

A selection of hot subluminous stars in the *GALEX* survey – II. Subdwarf atmospheric parameters [★]

Péter Németh^{†‡}, Adéla Kawka^{†‡} and Stéphane Vennes^{†‡}

Astronomický ústav AV ČR, Fričova 298, CZ-251 65 Ondřejov, Czech Republic

Accepted 2012 August 27. Received 2012 August 27; in original form 2012 May 15

ABSTRACT

We present an update of our low-resolution spectroscopic follow-up and model atmosphere analysis of hot subdwarf stars from the *Galaxy Evolution Explorer* (*GALEX*) survey. Targets were selected on the basis of colour indices calculated from the *GALEX* GR6 N_{UV} , Guide Star Catalogue (GSC2.3.2) V and the Two Micron All Sky Survey (2MASS) J and H photometry. High signal-to-noise ratio spectra were obtained at the European Southern Observatory (ESO) and the Kitt Peak National Observatory (KPNO) over the course of three years. Detailed H, He and CNO abundance analysis helped us improve our T_{eff} , $\log g$ and He abundance determination and to constrain CNO abundances. We processed 191 observations of 180 targets and found 124 sdB and 42 sdO stars in this sample while some blue horizontal branch stars were also found in this programme. With quantitative binary decomposition of 29 composite spectra we investigated the incidence of A, F and G type companions. The incidence of late G and K type companions and their effects on subdwarf atmospheric parameters were also examined.

Key words: catalogues – surveys – stars: abundances – stars: atmospheres – binaries: spectroscopic – subdwarfs

1 INTRODUCTION

Hot subdwarfs are core He burning stars located at the blue end of the horizontal branch (HB), also known as the extreme horizontal branch (EHB). These subluminous objects are located roughly midway between the early-type main-sequence (MS) stars and the white dwarf (WD) cooling curve in the Hertzsprung-Russell diagram (HRD). Being in a relatively long lasting (~ 160 Myr), intermediate evolutionary stage of $\sim 1M_{\odot}$ stars, they are quite common and likely to overwhelm WDs in blue and ultraviolet (UV) surveys of old stellar populations. These stars are the primary sources of the UV excess of elliptical galaxies (Brown et al. 1997, O’Connell 1999).

To look for bright, thus nearby WD and subdwarf candidates in the *Galaxy Evolution Explorer* (*GALEX*) data base, Vennes, Kawka & Németh (2011a) (hereafter: Paper I) devised a method based on UV, optical and infrared (IR) colours. Between 2008 and 2011, our systematic, low-resolution spectroscopic follow-

up with the European Southern Observatory (ESO)/New Technology Telescope (NTT) and the Kitt Peak National Observatory (KPNO)/Mayall telescopes confirmed 166 stars as hot subdwarfs. Here, we present the results of a model atmosphere analysis of 180 stars. Details of previous surveys of blue or ultraviolet excess objects and of our source selection can be found in Paper I. Here we modified the original selection criteria to avoid de-selecting bright sources with unreliable *GALEX* F_{UV} photometry. For *GALEX* $N_{UV} \leq 12.5$, where N_{UV} is corrected for non-linearity effects (Morrissey et al. 2007), we selected targets with $N_{UV} - V \leq 0.5$, where V is the Guide Star Catalogue version 2.3.3 (GSC2.3.2; Lasker et al. 2008) photographic magnitude (see Paper I), while ignoring the *GALEX* F_{UV} magnitude. 13 bright objects were added to our sample by using the modified criteria. Among the 180 stars we found 124 subdwarf B (sdB) and 42 subdwarf O (sdO) stars. Most of the remaining objects are classified as blue HB (BHB) stars. The 52 stars from Paper I are also re-analysed here with an extended abundance pattern and using a new fitting algorithm that provided consistent results with Paper I. Such large and homogeneously modelled samples of bright subdwarfs are useful in identifying candidates for pulsation (e.g., Østensen et al. 2010), radial velocity studies (e.g., Geier et al. 2011a, Napiwotzki 2008) and eventually to set observational constraints for formation and evolution theories.

The present paper deals with optical/IR data exclusively. We list N_{UV} magnitudes, but refer the interested reader to the UV work

[★] Based on observations made with ESO telescopes at the La Silla Paranal Observatory under programmes 82.D-0750, 83.D-0540 and 85.D-0866.

[†] E-mail: pnemeth1981@gmail.com (PN); kawka@sunstel.asu.cas.cz (AK); vennes@sunstel.asu.cas.cz (SV)

[‡] Visiting Astronomer, Kitt Peak National Observatory, National Optical Astronomy Observatory, which is operated by the Association of Universities for Research in Astronomy (AURA) under cooperative agreement with the National Science Foundation.

of Girven et al. (2012). A similar UV analysis will be reported elsewhere.

There are two main formation concepts for subdwarf stars, but current observational data cannot satisfyingly distinguish the contribution of their formation channels. The canonical subdwarf formation theory (Mengel, Norris & Gross 1976) invokes binarity and strong mass loss on the red-giant branch (RGB) for the formation of sdB stars, and WD binary mergers for the formation of He-rich hot sdO (He-sdO) stars (Webbink 1984). For a recent review of the canonical formation channels and binary population synthesis see Hu et al. (2008), Han et al. (2003a) and Han et al. (2003b).

The late hot-flasher scenario (D’Cruz et al. 1996) suggests a different evolutionary path that explains the abundance diversities observed in hot subdwarfs. This model also assumes a strong mass-loss on the RGB, but the star undergoes a core He-flash on the WD cooling track. Then, convective mixing would bring core material into the hydrogen envelope and would account for He, C and N overabundances.

Both models require an effective process to remove most of the hydrogen envelope on the RGB. The main difference is that the canonical formation scenario assumes a core flash on the tip of the RGB without mixing, while in the late hot-flasher scenario the star departs from the RGB before the flash happens allowing for shallow or deep convective mixing (Lanz et al. 2004).

Stringent observational constraints are needed to determine the relative contribution of these formation models. For this reason, detailed model atmosphere and binary analyses of large samples carried-out independently with different model atmosphere codes are necessary to reveal the contribution of various formation channels and the condition of mass loss on the RGB.

Throughout the paper we use the notation $[\text{He}/\text{H}]_{\bullet} = \log_{10}(n_{\text{He}}/n_{\text{H}})$ for abundance and $[\text{Fe}/\text{H}] = [\text{Fe}/\text{H}]_{\bullet} - [\text{Fe}/\text{H}]_{\odot}$ for metallicity. We omit the *GALEX* prefix, as well as the seconds and arcseconds of the identifier when referring to stars in the catalogue. Finally, we refer to possible short- (*p*-mode) and long-period (*g*-mode) pulsators as rapid and slow pulsators using the nomenclature of Kilkenny et al. (2010).

In Section 2 we briefly describe our data acquisition and reduction. In Section 3 we give details of our spectral modelling and fitting with TLUSTY and XTGRID, and our approach for binary decomposition. In Section 4 we present the properties of hot subdwarfs in the $T_{\text{eff}} - \log g$ and $T_{\text{eff}} - \text{He}$ diagrams, and describe our results on CNO abundance trends and binarity. In Section 5 we investigate the sample completeness by comparing our observed luminosity distribution to a modelled one. Modelling homogeneity is examined in Section 6. Subdwarf populations are reviewed in light of our results in Section 7. The catalogue of our *GALEX* sample is presented in Section 8 and Section 9 summarizes our results. Finally, in Section 10, we propose to initiate a large collaborative study on hot subdwarf stars.

2 FOLLOW-UP SPECTROSCOPY

Low-dispersion optical spectra were obtained at two sites during seven observing runs between 2008 and 2011. At ESO, we used the ESO Faint object Spectrograph and Camera (EFOSC2) attached to the 3.6-m NTT at the La Silla Observatory. On UT 2008 October 19-22, 2009 March 2-4 and 2009 August 23-27, we used grism #11 (300 lines mm^{-1}) with a dispersion of $\sim 4.17 \text{ \AA}$ per binned pixel (2 x 2). With a 1 arcsec slit width we obtained a resolution of $\Delta\lambda \approx 13.7 \text{ \AA}$. On UT 2010 March 2-4 and 2010 September 18-21 we

employed grism #7 (600 lines mm^{-1} , $\sim 1.96 \text{ \AA}$ per binned pixel) and a 1 arcsec slit width resulting in a resolution of $\Delta\lambda \approx 6.4 \text{ \AA}$.

At the KPNO on UT 2010 March 23-26 and 2011 January 28-31 the Ritchey–Chretien Focus Spectrograph (RC Spectrograph) was used with the 4-m Mayall telescope and KPC-10A (316 lines mm^{-1}) grating, delivering a spectral resolution of $\Delta\lambda \approx 5 \text{ \AA}$ in first order. The slit width was set at 1.5 arcsec resulting in a dispersion of $\sim 2.75 \text{ \AA}$ per pixel.

The KPNO spectra and the lower-resolution ESO data cover the entire Balmer-series from 3700 to 7400 \AA . The ESO $\Delta\lambda \approx 6.4 \text{ \AA}$ data covers the upper Balmer line series from 3600 to 5200 \AA . All data were reduced using standard IRAF¹ procedures.

Our selection also included three hot subdwarf candidates proposed by Jiménez-Esteban, Caballero, & Solano (2011). Two of these objects are *GALEX* sources outside of our selection criteria (TYC 6017-419-1 and TYC 9327-1311-1), while another lies in a region not covered by the survey (TYC 9044-1653-1). We included another two targets (J0716+2319 and J2349+4119) that are not subdwarfs, but accidentally met the criteria due to their erroneous *V* magnitude in our source selection. Although these stars are not formally part of the UV selection, we analyze their spectra in Section 3.

3 SPECTRAL ANALYSIS

3.1 Model atmospheres

We computed H/He/CNO non-LTE model atmospheres with TLUSTY 200 and synthetic spectra with SYNSPEC 48 (Hubeny & Lanz 1995; Lanz & Hubeny 1995). Model atoms of H I, He I–II, C II–IV, N III–V and O IV–VI; and detailed line profiles of H and He were used in SYNSPEC. For all relevant ions, we included the most detailed model atoms from the OSTAR2002 (Lanz & Hubeny 2003) and BSTAR2006 (Lanz & Hubeny 2007) data base.

Model atmospheres for BHB stars with effective temperatures below 20 000 K were calculated with H I, He I–II, C II–IV, N II–IV and O II–III model atoms. A line list compiled from Kurucz CD-ROM 23 and available at the SYNSPEC web page² was used. Details of the model atoms used in this work are listed in Table 1.

3.2 Spectral fitting with XTGRID

A spectral fitting method was employed by combining the steepest-descent and simplex algorithms, implemented in our new χ^2 minimizing fitting program XTGRID. This PYTHON program is an adjustable interface for TLUSTY and SYNSPEC, designed to carry out iterative multi-wavelength spectral analysis of hot stars from soft X-rays to near infrared wavelengths. The procedure requires a starting model and with successive adjustments approaches the observed spectrum.

At the beginning, XTGRID follows the gradient of steepest descent with a maximal step size that TLUSTY convergence allows. New step directions and sizes are calculated in a small grid (simplex step) and adjusted independently for each parameter. To follow the steepest gradient, relative step sizes are normalized to the leading parameter. Model atmospheres and synthetic spectra are calculated for a new temperature and gravity in all iterations, and only synthetic spectra are calculated for new abundances. Directions are

¹ <http://iraf.noao.edu/>

² <http://nova.astro.umd.edu/>

Table 1. Model atoms used for hot (H) and cool (C) subdwarfs.

Ion	Number of levels and line transitions	Frequency of highest level, s ⁻¹	Model
H I	9/10	3.273×10 ¹⁵	HC
H II	1/0	...	HC
He I	24/89	5.138×10 ¹³	HC
He II	20/51	3.289×10 ¹³	HC
He III	1/0	...	HC
C II	39/253	-5.299×10 ¹³	HC
C III	46/339	2.998×10 ¹⁴	HC
C IV	37/222	5.272×10 ¹⁴	HC
C V	1/0	9.480×10 ¹⁶	HC
N II	26/93	5.564×10 ¹⁴	C
N III	32/187	2.519×10 ¹⁴	HC
N IV	23/95	1.471×10 ¹⁵	HC
N V	16/95	8.227×10 ¹⁴	HC
N VI	1/0	1.335×10 ¹⁷	H
O II	29/123	6.622×10 ¹⁴	C
O III	41/226	2.410×10 ¹⁴	C
O IV	39/283	5.678×10 ¹⁴	HC
O V	40/225	1.685×10 ¹⁵	H
O VI	20/126	1.185×10 ¹⁵	H
O VII	1/0	1.788×10 ¹⁷	H

calculated from these fits and the starting model gets updated with the new model. This process is pursued until all relative changes (T , $\log g$, abundances and χ^2) decrease below 0.5 per cent in three consecutive iterations and all maximum allowed step sizes decrease below 50 per cent of their initial values. The latter condition ensures that a minimum is found for parameters with small gradients.

Temperature and gravity have a higher convergence rate than abundances. To take advantage of this observation and accelerate our procedure, parameter relaxation is included in the program. When relative changes of temperature or gravity decrease below 0.5 per cent they can be kept fixed for five iterations. This allows for slow converging parameters (like abundances) to approach their final values faster. Furthermore, such iterations save two out of the three model atmosphere calculations per iteration, the most time consuming part. After 11 iterations all models are calculated again for three iterations, to examine relative changes and to test if the final model is achieved. If the convergence limit is not reached, this loop of 14 iterations is repeated. This strategy provides about a factor of 2 speed-up with respect to regular iterations when model atmospheres are always calculated for a new temperature and gravity. Additionally, the fitting procedure accelerates automatically as by approaching the solution the relative differences between models get smaller.

XTGRID regularly reads the optional TLUSTY flag file, in which important control parameters can be stored for the fitting process. This way it is possible to adjust any fitting parameters or procedures during calculations.

A critical point in spectral fitting is the method how models are normalized to observations. Over a wide spectral range the match between theoretical and observed continua is usually poor in the beginning, while over a short wavelength range the continuum might not be visible because of broad spectral lines or line blanketing. To account for both effects, XTGRID samples the spectrum in small sections. The selection of these fitting windows is either specified by the user or the program partitions the entire data in equally sized

sections. The first setup can be used for selecting certain lines or ranges for fitting, like the hydrogen Balmer series or certain metal lines. When the whole spectrum is considered, only the segment size needs to be specified. The optimal section size depends on the spectral resolution, the spectral features being analysed and must be selected carefully. The synthetic spectrum is then normalized in each of these bins to the observed data by finding the ratio of their median fluxes. This simple approach tends to normalize for the continuum and normalization improves with the goodness of fit. Low order variations of the spectrum are significantly reduced this way, therefore the effects of interstellar reddening and poor fluxing, often seen at short optical wavelengths, are treated. An additional benefit of this method is, when the whole spectrum is used, that the χ^2 considers the interconnections between all spectral lines and the continuum. This can be very helpful in investigating the effects of metal abundances on hydrogen lines, in particular, to address the Balmer-line problem.

Although low order variations can be significantly reduced with a careful sectioning of the spectrum, our normalisation method considers the continuum as well, hence it is sensitive for flux calibration. Large deviations from the theoretical continuum due to a poor flux calibration can affect the final parameters. Hence, for consistent modelling the same sampling of the spectrum is necessary, or to work with continuum normalized spectra. XTGRID is designed to fit continuum normalized data as well.

To match the resolution of synthetic spectra to the observations, they are convolved with a Gaussian profile at either constant resolution (full width at half-maximum) or constant resolving power $R = \lambda/\Delta\lambda$.

Radial velocity corrections can be defined by specifying $\Delta\lambda/\lambda$ or taken as free parameter. If fitted, a χ^2 is calculated at small shifts of the model and the minimum is determined by a low order polynomial fit. This correction yields absolute radial velocities and updated after every third iteration with adjusted shifts.

After fitting is done, parameter errors for 60, 90 and 99 per cent confidence intervals are estimated by mapping the $\Delta\chi^2$ with respect to the final abundance (X) at representative points in the range of $-0.99 < \Delta X/X < 100$. Temperature and gravity errors are measured similarly in the range of $-0.26 < \Delta T/T < 0.26$ and $-0.195 < \Delta \log g/\log g < 0.195$. Parameters are changed until the statistical limit for the 60 per cent confidence level at the given number of free parameters is reached. Model atmospheres are calculated during error calculations for all synthetic spectra to track small changes of the χ^2 . This way the size and symmetry of error intervals can reflect the quality of the parameter determination. Errors at 90 and 99 per cent are extrapolated by a parabolic fit for the upper and lower error intervals independently.

XTGRID is scalable for cluster calculation and to further accelerate the fitting procedure, previously calculated models are reused until relative changes of temperature and gravity drop below 13 per cent of their respective maximum allowed values. Following this procedure, the program builds a model cloud that is more closely spaced near best solutions. Such accelerations are necessary to cope with the computing demand of model atmosphere analyses. In particular, in batch analysis of multiple spectra, because any change in the input data, physics or fitting procedure requires the recalculation of all fits to maintain homogeneity. In the final step \LaTeX fit summaries and GNUMPLOT scripts are produced for graphs shown in this paper. Figure 1 shows the best-fitting of the He-rich BHB star J2059-4232.

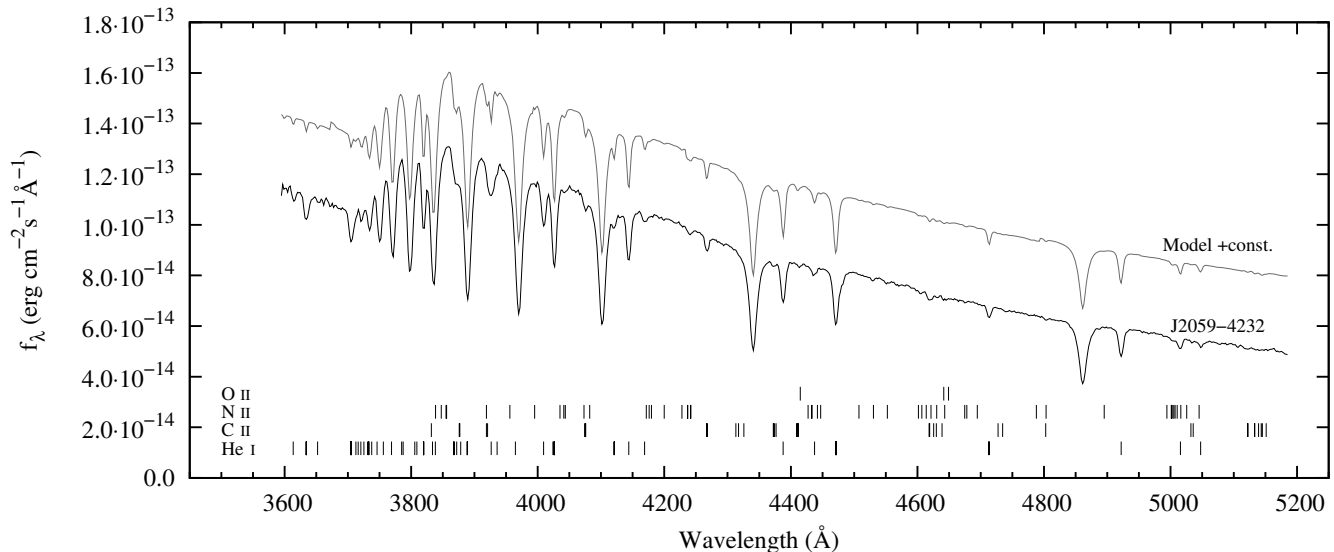


Figure 1. Observed NTT and best-fitting model spectrum for J2059–4232. Identifications are given for He and CNO lines with theoretical equivalent widths larger than 1 Å. The presence of He, C and N is statistically confirmed.

3.3 Binary spectral decomposition

Binarity plays an important role in the theory of subdwarf formation and evolution. In the canonical formation theory (Han et al. 2003a) the common-envelope, Roche lobe overflow and binary merger channels all depend on binary parameters. About 40 per cent of sdBs were found in binary or multiple systems with MS companions (Maxted et al. 2001, Napiwotzki, Karl & Lisker 2004). Reed & Stiening (2004) derived an sdB–MS (A0 to M2) binary fraction of 53 ± 6 per cent by using Two Micron All Sky Survey (2MASS; Skrutskie et al. 2006) $J-H$ and optical $B-V$ colours. Thejll, Ulla & MacDonald (1995) found ~ 43 per cent composite spectra in their sample of 27 subdwarfs. Stark & Wade (2003) found 40 per cent composite spectra in their magnitude limited sample of about 600 subdwarfs collected from the Palomar-Green survey (PG, Green, Schmidt & Liebert 1986) and the Catalogue of Spectroscopically Identified Hot Subdwarfs (Kilkenny, Heber & Drilling 1988). At least 20 per cent of subdwarfs show significant IR excess in the $V-J - J-H$ diagram (Ferguson, Green & Liebert 1984). In agreement with this number, about 19 per cent of our sample has $V-J > 0$ and $J-H > 0$ indicative of an IR excess (Figure 2). The true fraction of composites depends heavily on the quality of the spectra [signal-to-noise ratio (SNR), resolution] and selection criteria. Combining the frequency of composite spectra, radial velocity variables and photometric variables (ellipsoidal variations) we conclude that the binary fraction is close to two-thirds in agreement with Maxted et al. (2001).

About 17 per cent of our sample shows strong double lined composite spectra and about 33 per cent have noticeable Ca II H&K ($\lambda 3933$ and $\lambda 3968$ Å), Mg I ($\lambda 183$ Å) or Na I D ($\lambda 5890$ and $\lambda 5896$ Å) absorption lines. Fe I and CH molecular lines blend at $\sim \lambda 4300$ Å and notable in F and G type stars. This strong feature is often referred in the literature as the G band. We found G -band absorption in composite spectra. Although, these lines might have an interstellar origin, their simultaneous presence and a flat flux distribution can indicate a composite spectrum.

The high incidence rate of binaries and their importance in subdwarf evolution in addition to the fact that subdwarfs in composite spectra binaries cannot be modelled as single stars, inspired

us to include binary decomposition in XTGRID. In double-lined binaries both components can be examined simultaneously. In particular, the F and G companions are relatively easy to identify because they have characteristic spectral features different from subdwarfs and a comparable optical brightness. Late G and K companions present a bigger challenge because they have significantly lower contribution and weaker lines.

A library of low- and medium-resolution observed spectra was collected for spectral decomposition from the MILES (Cenarro et al. 2007, Sánchez-Blázquez et al. 2006) and HILIB (Pickles 1998) libraries with resolutions $\Delta\lambda = 2.3$ Å and $R = 500$, respectively. For visual inspections the spectral library of Silva & Cornell (1992) was also used. Altogether, 946 spectra between $\lambda 3525$ and $\lambda 7500$ Å at 2.3 Å resolution were included in our decomposition library from the MILES data base. This library provides a wide range of spectral types at sufficiently high resolution and good fluxing. HILIB templates were used to calculate synthetic colour indices in the optical and infrared.

We searched for the best-fitting template spectrum by interpolating in temperature, surface gravity, metallicity (as $[\text{Fe}/\text{H}]$) and flux ratio ($F_{\lambda, \text{comp.}} / (F_{\lambda, \text{comp.}} + F_{\lambda, \text{sd}})$) of the secondary component along with TLUSTY model parameters for the primary. The decomposition was performed at every third iteration and during the three consecutive iterations when fitting convergence was examined. The observed data were fitted with the linear combination of the subdwarf model and a secondary template. At the beginning, a 50 per cent flux contribution was assumed for F and early G type companions and the interpolation step size was 0.1 times the flux difference between spectra. At every decomposition iteration the interpolation step size was halved and after the fifth iteration it was set to 0.001. To avoid trapping, all template spectra were compared to the observed data at every iteration, but interpolation was performed only between the best-fitting template and its neighbours.

The decomposition of late G and K companions required a more elaborated method. Their most significant effect on the flux distribution is a slight flattening of the flux in the red part of the spectrum and relatively strong Na D lines. In this case, the initial flux ratio of the secondary was set to 15 per cent at the long wavelength end of the spectrum. Fitting started with a pre-defined

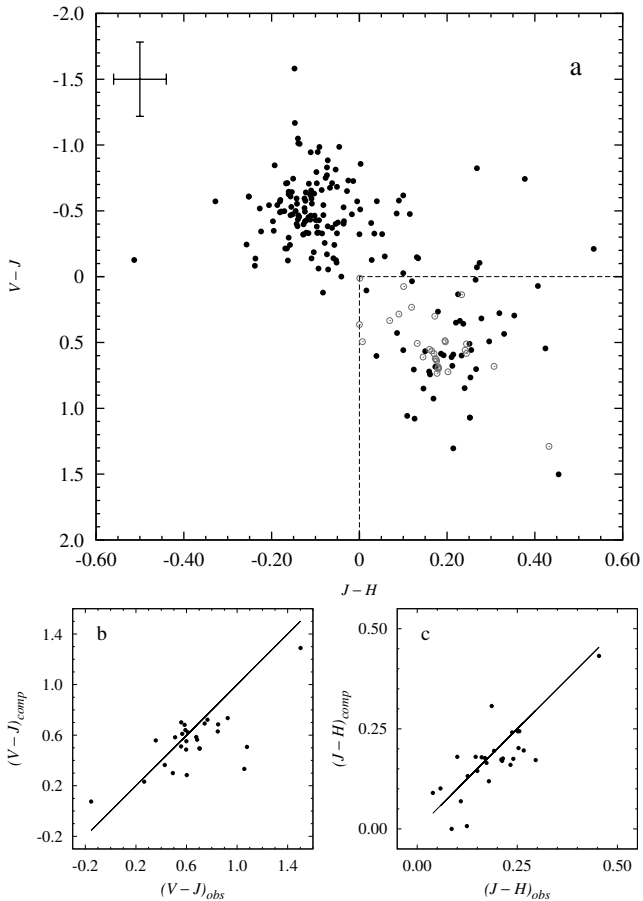


Figure 2. Panel *a* shows the $V-J$ vs. $J-H$ colour-colour diagram for our subdwarf sample. Optical magnitudes were collected from GSC2.3.2 and infrared from the 2MASS data base using Vizier. Apparently single stars aggregate near $V-J \approx -0.5$ and $J-H \approx -0.1$, while composite-spectra binaries show infrared excess (lower right corner). About 19 per cent of the stars have $V-J > 0$ and $J-H > 0$. Open circles show synthetic colour indices of the 29 binaries resolved in this work. Typical errors of photometric colour indices are shown in the upper left corner. Panel *b* and *c* show the correlations of synthetic and observed $V-J$ and $J-H$ colour indices, respectively.

section size to consider only spectral lines in the beginning, and the continuum was progressively considered by gradually increasing the section size up to three times the starting value. If the secondary contribution decreased below 10 per cent, the spectrum was sampled with the smallest possible sections, which was set to three times the size of a resolution element. This strategy is necessary only for late-type companions and does not change the results for F and early G stars, which can be modelled based on spectral lines. The fitting windows were reset to their input configuration in the last step and kept fixed during error calculations, because changing the size of fitting sections can introduce systematic shifts. In the case of late companions a high SNR (> 100), medium to high resolution data, and good fluxing are critical.

We consider that our semi-empirical approach in characterizing the cool star is not just faster, but less ambiguous than working with synthetic spectra for both components. To check if our interpolation returns real stellar spectra, the final templates were always compared to those calculated with the same parameters by

MILES Webtools³ (Vazdekis et al. 2003). Companion spectral types were determined using the MILES classifications. We show an example for our fit and spectral decomposition of the sdB-F7V binary J2124+1506 in Figure 3.

To resolve double-lined close binaries of similar luminosities, individual radial velocities would be helpful. However, such a study would require high-resolution spectra and templates or calculated spectra for both components. A productive method to resolve these binaries would be to obtain both ultraviolet and optical spectra.

3.4 Spectral fitting

We used the same initial model with: $T_{\text{eff}} = 40\,000$ K, $\log g = 5.6$ cm s^{-2} , $[\text{He}/\text{H}]_{\bullet} = -1$ and $[(\text{C}, \text{N}, \text{O})/\text{H}]_{\bullet} = -2$ to fit our observations. Maximum relative changes per iterations were limited to ± 5 per cent for T_{eff} , ± 2 per cent for $\log g$ and $+100$ per cent, -50 per cent for all abundances in order to maintain a stable TLUSTY convergence. We fitted only fluxed spectra with 80 \AA segments (each having six to 16 resolution elements depending on the resolution) using the entire spectral range. In order to decrease model atmosphere calculation time we used 30 depth points. Our tests showed this simplification affects model convergence before it would significantly change the emergent flux at low resolution. Model atmospheres were calculated in non-LTE radiative equilibrium without convection. Detailed profiles of H and He lines were included, but rotational broadening was not. A high rotational velocity is not typical for subdwarf stars. Fitting of ~ 200 observed spectra took ~ 800 h with six processors (15.2 GHz total) and needed the calculation of about 25 000 model atmospheres.

All fits are available in our online catalogue⁴.

3.4.1 Known issues

The piecewise normalization procedure implemented in XTGRID can reduce the effects of continuum inconsistencies between the theoretical and observed spectra as well as the effect of interstellar reddening. However, the method creates discontinuities in the fit residuals of stars that suffer from large reddening. Such fractures in the residuals may divert the fitting procedure and introduce systematic shifts in the derived parameters. Therefore, we performed extensive tests to discover if a wavelength dependent extinction correction would change atmospheric parameters significantly. We included the extinction function from Cardelli, Clayton & Mathis (1989) in XTGRID, and implemented an iterative reddening determination in the program. After recalculating some heavily reddened spectra, we did not find systematic differences. Our quoted error bars are larger than the effects of our normalisation on the parameters. We estimated the interstellar extinction from the final fits and listed the associated $E(B-V)$ colour excesses in Table 2 and 3. These values are consistent with the dust maps of Schlegel, Finkbeiner & Davis (1998) that provide an upper limit to the extinction coefficient toward each target.

Our binary decomposition method tends to attribute interstellar absorption lines along with other spectral lines to the template and fits the primary in this environment. This can cause degeneracy for binaries with similar components, like in J0716+2319. A single star fit provided a subluminal star with $T_{\text{eff}} = 12940 \pm 300$

³ <http://www.iac.es/proyecto/miles/pages/webtools.php>

⁴ <http://pleione.asu.cas.cz/~nemeth/work/galex/>

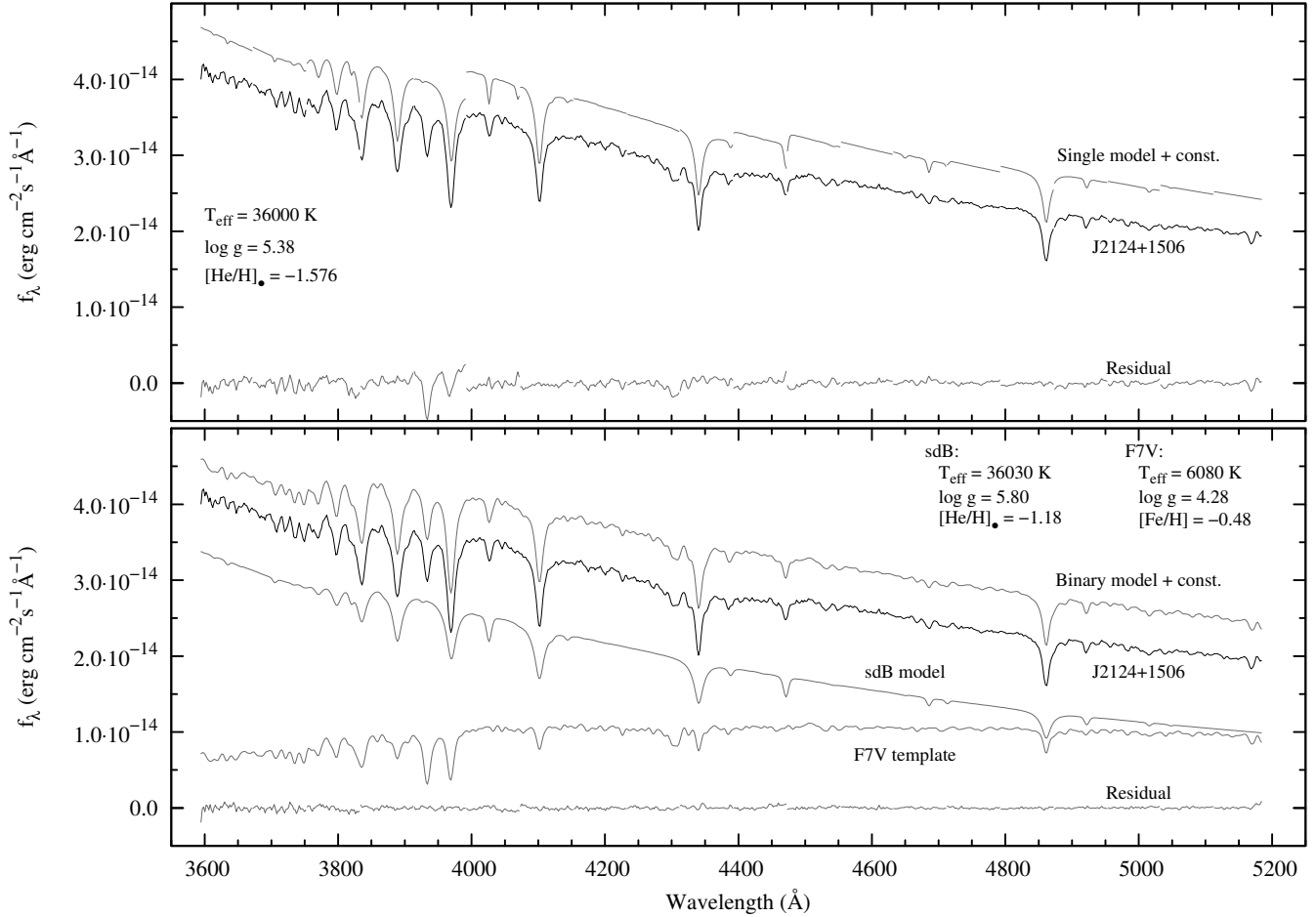


Figure 3. Binary decomposition of J2124+1506. The single model (top panel) can not reproduce the composite spectrum, the G-band (~ 4300 Å), Ca II H&K (3933 and 3968 Å) and Mg I (5183 Å) lines are clearly in the residual. The jagged model also indicates that the theoretical continuum is inconsistent with the observation. When the spectrum is modelled with an additional cool MS component (bottom), all major spectral features are reproduced well. The subdwarf temperature in this case was adjusted mildly, while there was significant change in the surface gravity and He abundance. A CNO abundance could not be measured in the spectrum.

K and $\log g = 5.34^{+0.01}_{-1.43}$ and slightly subsolar abundances. The apparent Ca and Mg lines, the H line profiles, the very asymmetric error in gravity and the infrared excess suggested the presence of a companion. Binary decomposition provided a much better fit with a B-A1V pair with $T_{\text{eff}} = 11140 \pm 180$ K, $\log g = 4.39^{+0.06}_{-0.22}$ primary and $T_{\text{eff}} = 9310$ K, $\log g = 3.67$ secondary.

Bright companions, like A stars, outshine sdB stars in the optical. Atmospheric parameters of relatively cooler subdwarfs in such binaries can be measured only with large uncertainty. In J2349+4119 the $T_{\text{eff}} = 7940$ K, $\log g = 3.44$, A4V companion contributes 87 per cent of light in the B photometric band. The determination of $T_{\text{eff}} = 11730$ K and $\log g = 5.8$ for the primary is less certain. Radial velocity measurements would help finding the true nature of this binary.

In unresolved composite spectra XTGRID can attribute subdwarf metal lines to the lines of the companion, leading to incorrect CNO abundances. While C and/or N is relatively abundant compared to O and show lines in the spectrum, this affects the O abundance determination in the first place. Companion G-band absorption overlaps with the strongest O II lines ($\lambda 4273$ – $\lambda 4322$ Å) of cool subdwarfs in composite spectra binaries. These lines are important in the O abundance determination and their attribution to secondary

features can, in some case, lead to an underestimated O abundance of subdwarfs. Contrarily, XTGRID might overestimate the O abundance of sdO stars in unresolved composite spectra binaries. Our current O abundances are only preliminary determinations, a complete study requires higher-dispersion spectra.

The puzzle of the N III/C IV $\lambda 4640$ – $\lambda 4665$ Å blend still challenges the present spectral modelling. We observed the blend in about half of the hot He-sdO stars over a wide range of temperature and our fits do not reproduce it satisfactorily. We revised our line list and updated the atomic data for the C IV $\lambda 4658.3$ Å multiplet with lines between the $1s^2 5f(2F^\circ)$ – $1s^2 6g(2G)$, $1s^2 5g(2G)$ – $1s^2 6h(2H^\circ)$ and $1s^2 5g(2G)$ – $1s^2 6f(2F^\circ)$ levels from the Tübingen NLTE Model-Atmosphere Package (TMAP; Werner & Dreizler 1999) available at the German Astrophysical Virtual Observatory page⁵. We noted a line strength inconsistency of the C III $\lambda 4070$ Å multiplet with the C IV $\lambda 4658.2$ Å multiplet as well as with the C IV $\lambda 5801.3$ and $\lambda 5812$ lines. Our models show too strong C III and too weak C IV lines compared to the observations, indicating an underestimated temperature or an overestimated gravity. The effects of a

⁵ <http://astro.uni-tuebingen.de/~TMAD/>

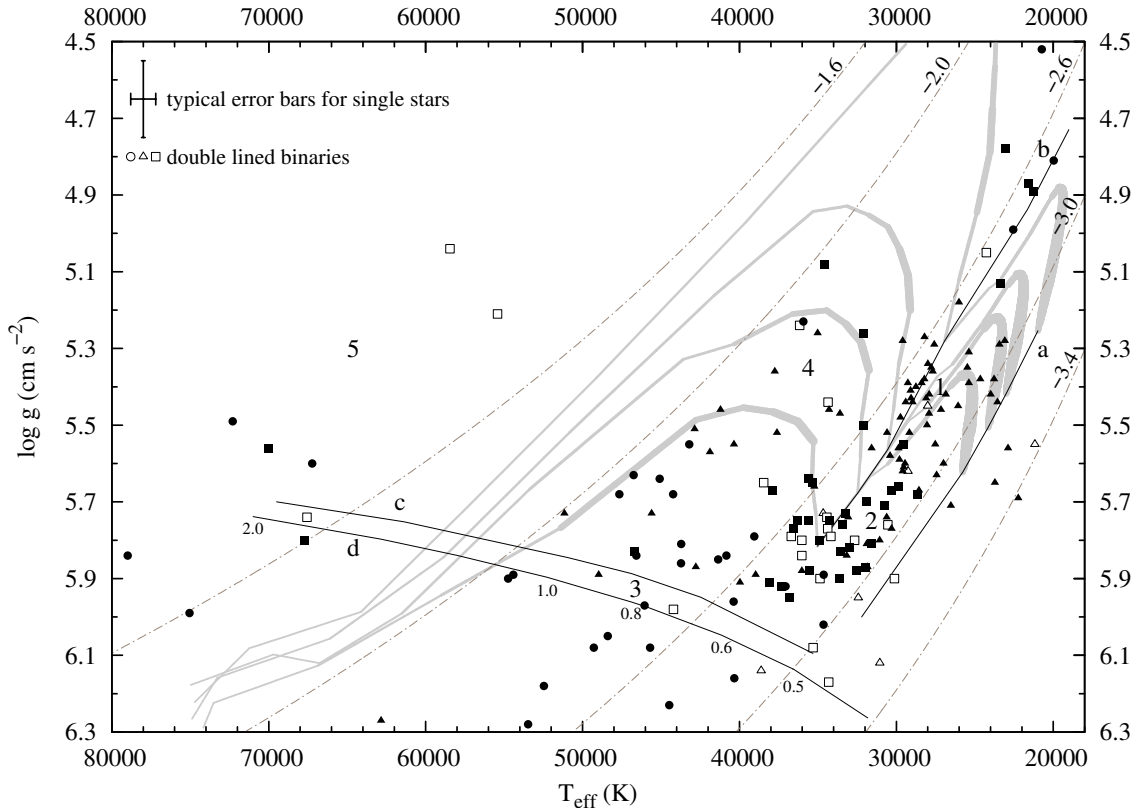


Figure 4. $T_{\text{eff}} - \log g$ diagram. The ZAEHB and TAEHB (Dorman, Rood & O’Connell 1993) are marked with “a” and “b”, respectively. The HeMS is taken from Paczyński (1971) and Divine (1965) and are marked with labels “c” and “d”, respectively. Stellar masses are marked along the HeMS in M_{\odot} . The grey lines are theoretical evolutionary tracks from Dorman, Rood & O’Connell (1993) for stellar masses from top to bottom: 0.480, 0.475, 0.473 and 0.471 M_{\odot} . Line widths are proportional to evolutionary time-scales. Typical error bars are shown in the upper left corner. He-rich ($[\text{He}/\text{H}]_{\odot} > -1$) stars are indicated with filled circles, He-poor ($[\text{He}/\text{H}]_{\odot} < -2.2$) stars with filled triangles and stars with $-2.2 \leq [\text{He}/\text{H}]_{\odot} < -1$ are with filled squares. Subdwarfs in resolved composite spectra binaries are shown with open symbols following the same classification. Iso-luminosity curves for $L/L_{\text{edd}} = -1.6, -2.0, -2.6, -3.0$ and -3.4 are shown with dash-dotted lines. These are characteristic values in the luminosity distribution.

change in gravity are low on metal lines, hence only a change in temperature could provide better fits. However, the ionisation balance shows that the C IV ion is dominant over C III above $\sim 42\,000$ K, hence an increase in the temperature would decrease the C III line strength, but would not increase the C IV opacity. Such changes in temperature or gravity would be inconsistent with the H and He line strengths as well. The high C and N abundance of these stars implies a high probability of heavier elements, in particular the iron-peak elements, which can be accounted for the missing opacities. Haas et al. (1996), Werner et al. (1998) and recently O’Toole & Heber (2006a) found high abundances of heavy elements in hot subdwarf stars. A review of the atomic data input is necessary and deserves a separate study.

4 PROPERTIES OF HOT SUBDWARFS

Our sample is large enough and appropriate for revisiting the distribution of stars in the $T_{\text{eff}} - \log g$ and $T_{\text{eff}} - \text{He}$ planes as well as to look for possible correlations in the He and CNO abundances. Such diagrams are very important tools in tracking subdwarf evolution and pulsational modes, because with the help of a model atmosphere program, stellar temperature, gravity and element abundances can be derived without any assumptions on distances or stellar luminosities. A comparison of the distribution of stars in these diagrams is also useful to test our fitting method.

Our spectral classification follows the simple scheme of Paper I: Subdwarfs with $T_{\text{eff}} < 40\,000$ K showing dominant H lines and weak He I are classified as sdBs; with $T_{\text{eff}} > 40\,000$ K and weak lines of He II are sdOs. Stars with dominant He I lines are He-sdBs, while those with dominant He II lines are classified as He-sdOs. Stars with $T_{\text{eff}} < 20\,000$ K and $\log g < 5$ are listed as BHB stars and with $\log g < 4.5$ are classified as MS B stars. Using this categorization, out of the 180 stars we found 166 subdwarfs, 124 of which are classified as sdB and 42 as sdO stars. The sdB/sdO number ratio of ~ 3 is the same figure as previously determined (Heber 2009). We found five He-sdB stars (or ~ 4 per cent) among the 124 sdB and 26 He-sdO (or ~ 62 per cent) out of the 42 sdO stars. In the 29 resolved spectroscopic binaries only four (namely: J0710+2333, J1602+0725, J2020+0704 and J2038-2657) have sdO primaries and two binaries (J0047+0337 and J2331+2815) are in the sdB/sdO transition region. No He-sdO subdwarfs were found in composite spectra binaries. One system (J0716+2319) is a MS binary and one (J2349+4119) is a possible low mass pre-WD-MS binary. The remaining 21 composites are classified as sdB-MS binaries.

4.1 The $T_{\text{eff}} - \log g$ plane

The properties of our hot subdwarfs in the temperature-gravity plane are shown in Figure 4. The distribution of sdB stars follow the theoretical EHB and He-sdO stars are scattered near the He

main-sequence (HeMS), with some stars along post-EHB evolutionary tracks. The post-EHB tracks of Dorman, Rood & O’Connell (1993) for subdwarf masses from top to bottom: 0.480, 0.475, 0.473 and 0.471 M_{\odot} are shown in grey. The zero-age EHB (ZAEHB) and terminal-age EHB (TAEHB) are marked with "a" and "b", respectively. The HeMS is taken from Paczyński (1971) and Divine (1965) and are labelled with "c" and "d", respectively. Stars with $[\text{He}/\text{H}]_{\bullet} > -1$ are marked with filled circles; most of these spread along the HeMS. Stars with $[\text{He}/\text{H}]_{\bullet} < -2.2$ are indicated with filled triangles and gather at lower temperatures and gravities than stars with $2.2 \leq [\text{He}/\text{H}]_{\bullet} \leq -1$ that are shown with filled rectangles and crowd around $T_{\text{eff}} \approx 35\,000$ K and $\log g = 5.8$. Resolved composite spectra binaries are marked with open symbols using the same scheme. Dash-dotted lines show iso-luminosity fractions, where the luminosity is expressed as the fraction of the Eddington-luminosity calculated from the effective temperature and surface gravity:

$$\log \frac{L}{L_{\text{Edd}}} = 4 \times \log T_{\text{eff}} - \log g - 15.118. \quad (1)$$

This distance independent quantity statistically separate stars. Assuming a constant stellar mass for sdB stars, these curves are also proportional to their absolute luminosities.

Figure 4 reveals five distinct regions in the $T_{\text{eff}} - \log g$ diagram. The cooler, He-poor sdB stars (no. 1) are found around 28 000 K and $\log g = 5.45$. These are potential slow pulsators ($P \approx 40 - 170$ min). The hotter sdB stars (no. 2) near 33 500 K and $\log g = 5.8$ are on average 10 times more He abundant and possible rapid pulsators ($P \approx 2 - 6$ min). The hot and He-rich sdO stars (no. 3) are found mostly between 40 000 and 55 000 K near $\log g = 5.9 \pm 0.4$. Although numerous He-sdO stars are above the theoretical HeMS, as theoretical models predict, an asymmetric scatter toward high gravities is apparent in our data and noted in the literature (Østensen 2009). He-weak sdO stars (no. 4) are located above both the EHB and HeMS. Finally, the least defined population: possible progenitors of low-mass WDs, pre-WDs, post-Asymptotic Giant Branch (post-AGB) stars and central stars of planetary nebulae (CSPN), that might cross this region evolving towards their cooling tracks (no. 5) are also distinguished. The lack of stars along sections of fast evolution, in particular between $-2.0 < L/L_{\text{Edd}} < -1.6$ is also notable in Figure 4. Furthermore, it is immediately seen in the figure that He abundance, surface temperature and gravity are correlated.

While sdB stars are assumed to evolve more or less along the indicated evolutionary tracks, He-sdO stars in lack of a H envelope are expected to leave the HeMS towards higher temperatures and gravities after He exhaustion. However, this fast evolution cannot explain the observed clustering of high gravity He-sdO stars. Hu et al. (2008) found that stars with $M_{\text{ZAMS}} > 2 M_{\odot}$ can ignite core He-burning in non-degenerate conditions and after the EHB such stars can develop a He-burning shell and a different structure than canonical subdwarfs. An observational property of these stars would be their clustering below the theoretical HeMS. From an observational point of view, incomplete line broadening parameters of He lines can also be responsible for overestimating gravity in such stars. More observations are needed to better characterize these high gravity He-sdO stars.

A known shift in sdB temperatures by about +2000 K compared to the blue edge of the theoretical EHB band (Charpinet et al. 2007) is also noticeable in Figure 4. Similar shifts have been observed in previous analyses with various modelling and fitting techniques in volume limited samples. Hence, this discrepancy deserves

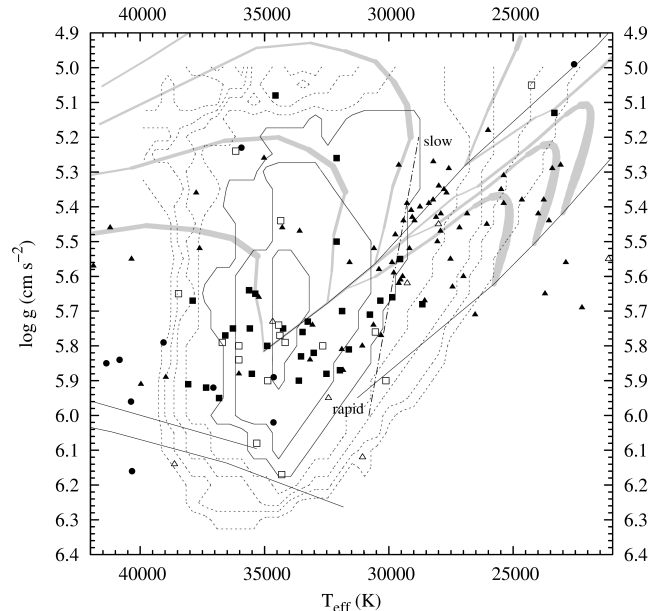


Figure 5. Subdwarfs in the theoretical instability region. Contours were rendered from Charpinet et al. (2011) and are overplotted on our data. Rapid (p -mode) pulsators are concentrated within the subdwarf instability region (Charpinet, Fontaine & Brassard 2001), indicated by the contours, driving is most efficient in the three highest contours (solid lines). The dash-dotted line separates slow and rapid pulsators. This boundary was found observationally based on an independent dataset (Charpinet et al. 2010).

attention from the theoretical side. Jeffery & Saio (2006) showed that including more iron-peak elements in the models would shift the theoretical EHB towards the observations.

The contours in Figure 5 mark the theoretical pulsational instability region by Charpinet, Fontaine & Brassard (2001) and are overplotted on our sample. The pulsations are driven by the iron-peak opacity bump. Charpinet, Fontaine & Brassard (2009) and Hu H. (2011) calculated models with equilibrium Fe abundance between radiative levitation and gravitational settling. The contours in Figure 5 were reproduced from Charpinet et al. (2011) and show the number of pulsating $\ell = 0$, p -modes. The outermost contour corresponds to a single mode and the highest in the centre to seven. Driving is most efficient in the three innermost contours. Possible rapid (p -mode) pulsators are located around 33 500 K and $\log g = 5.7$ while presumed slow (g -mode) pulsators are around 28 000 K and $\log g = 5.4$. The boundary that separates slow and rapid pulsators is marked with the dash-dotted line and was found independently (Charpinet et al. 2010). We refer to these groups as possible pulsators, although variable and non-variable stars co-exist in their observed parameter space. Østensen et al. (2010) found a ~ 10 per cent incidence rate for rapid pulsators in their survey for pulsating hot subdwarfs with the Nordic Optical Telescope. Slow pulsators show a larger incidence rate, reaching ~ 75 per cent according to Green et al. (2003), which was recently confirmed by the Kepler sdB sample (Østensen et al. 2011). In between these two groups are the hybrid (or mixed-mode) pulsators that show both slow and rapid modes. Based on the distribution of stars in Figure 5 many of our subdwarfs are possible pulsating candidates and a deep asteroseismic follow-up would be reasonable. Based on the locations of known pulsators we sorted out and flagged candidates for pulsation studies in Table 2. We would like to note that the *GALEX* sample

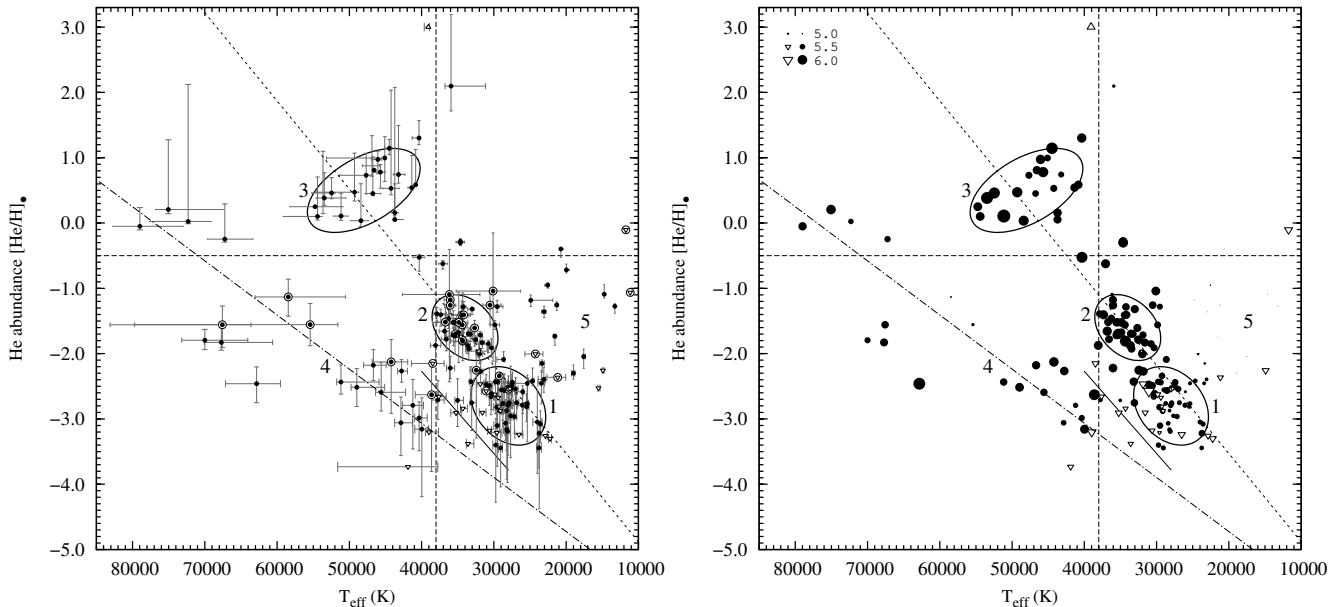


Figure 6. *Left:* He abundance versus effective temperature. Two trends of increasing abundance with effective temperature can be seen. Also remarkable are the clumping of possible slow (#1, near 28 000 K and $[\text{He}/\text{H}]_{\bullet} = -1.5$) and rapid sdB pulsators (#2, near 33 500 K and $[\text{He}/\text{H}]_{\bullet} = -2.7$) and the hot He-rich sdOs (#3). The sequence of He-weak subdwarfs (#4 and dash-dotted line) follow a similar correlation with effective temperature as more He rich stars (short dashed). The short full line is the best fit from Edelmann et al. (2003) for the He-weak sequence. Suspected progenitors of low-mass WDs and BHB stars are also possible in this region of the HRD (#5). The pure He atmosphere of J0851-1712 is an extreme case, we determined only a lower limit of its He abundance. Upper limits are indicated with open down triangles and binary stars are encircled. *Right:* Same data without error bars and point sizes are proportional to surface gravities (point size = $\log g - 4.8$) as shown in the upper left corner. Indicated regions are intended to guide the eye and are not derived from the data. Interesting to note the distribution of composite spectra binaries as well as surface gravity correlations.

presented here is a consistent set, the relative position of the stars to each other are free of major systematic shifts.

4.2 The $T_{\text{eff}} - \text{He}$ diagram

The He abundance in hot subdwarf stars is another fundamental parameter and must be investigated along with surface temperature and gravity. The panels of Figure 6 show the distribution of stars in the $T_{\text{eff}} - \text{He}$ diagram and their correlations with surface gravities. The five groups introduced in Section 4.1 are separated in the $T_{\text{eff}} - \text{He}$ plane as well. The He-poor (no. 1) and He-rich (no. 2) sdB stars, the sequences of He-sdO (no. 3) and He-weak sdO (no. 4) stars are marked in Figure 6 as well as BHB stars and possible WD progenitors (no. 5). The two $T_{\text{eff}} - \text{He}$ correlation sequences first described by Edelmann et al. (2003) are also remarkable. In general, the He abundance increases with temperature. Our He detection limit is at $[\text{He}/\text{H}]_{\bullet} \approx -3$ and does not allow to trace the two helium sequences deeper, although some data suggest a continuation of the He-weak sequence. Similarly large and homogeneously modelled samples like the Hamburg Quasar Survey (HS, Edelmann et al. 2003), Supernova Ia Progenitor survey (SPY, Lisker et al. 2005, Ströer et al. 2005) and Sloan Digital Sky Survey (SDSS, Hirsch, Heber & O’Toole 2008) confirm this observation (O’Toole 2008). In Figure 6 we plot the best fit line (short dashed) for sdB stars from the HS sample (Edelmann et al. 2003) for the He-rich sequence:

$$[\text{He}/\text{H}]_{\bullet} = -3.53 + 1.35 \left(\frac{T_{\text{eff}}}{10^4 \text{K}} - 2.00 \right). \quad (2)$$

This independent trend fits our sdB data as well, in particular for He-rich sdBs and passes through the region of He-sdO stars. We also plot their regression (full line) for the He-weak sequence.

However, we found a different trend (dash-dotted line) for these stars, possibly because the temperature range of the He-weak sequence was under-represented in the HS survey ($T_{\text{eff}} < 40\,000$ K). Separating He-weak stars at

$$[\text{He}/\text{H}]_{\bullet} < 1.08 \times 10^{-4} T_{\text{eff}} - 6.64, \quad (3)$$

and fitting them in a similar manner we got:

$$[\text{He}/\text{H}]_{\bullet} = -4.26 + 0.69 \left(\frac{T_{\text{eff}}}{10^4 \text{K}} - 2.00 \right). \quad (4)$$

Although, it can be seen from these fits that the distribution of subdwarf stars is much more complex and cannot be satisfactorily described with simple linear trends, hence we omit their significance test. Multiple breaks can be found in the He abundance distribution. There is a clear cut in temperature (vertical dashed line) in Figure 6, separating sdB and sdO stars somewhere between 36 000 and 40 000 K depending on the He abundance. To the right of this line are the two, relatively well defined groups of sdB stars, while to the left are the hot, either He-weak or He-rich sdO stars. A He abundance split is also remarkable at the line $[\text{He}/\text{H}]_{\bullet} = -0.5 \pm 0.5$ (horizontal dashed line), in particular over 40 000 K, where no stars can be found. Such a gap can be seen in the SPY data as well. Observationally this corresponds to a region where stars are expected to either never enter or pass through quickly during their evolution. The major formation theories in Section 7 also predict a lack of stars in this region. Similarly to the $T_{\text{eff}} - \log g$ distribution, possible rapid and slow sdB variable stars are separated according to their He abundance. Rapid pulsator candidates with $[\text{He}/\text{H}]_{\bullet} \approx -1.5$ have, on average, an order of magnitude higher He abundance than their slow pulsating counterparts with $[\text{He}/\text{H}]_{\bullet} \approx -2.7$. A region of photospheric mixing and He enrichment near $T_{\text{eff}} \approx 38\,000$ K at

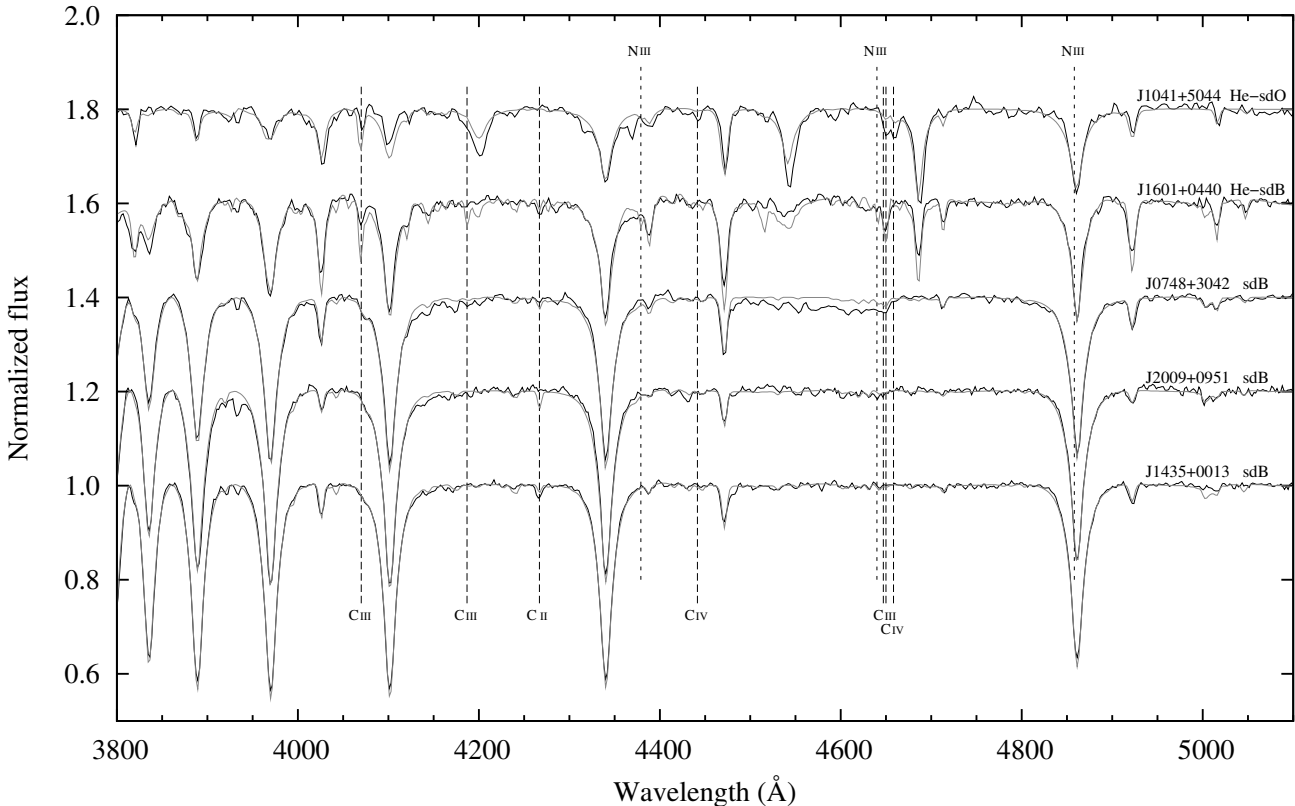


Figure 7. Sample fits (grey lines) of five subdwarf spectra (black lines) with increasing effective temperatures from bottom to top. The strongest C and N lines are marked.

$\log g \approx 6$ was predicted by Groth, Kudritzki & Heber (1985) and recently reviewed by Miller Bertolami et al. (2008). Our data show some abundance extremes in this region with $[\text{He}/\text{H}]_{\odot} > 1$ for He-sdO stars, culminating at the location of J0851-1712 in which we could determine only a lower limit of the He abundance. Toward higher temperatures from the sdB/sdO border the He abundance in He-sdO stars shows a decrease with temperature. The He abundance in these stars shows a correlation with mass along the HeMS.

Below the sdB/sdO border, a few He-sdB stars in our data show a He overabundance, but in general we can conclude that the He abundance is proportional to the effective temperature in sdB stars, and no stars can be found with similarly high He abundances like in He-sdO stars. In the proximity of the sdB/sdO transition both He-rich and He-poor sdB and sdO stars can be found. The case of He-weak sdO stars is simpler. They show a correlation with effective temperature similar to sdB stars and are connected to sdB stars at the sdB/sdO border. Their binary frequency and surface gravity diversity suggests that the He-weak sequence is a mixture of multiple populations. We discuss this point further in Section 7.

While parameter errors of temperature and gravity show gradual increase to higher temperatures, the error budget for the He abundance seems to be three-fold: sdB and BHB stars have well defined atmospheric parameters with symmetric error bars. He-weak sdO stars have significantly larger errors and show asymmetries in temperature. He-sdO stars show a rather symmetric temperature, but very asymmetric He abundance errors; our method tends to stop at the lower limit. Probably because at such high temperatures and He abundances the spectrum is He dominated and hydrogen lines are difficult to trace with low-resolution spectroscopy. In such conditions He becomes the reference element and the χ^2 is less

sensitive for the change of the shallow He lines. Beyond the low resolution of our spectra, the incomplete chemical composition of our models can also be blamed for the larger parameter errors of He-sdO stars.

By comparing the panels in Figure 6 further differences between the two He sequences become apparent: there is a strong correlation between surface temperature, gravity and He abundance of sdB and He-sdO stars, but this cannot be said about He-weak sdO stars. Among these stars a much weaker correlation and scattered high gravity stars can be found. Also notable are the low temperature sdB and BHB stars that have a wide distribution in He abundance and low surface gravities. Some of our subdwarfs show a low He abundance at a relatively high gravity, these are possible progenitors of low-mass WDs.

4.3 CNO trends

Metal abundance patterns are difficult to obtain from optical spectra, because the vast majority of CNO lines are in the ultraviolet and CNO lines in the optical are relatively insignificant. In spite of the weakness of these lines, our analysis provided C and N abundances for a number of sdB and sdO stars. Our metal abundance determination is based on the global effects of a specific chemical composition on the entire spectrum as well as on individual lines. We adopted this method mainly because in low-dispersion optical spectroscopy weak metal lines are heavily blended and hard to identify, but, thanks to the flux blocking of UV lines the overall shape of the energy distribution is also affected by the chemical composition. Sample fits for various subdwarf types are shown in Figure 7. Following the C&N analysis of sdO stars by Stroeger et al.

(2007), we summarise our results for the *GALEX* sample in Figure 8. In the $T_{\text{eff}} - \log g$ diagram the coolest EHB and BHB stars ($T_{\text{eff}} < 24\,000$ K) show both C and N abundances. Cooler sdB stars between 24 000 K and 30 000 K show a higher N abundance, but no C in general. In a narrow range around 30 000 K both C and N were found in some stars. The majority of sdB stars over 30 000 K show much less diversity, in most of these stars only He was found similarly to post-EHB stars. He-sdO stars show a diversity of surface abundances, but a pattern can be outlined. N-class stars are concentrated below $T_{\text{eff}} < 45\,000$ K. He-sdO stars with higher temperature and surface gravity belong to the C-class, while a group of C&N-class objects can be found in a narrow strip at $\sim 45\,000$ K. The C-class seems to belong exclusively to hotter He-sdO stars. Finally, the hottest sdO stars ($T_{\text{eff}} > 60\,000$ K) show a N overabundance in their spectra. The evolutionary status of these stars is an interesting question. They might belong to evolved He-sdO stars moving away from the HeMS as well as to He-weak sdO stars moving towards the HeMS in the temperature-gravity diagram (Husfeld et al. 1989).

Based on the $T_{\text{eff}} - \text{He}$ graph, we can confirm the conclusions of Stroerer et al. (2007) that He-weak sdO stars do not show metal traces. We found only a few stars around $T_{\text{eff}} \approx 40\,000$ K near $[\text{He}/\text{H}]_{\bullet} \approx -0.5$ where a small clumping was observed in the SPY sample. However, in our data, the trend of decreasing He abundance with increasing effective temperature can be traced down to $[\text{He}/\text{H}]_{\bullet} > 0$ in contrast with $[\text{He}/\text{H}]_{\bullet} > 1$ found by Stroerer et al. (2007).

Figure 8 gives only a qualitative picture of the C and N distribution, because these graphs do not reflect element abundances. To further investigate the C and N abundance distributions and possible C–He, N–He and C–N abundance correlations we refer to the panels of Figure 9, where only positive determinations are shown. In Appendix A we repeat these figures supplemented with error bars and upper limits.

Panels *a*, *b* and *c* of Figure 9 show CNO trends with respect to temperature. The approximate border between sdB and sdO stars at $T_{\text{eff}} \approx 38\,000$ K is shown by a vertical line and solar abundances from Grevesse & Sauval (1998) are indicated with horizontal dashed lines. Out of the 180 stars, we measured a He abundance in 149; 68 showed N, 39 showed C, but only 7 showed O in their spectra. A quick look reveals that the bulk of sdB stars have subsolar C and O abundances and roughly solar N abundances. He-sdO stars show higher abundances, strongly correlated with effective temperature. Interpreting the abundance distribution in the direction of increasing temperature: both C and N show a similar abundance in cooler sdB or BHB stars in the range $20\,000 \text{ K} < T_{\text{eff}} < 23\,000 \text{ K}$ of about $[\text{C}/\text{H}]_{\bullet}, [\text{N}/\text{H}]_{\bullet} \approx -3$. In sdB stars between $23\,000 \text{ K} < T_{\text{eff}} < 34\,000 \text{ K}$ a lower abundance of about $[\text{C}/\text{H}]_{\bullet}, [\text{N}/\text{H}]_{\bullet} \approx -4$ was measured. Above $T_{\text{eff}} \approx 35\,000 \text{ K}$ across the sdB/sdO border a significant abundance increase of C and N is observed reaching a peak near $T_{\text{eff}} \approx 43\,000 \text{ K}$ at $[\text{C}/\text{H}]_{\bullet}, [\text{N}/\text{H}]_{\bullet} \approx -1$, over this temperature the abundance of both elements decrease steadily with temperature. The hottest stars indicate a gradual abundance increase over $T_{\text{eff}} \approx 60\,000 \text{ K}$. Only a few stars without He in their spectra show C or N. These trends are very similar to those found in the He abundance distribution and similar observations were made in the SPY data (Lisker et al. 2005, Stroerer et al. 2007).

In panels *d* and *e* of Figure 9 the C and N abundances are plotted with respect to the He abundance. The 39 stars that have C determination have He as well. Out of the 68 stars showing N, 64 show a He abundance. The stars in which both C and N were found simultaneously are fitted with a full line. A similarly complex C and N abundance pattern can be outlined from this data as

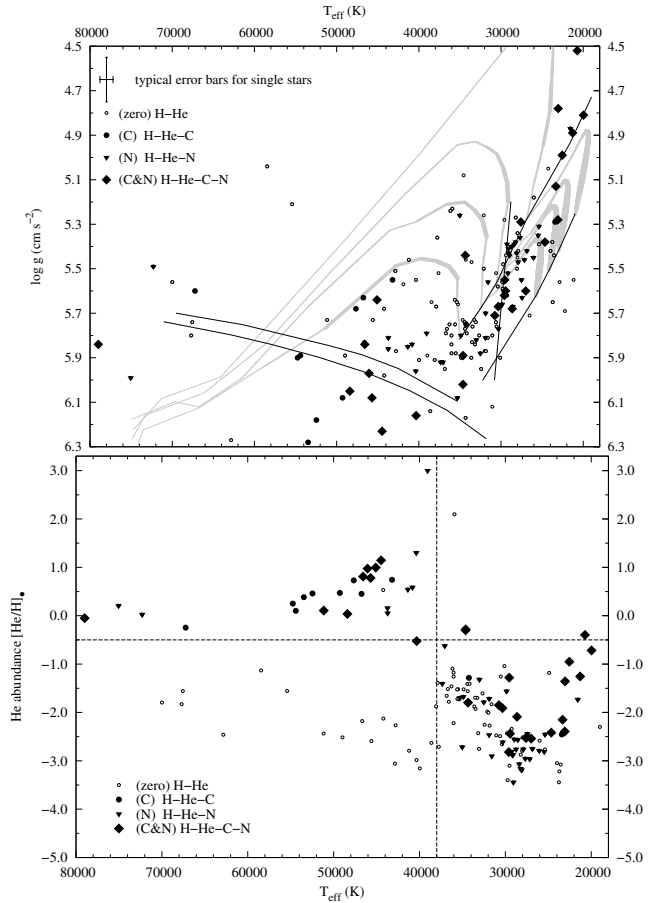


Figure 8. Metal abundances in the $T_{\text{eff}} - \log g$ and $T_{\text{eff}} - \text{He}$ diagrams.

in the case of He. In sdB stars both C and N show large variations, although a higher N abundance in cooler sdB stars is apparent. Towards higher He abundances, starting at $[\text{He}/\text{H}]_{\bullet} \approx -1$, He-sdB stars nicely connect sdB and He-sdO stars (Ahmad & Jeffery 2003) and show a higher C and N abundance than sdB stars. Unlike in sdB stars, the He abundance in He-sdO stars decreases with increasing effective temperature. Therefore, in the direction of increasing He abundances, we observe the hottest He-sdO stars first, and finally, we see the most He abundant and cooler He-sdO stars. We observed a similar trend for the C and N abundances as well. Due to this different population, an abundance drop is observed at $[\text{He}/\text{H}]_{\bullet} \approx 0$, which is followed by a steady abundance increase with increasing He abundance. These trends reach a peak at $[\text{C}/\text{H}]_{\bullet}, [\text{N}/\text{H}]_{\bullet} \approx -1$ and were fitted with a dashed line in panel *d* for the C abundance:

$$[\text{C}/\text{H}]_{\bullet} = 1.72(\pm 0.23) [\text{He}/\text{H}]_{\bullet} - 3.55(\pm 0.17) \quad (5)$$

and with a dash-dotted line in panel *e* for the N abundance:

$$[\text{N}/\text{H}]_{\bullet} = 1.00(\pm 0.13) [\text{He}/\text{H}]_{\bullet} - 3.16(\pm 0.18), \quad (6)$$

respectively. These fits suggest that He-sdO stars with a low He abundance are either C-rich or N-rich. Over $[\text{He}/\text{H}]_{\bullet} \approx 0.55$ both C and N is present in the spectra and C is more abundant. Finally, the most He abundant He-sdO stars show only N in their spectra. The hottest sdO stars complicate the trend, but it can be seen that towards higher He abundances (lower temperature) the N abundance progressively remains below the C abundance. The ratio of these two elements has important connections with formation theories. In the case of the extremely He-rich star J0851-1712 we could not

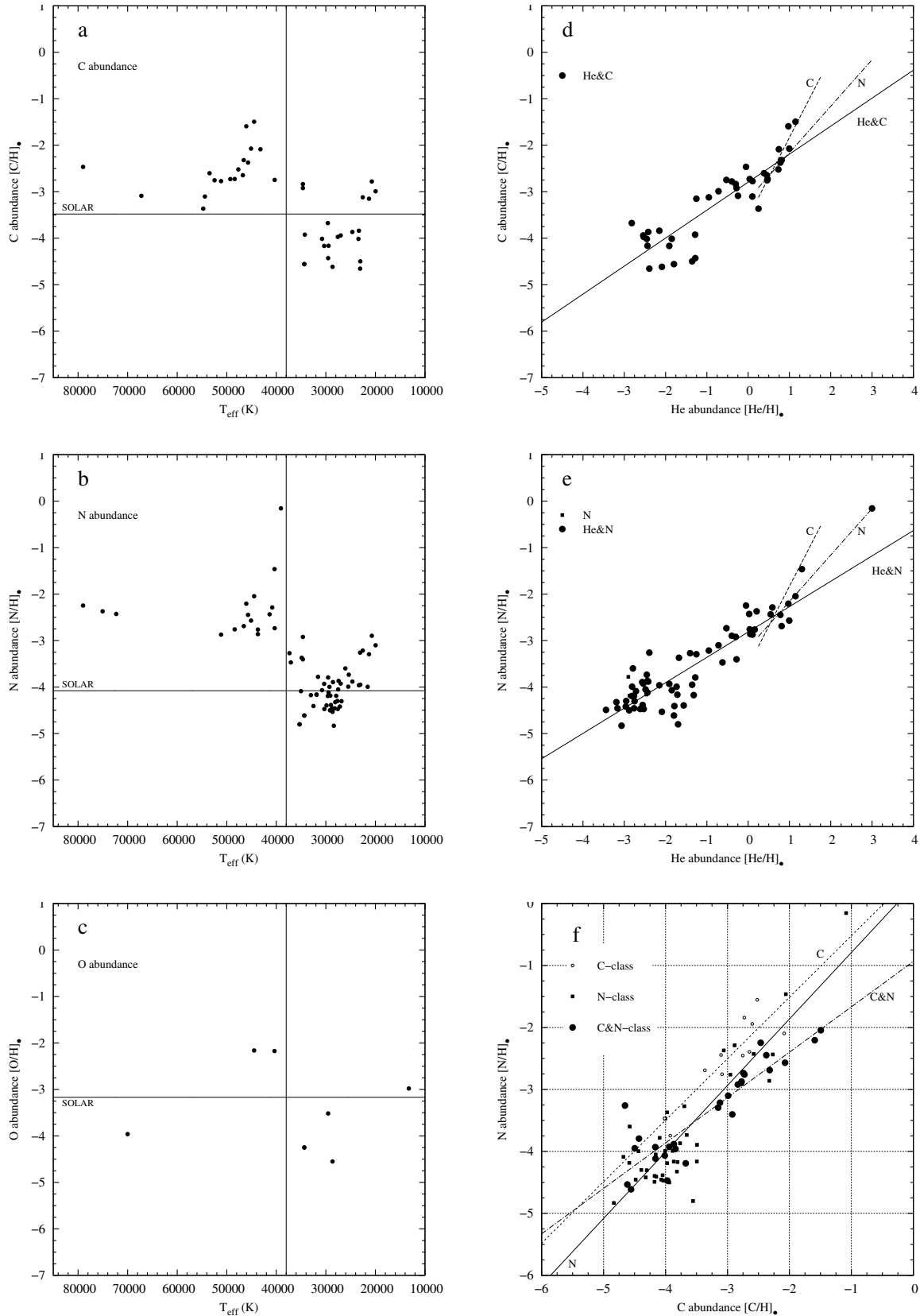


Figure 9. Panels *a*, *b* and *c* show the measured C, N and O abundances with respect to effective temperature. A vertical line at 38 000 K separating sdB and sdO stars is overplotted as well as the solar abundance for each element with a horizontal line. Panels *d* and *e* show correlations between the C, N and He abundances. In panel *f*, the C–N abundance correlations are shown, trends are fitted for N-rich stars (full line), C-rich stars (dashed line) and both C- and N-rich stars (dash-dotted line).

determine an upper limit to the He abundance to support this trend. For such He dominated stars and He-sdO stars in general, it might be worth considering changing the reference element to He because abundances relative to H may show extreme values merely due to the vanishing H in the atmosphere.

In panel *f* the N abundance is plotted with respect to the C abundance. The three lines show the linear fits to stars that show a C (dashed line), N (full line) and both C and N abundances (dash-dotted line). While data for C or N-rich stars independently show about the same abundances in He-sdO stars, stars near the C–N peak that show both C and N simultaneously suggest a C to N ratio of about ~ 3 . Considering the asymmetric errors of our abundance determination (see Appendix A) this number is a lower limit. The same trend predicts a N overabundance in the coolest sdB stars. We found equilibrium abundance at $[C/H]_{\bullet}, [N/H]_{\bullet} \approx -3.5$ that corresponds to $[He/H]_{\bullet} \approx -1.25$; just above the group of possible short period sdB pulsators in the temperature–He-abundance diagram. C&N-class objects are C-rich above this He abundance and N-rich below. Based on the number of detections the C and N abundance peaks of He-sdO stars are also recognisable in panel *f* near $[C/H]_{\bullet} \approx -2.5$ and $[N/H]_{\bullet} \approx -2.3$, respectively. We note that our C abundance determination in some cases has asymmetric errors and the N abundance has large errors making the derivation of fine details difficult. However, our observations confirm the C&N classification scheme of He-sdO stars. Interestingly, the most He abundant star (J0851-1712) showed a N abundance, but we could not determine a C or O abundance. It might belong to the N-class. Zhang & Jeffery (2012) showed that WD mergers can produce such abundance patterns. Their slow mergers are predicted to be N-rich and populate the low-mass end of the HeMS around $T_{\text{eff}} \approx 41\,000$ K. In turn, fast mergers are expected to be C-rich with higher masses around $T_{\text{eff}} \approx 45\,000$ K. Their composite model retains both elements with N overabundance in low-mass and C overabundance in high-mass He-sdO stars. Such C enrichment can be explained by the standard hot-flasher scenario as well, for He-sdO stars it predicts a C/N ratio in the range of ~ 0.85 to ~ 9.5 (Miller Bertolami et al. 2008) in agreement with our observations.

In Appendix A we show upper limit determinations and error bars. These graphs show even more similarities with the He abundance distribution, but a deeper look reveals some differences as well. The appearance of the C-weak and N-weak sequences is remarkable. The C–N peak shows a structure: C shows a peak at $T_{\text{eff}} \approx 46\,000$ K and overabundant compared to N up to $T_{\text{eff}} \approx 55\,000$ K, while N shows a peak at $T_{\text{eff}} \approx 42\,000$ K and decreases with increasing temperature faster than C. This structure has already been observed in He-sdO stars (Hirsch 2009) and was investigated in the case of double He-WD mergers (Zhang & Jeffery 2012). From the model analysis of Hirsch (2009) we found a mean temperature of $\sim 44\,600$ K for C-rich and $\sim 40\,600$ K for N-rich He-sdO stars, in agreement with our results. In the hottest He-sdO stars ($T_{\text{eff}} > 60\,000$ K) we were able to determine N and found a slight anti-correlation with the He abundance unlike at lower temperatures. Our O determination is not yet reliable to derive such trends, but a correlation with the He abundance is possible.

The boundary that separates rapid and slow sdB pulsators (dash-dotted line in the top panel of Figure 8) correlates with the observed abundance patterns. Suspected rapid pulsators near $33\,500$ K are He-rich and do not show metal traces, while slow pulsators around $28\,000$ K are He-poor and many show a N abundance. We found 27 stars in the temperature-gravity region of known rapid pulsators. Out of the 27 stars, we found a N abundance in six (~ 22 per cent). Similarly, we found 23 stars at the location of known

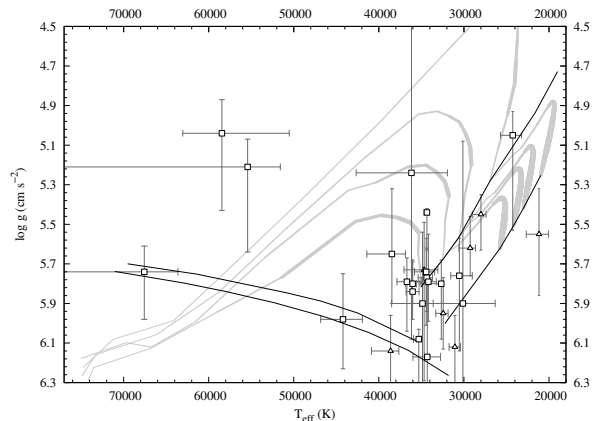


Figure 10. Same $T_{\text{eff}}-\log g$ diagram as Figure 4, here showing only composite spectra binaries. A crowding of composites can be observed near the location of possible rapid pulsators at $T_{\text{eff}} = 33\,500$ K, $\log g = 5.8$.

slow pulsators and 16 (~ 70 per cent) of these show a N abundance. In between these groups, where hybrid pulsators are expected, we found both C and N in most of the stars. Interestingly, flashless evolutionary tracks by Hu et al. (2008) connect the group of C&N class sdB stars with C&N class high gravity He-sdO stars. Recently, Geier et al. (2012) found a He isotope anomaly (${}^3\text{He}$ is strongly enriched in the atmosphere) in eight stars in a sample of 46 sdB stars. These stars are situated in a narrow strip in the temperature-gravity plane between $27\,000$ and $31\,000$ K, where we see C&N class sdB stars in our survey. No connection has been found in earlier studies between surface abundance patterns and pulsational instability (O’Toole & Heber 2006b). However, we observed different He, C, and N contents along the EHB that might play a role and need further investigations.

4.4 Binaries

Figure 10 shows the distribution of subdwarfs in composite spectra binaries in the temperature-gravity plane. We did not find He-sdO stars in such binaries. Based on the Ca infrared triplet Aznar Cuadrado & Jeffery (2001) and Aznar Cuadrado & Jeffery (2002) found that companions from composite spectra are in the range of $0.8-1.2 M_{\odot}$ F–G type MS or subgiant stars. We confirm this observation and list the results of our binary decomposition in Table 4. Monochromatic flux ratios are listed in Table 5 for the companion stars at the effective wavelengths of the broadband Bessell filters (Bessell 2005). In parentheses we also give predicted flux ratios that were derived from the synthetic subdwarf spectrum and companion template outside our observed spectral range.

Before starting spectral decomposition we always performed a single star fit and used the results in the input of the binary model. This allowed us to estimate the shifts in subdwarf atmospheric parameters during decomposition with respect to a single star fit. We emphasise that the relative shifts in Table 4 are specific to our modelling and fitting method that does not make assumptions for the companion types. Temperature shifts show large variations with an average of ~ 1300 K increase. Surface gravity shows a stronger correlation, with an average 0.7 dex increase. Similar strong correlation can be observed in the He abundance shifts. On average a 0.42 dex increase with a small scatter is indicated by the spectral decomposition of the 14 stars in which He was measurable in both the single star and binary fits. Spectral decomposition helped to achieve a He abundance measurement in four cases while in six

Table 4. Parameter shifts during decomposition. He abundance determination from upper limit to positive identification (normal font), upper limit before–after (italic font) and positive identification before–after (bold font) are distinguished. Companion absolute V magnitudes are derived from spectral types and from binary decomposition for subdwarfs. Absolute magnitudes of binary components allowed to estimate distances.

GALEXJ	ΔT	$\Delta \log g$	$\Delta[\text{He}/\text{H}]$	Type	$M_{V,\text{sd}}$	$M_{V,\text{comp}}$	d (pc)
004759.6+033742B	2420	0.90	-0.347	sdB–F6V	3.95	3.6	750
011525.9+192249B	2860	0.96	<i>0.265</i>	sdB–F2V	3.65	2.9	1340
011627.2+060314B	1610	1.06	0.327	sdB–F6V	4.36	3.6	1040
020447.1+272903B	1580	0.30	0.090	sdB–G0IV	-	2.7	-
021021.8+083058B	3730	0.77	0.406	sdB–F2IV	-	1.6	-
022454.8+010938B	0	0.46	<i>0.309</i>	sdB–F4V	4.02	3.3	780
071029.4+233322B	8010	-0.12	0.424	sdO–F6V	2.64	3.6	2240
071646.9+231930B	-1800	-0.95	<i>0.286</i>	B–A1V?	1.57	1.0	1690
101756.8+551632B	2480	0.41	<i>0.668</i>	sdB–F5V	4.06	3.5	730
110541.4–140423B	-	-	-	sdB–F6V	5.02	3.6	440
141133.4+703736B	1800	0.75	<i>0.669</i>	sdB–F0.5V	3.17	2.6	1640
151325.7+645407B	610	0.93	0.417	sdB–G0V	5.17	4.4	990
152513.0+605321B	150	0.59	0.211	sdB–G0V	4.33	4.4	710
160209.1+072509B	70	0.20	0.464	sdO–G0V	3.83	4.4	1820
161902.7+483144B	5730	0.87	-	sdB–F0V	3.46	2.6	1710
173651.2+280635B	-	-	-	sdB–F7V	4.71	3.9	390
175340.5–500741B	-470	0.75	0.703	sdB–F7V	4.52	3.9	780
202027.2+070414B	-590	0.93	0.690	sdO–F3V	3.33	3.1	2060
202059.8–225001B	-950	0.15	0.121	sdB–G0V	4.38	4.4	430
202216.8+015225B	2300	0.77	0.441	sdB–F6V	4.34	3.6	1020
203850.2–265747B	-1550	0.14	0.606	sdO–G3.5III	1.95	0.95	1830
210031.7+145213B	2370	0.76	0.498	sdB–F5.5IV-V	4.54	3.5	970
212424.3+150619B	-270	0.42	0.396	sdB–F7V	4.00	3.9	940
213730.9+221908B	-1770	0.48	-0.009	sdB–G1V	4.03	4.5	1010
214022.8–371414B	-840	0.77	0.239	sdB–F6V	4.15	3.6	870
222758.5+200623B	2540	0.85	0.930	sdB–F5V	4.98	3.5	300
232917.9+325348B	3850	1.27	-0.067	sdB–F4V	4.37	3.3	930
233158.9+281522B	-290	0.38	<i>0.994</i>	sdB–F8V	3.33	4.1	1750
234903.2+411925B	-1150	1.37	-	B?–A4V	3.60	1.7	480
Average	1306	0.67	0.418				
Median	610	0.76	0.420				

cases it confirmed an upper limit measurement. We adopted absolute V magnitudes based on the spectral type and luminosity class of the companions from Gray (1992). Using the flux ratios from Table 5 we calculated subdwarf absolute V magnitudes and approximate distances. The absolute magnitude distributions of subdwarfs and their companions are shown in Figure 11 and confirm a consistent spectral decomposition. F type MS stars are the easiest companions to find, hence these are the most frequent in our sample.

We did not find line asymmetries indicating a measurable radial velocity difference between the components in any of our stars. Radial velocity did not show variations in the much larger, low-resolution sample of similar composite spectra binaries of Green et al. (2008), which suggests that orbital periods must range from at least a few months to few years. Recently, Østensen & Van Winckel (2012b) measured radial velocity variations and detected orbits of eight sdB–F/G binaries. They found orbital periods in the range of 500–1200 days.

The effects of spectral decomposition of subdwarfs with F and early G type companions were found to be a positive shift in the subdwarf temperature, gravity and He abundance. In the case of late G and early K-type companions, due to the lower flux contribution, we expect lower shifts. A shift to higher gravities, hence to lower luminosities of some of these sdB stars is possible. A flux flattening and strong Na D lines can also indicate binarity. The high SNR allowed us to detect signs of such companions in the far red part

of the spectra. However, such faint stars do not contribute enough flux next to a 40–300 times more luminous subdwarf to carry out a proper decomposition. Due to the lack of strong H lines in their spectra and their low contribution, these stars are not expected to significantly affect the derived subdwarf atmospheric parameters. The binary population with late MS (K and M dwarf) companions is high according to radial velocity surveys and probably similarly high with WDs. Such companions are too faint to show resolvable spectral signatures.

Because close binaries are usually found by radial velocity surveys we checked the absolute shifts of our spectra relative to synthetic spectra. Figure 12 shows the radial velocity distribution in the GALEX sample with respect to the kinematic local standard of rest (LSR) frame. We found a two component Gaussian velocity distribution with velocity dispersions $\sigma_1 = 82$ and $\sigma_2 = 26$ km s⁻¹, and mean velocities $v_1 = -25$ and $v_2 = -3$ km s⁻¹, respectively. Half of the stars in the catalogue show a radial velocity $v_r(\text{LSR}) > 47$ km s⁻¹ and 42 show $v_r(\text{LSR}) > 100$ km s⁻¹ which, in some case, may be evidence of binarity. These stars are distinguished with the ‘rv’ flag in Table 2. Two subdwarfs (J0321+4727 and J2349+3844, Kawka et al. 2010) were found in close binaries and J1717+6757 is a double-degenerate binary (Vennes et al. 2011b) out of the 42 kinematically peculiar stars. J0716+2319 shows binarity and will be discussed in a forthcoming paper. Interestingly, four out of the 29 composites show a notable radial velocity. In fact, some stars can

Table 5. Monochromatic flux ratios ($F_{\lambda,comp.}/(F_{\lambda,comp.} + F_{\lambda,sd})$) of binary companions at the effective wavelengths of the broadband Bessell filters. Flux ratios outside our observed spectral ranges were calculated from synthetic and template spectra, these predicted flux ratios are listed in parentheses.

GALEXJ	U 3663 Å	B 4361 Å	V 5448 Å	R 6407 Å
004759.6+033742B	0.227	0.434	(0.580)	(0.672)
011525.9+192249B	0.331	0.551	(0.667)	(0.737)
011627.2+060314B	0.286	0.522	(0.669)	(0.749)
020447.1+272903B	0.058	0.153	0.271	0.371
021021.8+083058B	0.385	0.616	(0.735)	(0.799)
022454.8+010938B	0.333	0.537	(0.660)	(0.735)
071029.4+233322B	0.073	0.180	0.292	0.382
071646.9+231930B	0.564	0.637	0.629	0.633
101756.8+551632B	0.328	0.510	0.626	0.699
110541.4-140423B	(0.454)	0.685	0.787	0.838
141133.4+703736B	0.345	0.547	0.628	0.683
151325.7+645407B	0.334	0.529	0.671	0.757
152513.0+605321B	0.170	0.328	0.484	0.591
160209.1+072509B	0.094	0.231	(0.373)	(0.478)
161902.7+483144B	0.341	0.575	0.689	0.755
173651.2+280635B	(0.285)	0.523	0.678	0.753
175340.5-500741B	0.277	0.496	(0.640)	(0.724)
202027.2+070414B	0.182	0.404	(0.552)	(0.652)
202059.8-225001B	0.165	0.338	(0.496)	(0.594)
202216.8+015225B	0.295	0.522	(0.664)	(0.743)
203850.2-265747B	0.244	0.496	(0.715)	(0.806)
210031.7+145213B	0.347	0.594	(0.723)	(0.792)
212424.3+150619B	0.189	0.370	(0.522)	(0.622)
213730.9+221908B	0.112	0.232	(0.393)	(0.508)
214022.8-371414B	0.279	0.484	(0.625)	(0.712)
222758.5+200623B	0.481	0.700	(0.797)	(0.846)
232917.9+325348B	0.365	0.605	0.729	0.797
233158.9+281522B	0.090	0.199	0.330	0.430
234903.2+411925B	0.768	0.866	0.853	0.869

be hierarchical triples (Maxted et al. 2001), these require further observations.

We found eight composite spectra binaries among the 27 stars in the empirical region of rapid pulsators, while only one binary out of the 23 stars in the region of slow pulsators. The higher frequency of composite spectra binaries among possible rapid pulsators is obvious and supports the importance of binary evolution in subdwarf formation. A possible correlation between binarity and rapid pulsations requires further investigations.

Figure 13 shows the SEDs of the components in the sdO-G3.5III binary J2038-2657. The sdO dominates the flux in the UV, the subgiant emerges in the optical and dominates the infrared. The inset shows our observation, the components were smoothed to the correct spectral resolution. Our recent, high-resolution time-resolved spectroscopic follow-up revealed variable H_{α} emission in this binary.

5 LUMINOSITY AND MASS DISTRIBUTION

The GALEX sample presented here is one of the largest homogeneously analysed subdwarf sample to date, therefore we describe the cumulative luminosity distribution function (CLDF) of the 180 stars shown by the thick histogram in Figure 14. The bottom axis is the Eddington luminosity-fraction calculated from the

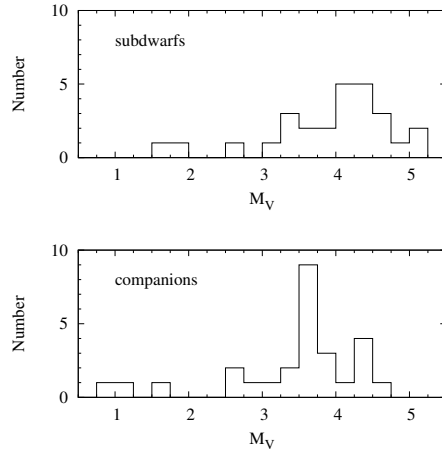


Figure 11. Absolute V magnitude distributions of hot subdwarfs and their companions.

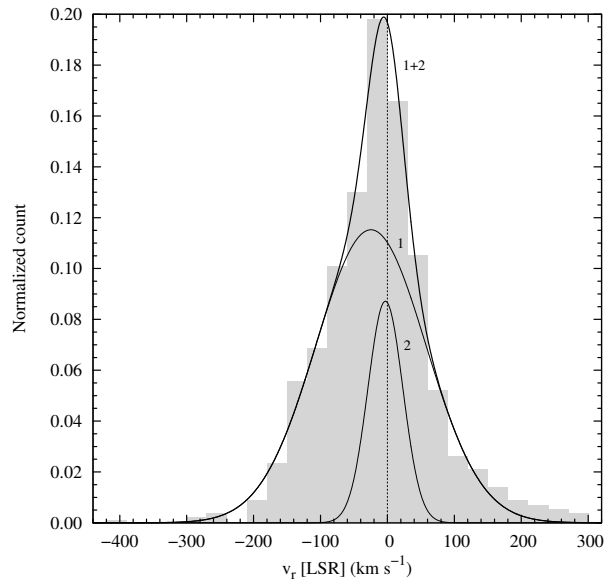


Figure 12. Velocity distribution relative to the kinematic LSR.

derived effective temperatures and surface gravities. The shaded area shows the probability density function calculated from the smoothed CLDF. The luminosity is also indicated in solar units on the top axis, assuming an average stellar mass of $0.48 M_{\odot}$. This scale is valid only for sdB stars and their descendant sdO stars, and represents a lower limit for He-sdO stars that have progressively higher masses toward higher temperatures along the HeMS (DiVine 1965, Paczyński 1971). Again, we found five well separated sections in the luminosity distribution. We identify the lowest luminosity stars below $\log(L/L_{\text{Edd}}) < -3.5$ with possible progenitors of extremely low mass WDs such as J0805-1058. The group between $-3.5 < \log(L/L_{\text{Edd}}) < -3$ consists of possible BHB stars, like J0746+0610, J1738+2634 and J2153-7004. About 55 per cent of our sample have luminosities between $-3 < \log(L/L_{\text{Edd}}) = -2.6$, we identify these with most of the sdB and some of the low-mass He-sdO stars. At higher luminosities the slope of the CLDF is defined by sdO and He-sdO stars up to $\log(L/L_{\text{Edd}}) = -2$. Finally, the most luminous sdO, post-AGB, or CSPN stars are found at $\log(L/L_{\text{Edd}}) > -1.6$. After passing their maximum light, these stars become WDs and cross the subdwarf region on their way to the

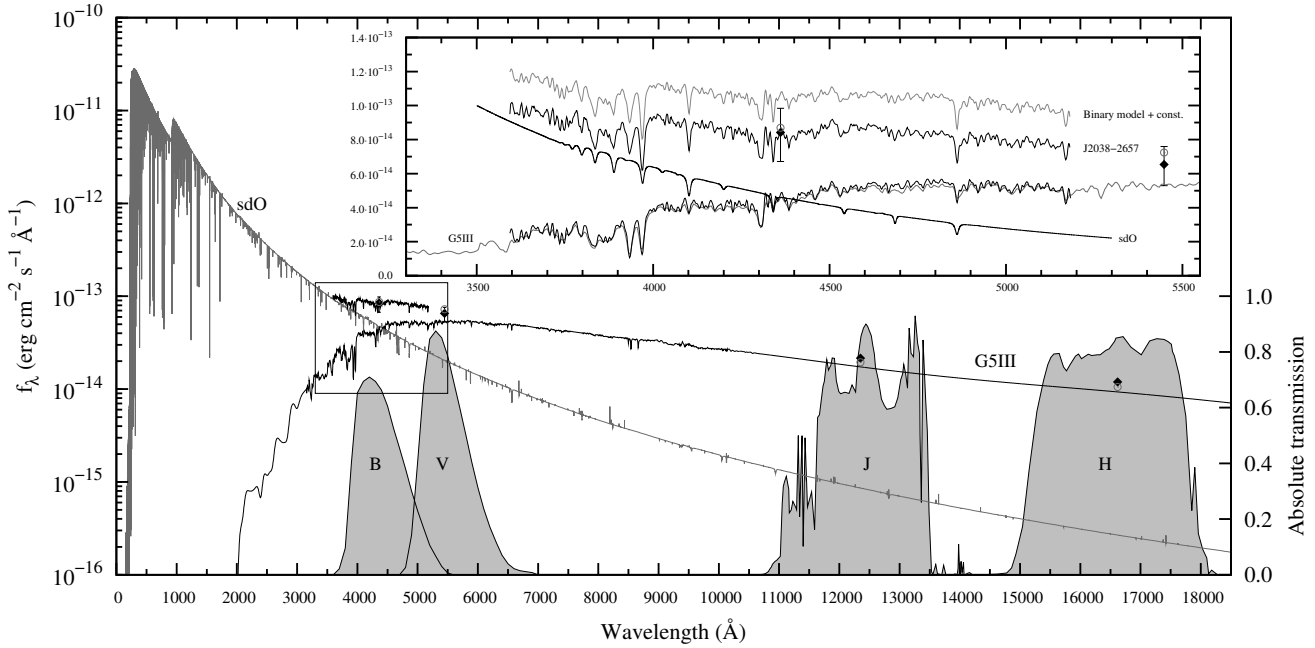


Figure 13. Spectral energy distributions of the components in J2038-2657. The TLUSTY SED for the sdO star (grey) and the G5III template from the HILIB library are marked. Bessell *B*, *V* and 2MASS *J* and *H* filter transmission curves cut out the contribution of each star to the synthetic photometry. *Inset:* Magnified part of the spectrum where decomposition was performed. The HILIB G5III template is in grey, overplotted with our interpolated MILES template in black, their match is excellent. The G5III and the sdO spectra adds up nicely and this binary model fits the observation. The binary model is shifted up for clarity. At the effective wavelengths of Bessell *B*, *V* and 2MASS *J* and *H* filters we show GSC2.3.2 (quick-*V*) and 2MASS *J* and *H* photometry with black diamonds. Data for the Bessell *B* filter is the associated optical source magnitude form 2MASS. Grey circles show our synthetic photometry.

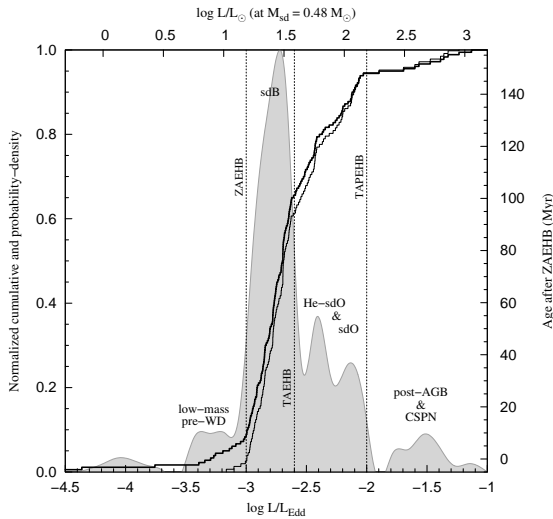


Figure 14. Luminosity distribution of 180, mostly hot subdwarf stars from the *GALEX* survey. The locations of the ZAEHB, TAEHB and terminal age post-EHB (TAPEHB) are marked. Stellar luminosities are expressed in solar luminosity on the top axis assuming a subdwarf (sdB, sdO) mass of $0.48 M_{\odot}$. He-sdO stars show a wide mass distribution.

lowest luminosities. Two peaks at higher luminosities are noticeable. We identify the peak at $\log(L/L_{\text{Edd}}) \approx -2.5$ with He-weak post-EHB sdO stars and at $\log(L/L_{\text{Edd}}) \approx -2.15$ with He-sdO stars. These groups can be seen to separate in Figure 15, where analogously to the HRD, the distribution of subdwarfs, WDs (Eisenstein et al. 2006) and stars from the MILES library are shown in the Eddington-luminosity fraction versus temperature plane. The He content and binary frequency on the He-weak sdO sequence seems

to be different for the two sdB groups and suggests that He-rich sdB stars reach higher temperatures in their post-EHB evolution than He-poor sdB stars.

To estimate the mass-distribution in our sample we compared our observed CLDF to a synthetic CLDF calculated from the subdwarf evolutionary tracks of Dorman, Rood & O’Connell (1993). This method looks for the most probable mass-distribution to reproduce the CLDF similarly to the method of Zhang, Chen & Han (2010). The Dorman evolutionary tracks were calculated for eight core-masses at eight different surface He abundances with various envelope thicknesses, giving 137 tracks altogether. However, they do not support the entire observed temperature and gravity range. The tracks were calculated for the HB with the EHB at its hot extreme that, along with the HeMS, is only partially represented. For this reason, we fitted only stars with $-3.2 < \log(L/L_{\text{Edd}}) < -1.7$ and excluded low temperature and high gravity He-sdO stars ($T_{\text{eff}} < 45000$ K and $\log g > 5.9$). This way we also excluded possible low-mass pre-WDs in the sample that are not supported by the tracks. The CLDF of the remaining stars is shown by the thin histogram in Figure 14. Next, we trimmed the evolutionary tracks to the observed temperature and gravity range. This step was necessary, because due to the approximately constant luminosity along the HB and EHB, a wide range of temperatures and gravities can contribute to a given point in the CLDF, causing a degeneracy in our solutions. Then, from the effective temperature, surface gravity and the age from the zero-age horizontal branch (ZAHB) of the Dorman-models we calculated evolutionary tracks in the Eddington-luminosity fraction versus age plane. Next, we interpolated these tracks to a new and common age axis. Finally, we applied a χ^2 minimisation to determine the mass-distribution in the sample using the normalised weighted average of these tracks (synthetic CLDF) and fitted the observed CLDF. Such an analysis

also allows for estimating the evolutionary times on the EHB and post-EHB phases.

We assumed that our sample is complete in the observed luminosity range and well-distributed, representing the true frequencies of all subdwarf types. Our main goals were to describe the slopes and the break points of the CLDF in general. The models reproduce both sdB and sdO stars reasonably well, although they predict a slower evolution and higher luminosities for post-EHB stars. From the theoretical models we found an average EHB lifetime of ~ 100 Myr, followed by ~ 50 Myr post-EHB evolution, in contrast with Zhang, Chen & Han (2010) who found 160 and 20 Myr, respectively. The observed CLDF also suggests that the post-EHB evolution is about 50 per cent of the EHB lifetime. However, large discrepancies are expected if the observed sample is not complete or not fully described by these models. More recently, Østensen et al. (2012a) found ~ 80 Myr EHB lifetime followed by ~ 62 Myr post-EHB evolution in the case of the He-rich sdB pulsator KIC 1718290.

We found that our subdwarfs have a well defined mass distribution around $M = 0.52 \pm 0.02 M_{\odot}$. A small contribution of stars with $M = 0.48 \pm 0.01 M_{\odot}$ and a shallow distribution up to $0.6 M_{\odot}$ was also found. We would like to note that the ~ 2000 K systematic shift found for sdB stars comparing to these theoretical models would shift the CLDF for sdB stars by about ~ 0.1 unit to lower luminosities. This adjustment would shift the mass distribution of sdB stars to considerably lower masses by about $0.1 M_{\odot}$.

By applying theoretical models to the SPY sdB and sdO data Zhang, Chen & Han (2010) derived the number of sdO stars evolved from sdB stars to be observationally 12 per cent. Using our spectral classification criteria and the class separation in the temperature He abundance diagram (Figure 6) we found 120 sdB and 15 sdO stars, or about 12.5 per cent that are possible post-EHB stars.

6 MODELLING HOMOGENEITY

Systematic shifts inevitably arise when data from different instruments are modelled with various model atmosphere codes. To decrease such shifts in the atmospheric parameters of subdwarfs some aspects need consideration, such as: various modelling assumptions and implementations, different atomic data, various fitting methods and error estimations can all introduce systematic differences. Therefore, independent model atmosphere analyses on large and homogeneous datasets, like the HS, SPY and SDSS data would be desirable with various modelling and fitting codes to find systematic offsets and their reasons.

Beyond homogeneous modelling and fitting techniques, consistent atmospheric parameters would require homogeneous data as well (similar SNR, resolution, spectral range). This requirement is difficult to comply due to observing time restrictions. For this reason a careful reduction is important, in particular, to apply a correct dispersion solution because even small departures from linearity or an incorrect radial velocity correction can change the parameters considerably. We found the effects of instrumental resolution and its variation along the dispersion axis to be very important. Therefore, we measured the resolution of our spectra in the middle of the available spectral range using arcs. In spite of a careful reduction and analysis, Figure 16 shows systematic shifts between different resolution data. We conclude that it is important in the future to obtain higher resolution data and to measure and model the variations of spectral resolution for each spectrum in the entire spectral range.

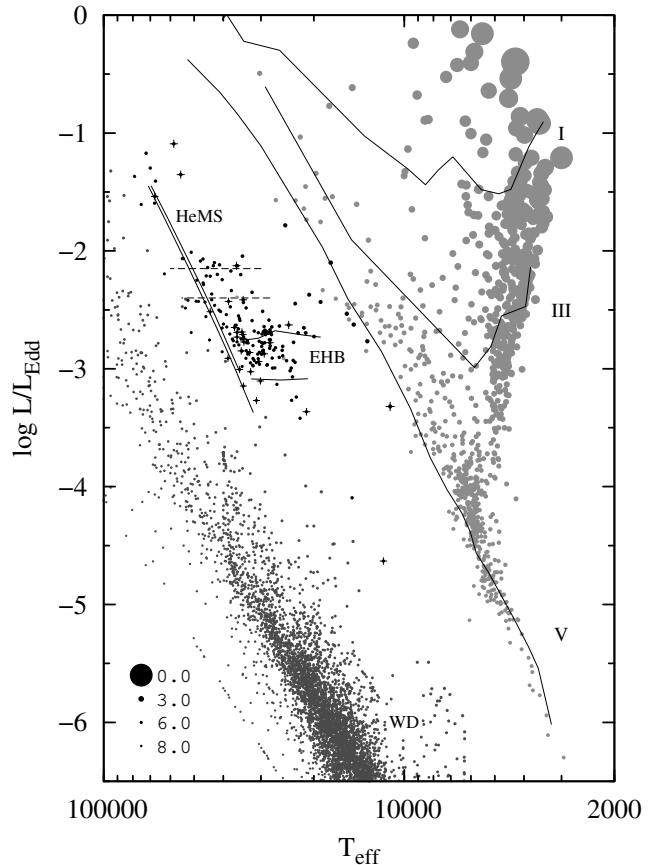


Figure 15. $T_{\text{eff}} - \log(L/L_{\text{Edd}})$ distribution of stars in the MILES library (light grey), WD sample ($\log g > 6$) from SDSS DR4 (Eisenstein et al. 2006, dark grey) and the GALEX subdwarf sample (black). The EHB, HeMS and WD sequences and three luminosity classes from Kurucz (1993) are marked in the figure. Point sizes are proportional to the inverse of surface gravities (point size = $2/(\log g + 1)$) for the sake of clarity. Composites from the GALEX sample are marked with crosses.

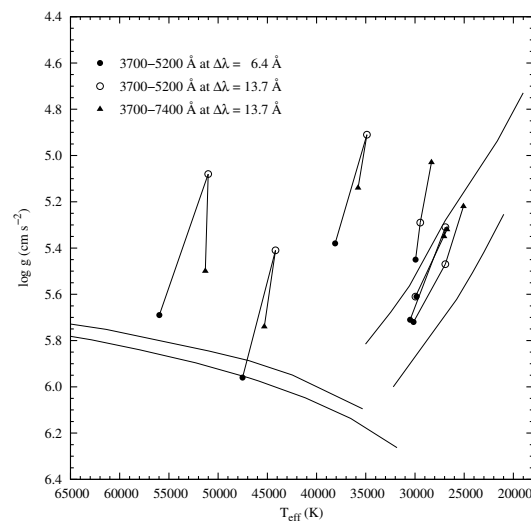


Figure 16. Systematic shifts in the temperature-gravity diagram between NTT EFOSC2 observations at different resolutions and/or spectral coverage. Data points of the same stars are connected. We measured $\Delta\lambda = 6.4$ Å for grism #7 (3700 – 5200 Å) and $\Delta\lambda = 13.7$ Å for #11 (3700 – 7400 Å). The different spectral window and low-order variations in the resolution can result, at worst, in $\Delta T_{\text{eff}} \approx 5000$ K and $\Delta \log g \approx 0.6$ systematic shifts.

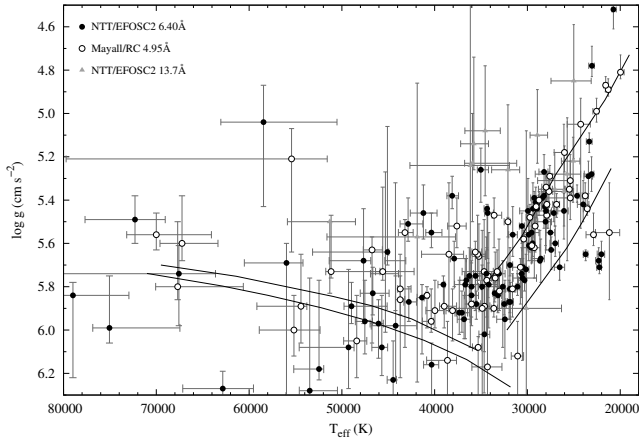


Figure 17. $T_{\text{eff}} - \log g$ diagram indicating different instruments and resolutions for all of the 191 observations. There is no correlation between instrumental setups and derived atmospheric parameters for the higher resolution data, but only less accurate parameters could be derived from the low-resolution observations.

A combination of the χ^2 and residual minimisation (or equivalent width fitting) will be implemented in XTGRID to overcome the small scale variations caused by spectral convolutions. We found that high series members of H lines (from H_δ to the Balmer-jump) are important in temperature and gravity determination and data quality is essential in this spectral range. Figure 16 shows that the observed spectral range can also be a source of systematic deviations, especially the inclusion of the H_α and H_β lines, which form higher in the atmosphere and may show non-LTE effects.

Systematic shifts that arise from different resolutions or different spectral coverage are represented in Figure 16 where we compare the parameters derived from spectra taken with grism #7 and #11 with the EFOC2 spectrograph on the NTT. Shifts from the inclusion of the H_α line or due to the strong blending of spectral lines in low-resolution spectroscopy can be seen. This problem affects 16 observations of 14 stars in our sample, seven of these stars, shown in Figure 16, have higher resolution observations as well, hence we regard the effects on our final results negligible. The higher resolution NTT and Mayall spectra provide consistent atmospheric parameters as shown in the temperature-gravity plane in Figure 17. We conclude that spectral resolution affects the derived atmospheric parameters and low resolution data provides systematically lower temperatures and gravities for sdO stars. These trends are not so remarkable in sdB stars, but considerable shifts can be found. For detailed subdwarf modelling in the optical, not just a high signal-to-noise, but medium to high resolution data is necessary ($\Delta\lambda < 3 \text{ \AA}$, or $R > 3000$).

7 SUBDWARF POPULATIONS

The observed distribution of subdwarf stars can be explained in the framework of both the canonical formation theory (Han et al. 2003a, Han et al. 2003b, Mengel, Norris & Gross 1976) and the hot-flasher scenario (Miller Bertolami et al. 2008, Lanz et al. 2004, D’Cruz et al. 1996), with an interplay between atmospheric diffusion and stellar winds (Unglaub 2008). Both theories have three formation channels that we describe in the context of our observations.

In Figure 18 we present evolutionary sketches in the $T_{\text{eff}} - \text{He}$ diagram of the canonical and hot-flasher formation models, and in

Figure 19 we show predictions if diffusion and stellar wind may change the observed He abundance.

First, we describe the branches of the canonical formation. The *common-envelope channels* (Han et al. 2003a) predict subdwarfs with low-mass MS (CE-1 channel) or WD (CE-2 channel) companions in close binaries with 0.1 – 10 days orbital periods. Such binaries are usually discovered in radial velocity surveys, because in these systems the low-mass companion is hardly visible next to a bright subdwarf. These subdwarfs are predicted to have a very thin H-rich envelope and a sharp mass distribution peaked around $0.46 M_\odot$. Our observations confirm a population near 28 000 K and $\log g = 5.45$.

Hotter and more helium abundant sdB stars near 33500 K and $\log g = 5.8$ are predicted by the *Roche-lobe overflow channel* (ROFL-1, Han et al. 2003a). These stars are expected in wide binaries with $1 - 2 M_\odot$ companions, 400 – 1500 days orbital periods and with thin H envelopes. The location of possible rapid pulsators in our survey coincides with this population and shows a higher composite frequency. Interestingly, the rapid pulsator class-prototype, EC 14026-2647 itself, and the three rapid pulsators discovered later are all in very similar composite spectra binaries (O’Donoghue et al. 1997).

He-sdO stars may form by *WD binary mergers* (Zhang & Jeffery 2012). This channel would intrinsically explain single subdwarf stars that are expected to show He dominated atmospheres enriched in CNO-processed nuclei. Following the He core-flash these stars evolve through small loops (few 1000 K) in the temperature-gravity diagram of Zhang & Jeffery (2012) and reach their locations at various temperatures depending on their C and N abundance. Binary merger channels have been proposed with low-mass stars as well as with substellar companions (Soker 1998). The merger theory assumes a large rotational velocity of the progeny that is not generally observed in single subdwarf stars. Geier et al. (2009) found $v_{\text{rot}} \sin i < 10 \text{ km s}^{-1}$ for ~ 100 single sdB stars. However, Lanz et al. (2004) found large rotational velocities for two C-rich sdB stars (PG 1544+488 and JL 87) and Hirsch, Heber & O’Toole (2008) found two out seven sdO stars having a projected rotational velocity in excess of 20 km s^{-1} . Recently, Geier, Classen & Heber (2011b) found EC 22081-1916 a single sdB star that is a fast rotator with $v_{\text{rot}} \sin i \approx 150 \text{ km s}^{-1}$ and most probably a merger product of a WD and a substellar companion. In close binaries tidal spin-up can cause such high rotational velocities. [Note added in proof: After this paper has been accepted, Vennes et al. (2012) reported that one of our targets (J1411-3053) is a fast rotating sdB star ($v_{\text{rot}} \sin i = 164 \pm 5 \text{ km s}^{-1}$) in a short period sdB-WD binary.] A targeted radial and rotational velocity study would be helpful to constrain the properties of our subdwarfs and investigate the merger channel.

The hot-flasher scenario (Miller Bertolami et al. 2008) also predicts three major groups of subdwarfs. In the *early hot-flasher* channel the core-flash occurs after the star leaves the RGB, during the constant luminosity phase and hot subdwarfs are predicted with standard H/He envelopes. Possible rapid pulsators in our catalogue show such atmospheres; they are He enriched and have notably less CNO in their atmospheres. The *late hot-flasher (shallow mixing)* theory assumes a core-flash early after the star reached the WD cooling track. This concept predicts a He and N enriched H atmosphere, similar to possible slow pulsators or cooler He-sdO stars in our sample. The *late hot-flasher (deep mixing)* predicts strong He, C and N enrichment, exactly as we found in the case of hotter He-sdO stars. All these features can be observed in Figure 8

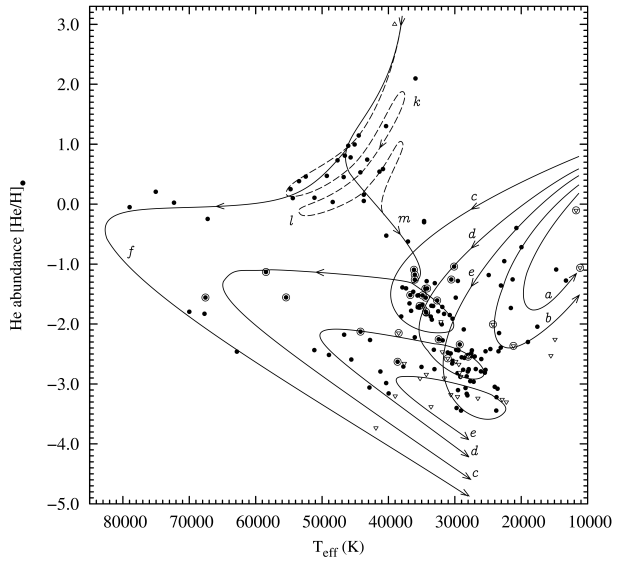
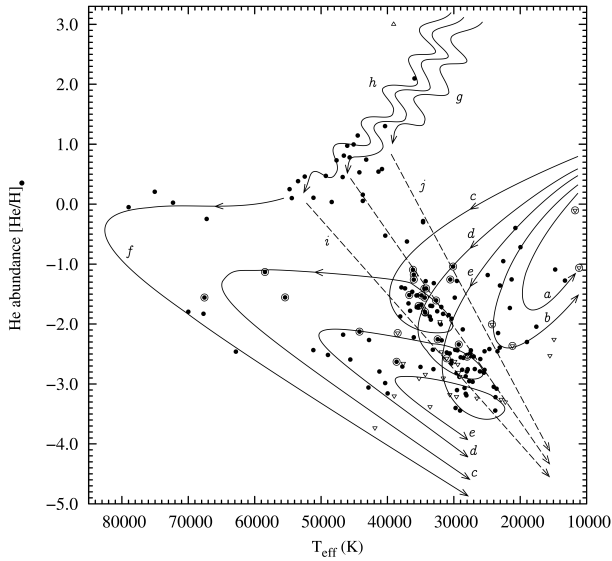


Figure 18. Possible evolutionary sketches for sdB, sdO and He-sdO stars based on our observations and the predictions of the canonical (*left*) and hot-flasher (*right*) scenarios.

and 9 as well. In the hottest sdO stars we found signs of increasing abundances of C and N with temperature.

Since the evolution from the primary He core-flash to the EHB or HeMS is about 40 times shorter than the evolution on the EHB, stars are expected to group around the EHB or the HeMS. Such an accumulation is not observed for He-sdO stars. This may suggest that these subdwarfs evolve through the HeMS in large numbers without slowing down, which is physically impossible. Hence we conclude that they show more diverse atmospheric parameters before settling on the EHB as sdB stars or starting their evolution towards the WD cooling sequence.

The left panel of Figure 18 shows evolutionary sketches in the $T_{\text{eff}} - \text{He}$ diagram based on our observations and the predictions of the aforementioned canonical studies. The distribution of sdB and He-weak sdO stars can be explained according to the canonical theory. Convection and rotation on the HB are significant below 11 500 K. BHB stars show a decreasing He abundance with surface temperature until core He burning is on. After core exhaustion, these stars evolve towards the AGB and lower surface temperatures. Along this evolution the He abundance is expected to increase as shown by lines *a* and *b* in Figure 18. In sdB stars He is sinking to about 24 000 K (O’Toole 2008). Over 24 000 K the increasing UV flux starts to bring He to the surface and steadily increases the He abundance until about 36 000–38 000 K where core He burning stops. In stars with a lower He abundance (thicker H envelopes and larger total mass) this happens at lower temperatures. Canonical models then predict a fast evolution to higher temperatures. After passing a maximum temperature, stars cool and He sinks again, these post-EHB stars rapidly evolve to WDs. We sketched and labelled this evolution with lines *c*, *d* and *e*.

The canonical formation of He-sdO stars (Zhang & Jeffery 2012) predicts different channels depending on the merger type. Assuming He-WD binaries it predicts C and N enriched He-sdO stars in agreement with our observations. In Figure 8 He-sdO stars separate in temperature according to their C and N abundance. If these stars belong to the HeMS, this separation suggests a different average stellar mass as well. Following the He core-flash the slow merger model includes accretion from a debris disc and pre-

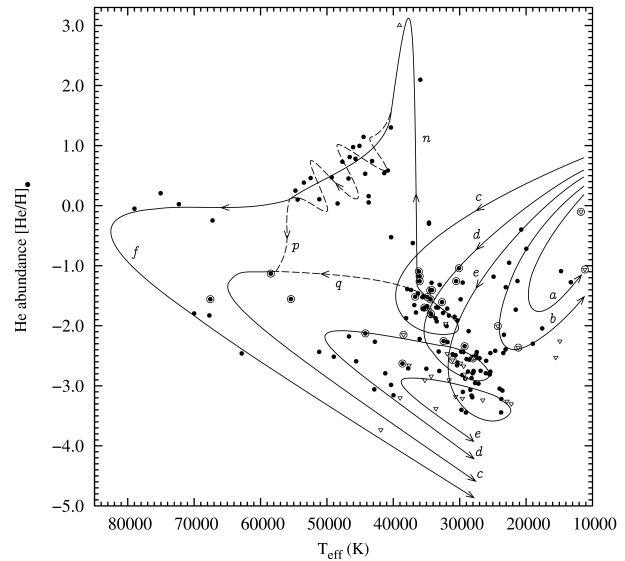


Figure 19. Evolutionary sketches for sdB, sdO and He-sdO stars based on our observations and theoretical predictions with atmospheric mixing and stellar winds.

dicts N-rich low-mass He-sdO stars (line *g*). The fast merger model involves a period of coronal accretion and predicts higher mass C-rich subdwarfs (line *h*). The composite model predicts a similar abundance pattern, but a broader mass distribution where low-mass He-sdO stars are enriched in N and high mass stars are enriched in C, hence this evolution proceeds between the slow and fast merger tracks. After core He exhaustion they may evolve directly to lower temperatures and abundances as indicated by the dashed lines *i* and *j*, or reach a maximum temperature before joining the WD cooling tracks (line *f*).

The right panel of Figure 18 shows evolutionary sketches based on the hot-flasher scenario of Miller Bertolami et al. (2008). This predicts an evolutionary link between He-sdO, the hotter sdB and He-weak sdO stars (line *m*). The different binary frequency of

He-sdO and sdB stars implies a mixed sdB population, therefore we repeat the sketches for the canonical evolution (lines *c*, *d* and *e*) that may contribute to sdB stars. The early hot-flasher and late hot-flasher (shallow mixing) channels may also contribute to the mixed sdB population. The hot-flasher formation of He-sdO stars predicts larger loops (dashed lines) from He shell-flashes than the canonical theory, extending to 10 000 K. These loops might cover the entire temperature range of He-sdO stars in our sample. Along these loops stars may cross the wind limit and show changing enhancements of C and N. In light of the hot-flasher scenario, our observations imply that stars after a He shell-flash may show C enriched atmospheres (*l*) that may transform to N-rich CNO processed atmospheres in their cooler phase (*k*). After these transients stars either move towards higher temperatures (line *f*) or settle on the EHB among suspected rapid pulsators and join the canonical evolution of the hotter sdB stars (line *c*).

Between 36 000 and 40 000 K a photospheric convective mixing is predicted over $\log g \approx 5.9$ increasing the He abundance until no H is measurable (Groth, Kudritzki & Heber 1985) as shown by line *n* in Figure 19. This mixing makes the tracking of formation theories difficult and might be responsible for the atmospheric properties of He-sdO stars. These stars may cross the wind limit periodically and transient He enhancements (dash-dotted line) may occur while stars drift to higher temperatures. With this evolution to higher temperatures the C/N ratio is steadily increasing according to our observations. Convection ceases around 45 000–52 000 K and He sinks again (O’Toole 2008). As a result, He-sdO stars may return to the canonical evolution indicated by line *c* through dashed line *p*, or reach a maximum temperature and follow line *f*. The gap between 40 000 and 54 000 K at $[\text{He}/\text{H}]_{\odot} \approx -1.5$ coincides with the He-sdO region in our sample suggesting that most of the He-rich sdB stars may either pass through very fast (dashed line *q*), or suffer a huge metal abundance increase upon entering this region. A larger sample could help to statistically confirm the existence of this empty region. A period of deep atmospheric mixing can also explain the high ^3He concentrations observed at some subdwarf stars (Heber 2009). Due to a high temperature gradient in subdwarf atmospheres the *pp*-chain can produce this isotope relatively close to the photosphere. Because the equilibrium abundance of ^3He is much higher at low temperatures, ^3He produced in deeper layers may accumulate and replace ^4He in the atmosphere if diffusion brings it to the surface.

Progenitors of low-mass WDs evolve through the parameter region occupied by subdwarfs. Figure 20 shows evolutionary tracks for different stellar masses taken from Driebe et al. (1998). Evolutionary time-scales are inversely proportional to line widths in order to emphasise regions where an accumulation of stars is expected. Such low-mass pre-WDs are conceivable in our sample, in particular among He-weak sdO stars, but, in general, the distribution of our subdwarfs does not confirm a significant fraction of such low-mass, non-core-He burning stars.

These interpretations can qualitatively relate our observations to the various subdwarf evolutionary theories, but deeper investigations are necessary on a larger sample to estimate the contribution of the channels of different subdwarf formation theories as well as the role of diffusion and mass-loss.

8 CATALOGUE OF SUBLUMINOUS STARS

The catalogue in Table 2 and 3 contains 191 observations of 180 subluminoous field stars sorted according to increasing right as-

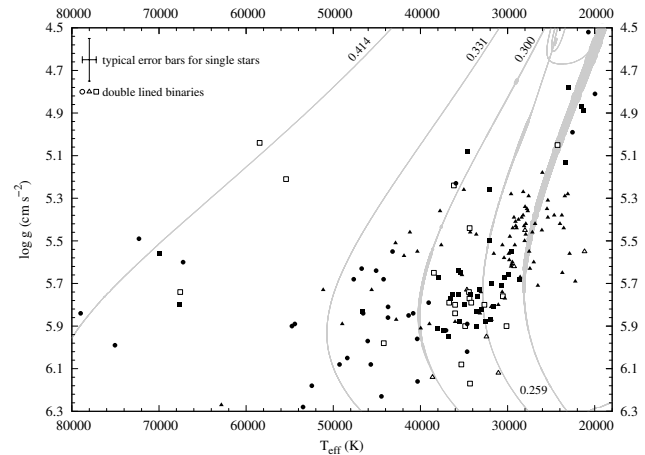


Figure 20. Low-mass He WD evolutionary models from Driebe et al. (1998). Tracks for 0.259, 0.300, 0.331 and 0.414 M_{\odot} are overlaid and labelled with the stellar mass. The 0.259 M_{\odot} track crosses this region twice following a He shell-flash.

cension. In resolved binaries the primary and the companion are labelled with *A* and *B* suffixes, respectively. Our observations are typesetted with bold and MILES templates with normal font. We list *GALEX* N_{UV} and GSC2.3.2 *V* magnitudes taken from the GSC quick-*V* photometry. Atmospheric parameters like effective temperature, surface gravity, He and CNO abundances are listed for subdwarfs and only effective temperature, surface gravity and metallicity for companions. The interstellar reddening was estimated towards each target and we list the values of the derived $E(B - V)$ colour excess. The $V - J$ and $J - H$ colour indices were calculated from 2MASS photometry. In parenthesis, we give synthetic colour indices calculated from TLUSTY SEDs and HILIB templates in a similar fashion like in Figure 13. Because of the higher uncertainties in the *V* magnitudes the $J - H$ colour indices are more reliable. Our comments are abbreviated with flags and these are explained in Table 6. We performed a cross-correlation of our subdwarf list with SIMBAD⁶ and The Subdwarf Database⁷ (Østensen 2004, Østensen 2006). In SIMBAD a search radius of 1 arcminute was used. Resolved stars are marked with one of their common identifiers in the last column. Ambiguous identifications are appended with a question mark. Out of the 180 stars we found 32 in the PG, 16 in the First Byurakan Survey (FBS, Mickaelian 2008), 6 in the HS, 3 in the Edinburgh-Cape (EC, Kilkenny, O’Donoghue & Stobie 1991) and 2 in the Hamburg-ESO Survey (HE, Wisotzki, Reimers & Wamsteker 1991) catalogues. We cross-correlated our data with the list of subdwarf pulsators in Østensen et al. (2010) as well, but no match was found. A cross-correlation with Geier et al. (2011a) in search for close-binaries revealed only the two known short-period binaries: J0321+4727 and J2349+3844, already discussed in Kawka et al. (2010).

8.1 Comments on individual stars and overlaps with other catalogues

The new analysis confirms our previous results on *PG 0314+146* (He-sdO), *PG 0838+133* (He-sdO), *PG 1432+004* (sdB) and *PG*

⁶ <http://simbad.u-strasbg.fr/simbad/>

⁷ <http://catserver.ing.iac.es/sddb/>

Table 6. Flags that are used in the comments of Tables 2 and 3.

Flag	Meaning
c	- Contamination, scattered light from a nearby star.
t	- See text; further details can be found in Section 8.1.
#7, #11	- Spectral resolution; #7: ESO/NTT/EFOSC2, grism #7, $\Delta\lambda = 6.4 \text{ \AA}$. #11: ESO/NTT/EFOSC2, grism #11, $\Delta\lambda = 13.7 \text{ \AA}$. If resolution is not given: NOAO/Mayall/RC, grating KPC-10A, $\Delta\lambda = 4.95 \text{ \AA}$.
d	- Binary decomposition degeneracy: components are either similar type, or a high metallicity single line binary.
b	- Spectral signatures of a cool companion.
rv	- Radial velocity with respect to the kinematic LSR is over 100 km s^{-1} .
RV	- Radial velocity curve proves a close binary, references are given in footnote.
f	- Poor fluxing below 4500 \AA .
ca, na	- Ca II H&K or Na I D lines; indicating either a cool companion or interstellar absorption.
he	- He I/He II line inconsistency.
M	- Data is taken from the MILES library.
C&N	- C&N $\lambda 4640 - \lambda 4665 \text{ \AA}$ blend.
s	- Possible slow pulsator
r	- Possible rapid pulsator

1629+081 (sdB). The new fitting method provides consistent results with Paper I.

J0047+0958 (HD 4539) was observed with NTT and is one of the two subdwarfs in the MILES library observed with the 2.5m Isaac Newton Telescope at 2.3 \AA resolution. It is the brightest star in our sample with $V = 10.24$ magnitude. Cenarro et al. (2007) determined $T_{\text{eff}} = 25\,200 \text{ K}$ and $\log g = 5.40$ in good agreement with our $T_{\text{eff}} = 24\,650^{+590}_{-200} \text{ K}$ and $\log g = 5.38^{+0.03}_{-0.05}$. Then, we refitted the MILES spectrum with our method and found $T_{\text{eff}} = 24\,000^{+180}_{-380} \text{ K}$ and $\log g = 5.21^{+0.03}_{-0.04}$. From the higher resolution data we derived slightly lower temperature and gravity for this star.

J0059+1544 (PHL 932) was suspected to be the central star of a planetary nebula. Therefore, it has been targeted by numerous studies to reveal its connection. Frew et al. (2010) derived $T_{\text{eff}} = 33\,490 \pm 73 \text{ K}$, $\log g = 5.81 \pm 0.02$ and $[\text{He}/\text{H}]_{\bullet} = -1.58 \pm 0.03$ and concluded it is an sdB star exciting a H II region in the dense ISM. Napiwotzki (1999) derived $T_{\text{eff}} = 35\,000 \pm 900 \text{ K}$, $\log g = 5.93 \pm 0.12$ and $[\text{He}/\text{H}]_{\bullet} = -1.53 \pm 0.05$ and a mass of $0.28 \pm 0.01 M_{\odot}$. Our analysis confirms a slightly lower He abundance, we measured $T_{\text{eff}} = 33\,530^{+190}_{-310} \text{ K}$, $\log g = 5.83^{+0.04}_{-0.05}$ and $[\text{He}/\text{H}]_{\bullet} = -1.69^{+0.06}_{-0.04}$.

J0321+4727 and *J2349+3844* have been analysed before by Kawka et al. (2010). For *J0321+4727* they obtained $T_{\text{eff}} = 29\,200 \pm 300 \text{ K}$, $\log g = 5.5 \pm 0.1$ and $[\text{He}/\text{H}]_{\bullet} = -2.6 \pm 0.1$ in agreement with our measurements: $T_{\text{eff}} = 27\,990^{+460}_{-400} \text{ K}$, $\log g = 5.34 \pm 0.07$ and $[\text{He}/\text{H}]_{\bullet} = -2.52^{+0.17}_{-0.22}$, although our new temperature is slightly lower. For *J2349+3844*, we derived a lower temperature. Fitting only H α , Kawka et al. (2010) measured $T_{\text{eff}} = 28\,400 \pm 400 \text{ K}$, $\log g = 5.4 \pm 0.3$ and $[\text{He}/\text{H}]_{\bullet} = -3.2 \pm 0.1$, while we measured $T_{\text{eff}} = 23\,770^{+330}_{-350} \text{ K}$, $\log g = 5.38^{+0.05}_{-0.06}$ and $[\text{He}/\text{H}]_{\bullet} = -3.44^{+0.25}_{-0.30}$. Both stars show radial velocity variations and are confirmed binaries. Phase variation is a possible source of discrepancies in measured atmospheric parameters.

J0507-2802 (HE 0505-2806) and *J0657-7324* (CPD-73 420). For both stars we have multiple observations showing variable composite spectra and a significant IR excess. Changing compos-

ite features are also visible in their spectra. An inspection of their fields revealed crowding; both stars are visual binaries. The composite spectra is most probably the result of contamination from the nearby, but possibly independent star. Atmospheric turbulence can scatter light in the slit from these stars depending on observing conditions. In such cases the decomposition is important to remove the contamination and improve the subdwarf parameter determination, although, it is difficult due to the variability and chromatic aberration of the scattered light. Reliable parameters for the nearby star cannot be derived.

J0639+5156 was observed by Vučković et al. (2012) in a photometric campaign to look for bright pulsating subdwarfs. This star is the brightest rapid pulsator to date with a main pulsating period of 260 s and amplitude of $\sim 13.5 \text{ mmag}$ in the R filter. A slow pulsation mode with $\sim 2 \text{ mmag}$ at 1765 s period suggests the star is a hybrid pulsator.

J0806+1527 was observed by Baran et al. (2011) and found to be a hybrid pulsator with two rapid and two slow modes.

J0851-1712 (TYC 6017-419-1). We derived $T_{\text{eff}} = 39\,060 \text{ K}$ and $\log g = 5.79$ for the star, placing it at the end of the EHB on the HeMS. We did not detect H in its atmosphere while the C/N ratio remained below 0.12 and the O/N ratio below 0.54 by number with increasing He abundance. We classify this star as a N-class object. The C/N ratio of 0.05 and O/N ratio of 0.2 by number is typical for CNO processed material. Peculiar abundances can be the result of mixing, diffusion and mass-loss processes (Unglaub & Bues 2001). The atmospheric parameters of the star correspond to the region of photospheric convective mixing in the $T_{\text{eff}} - \log g$ diagram. High resolution and high signal-to-noise observations could help improving the CNO abundance determination of this exotic star.

J0934-2512. Our previous analysis in Paper I found peculiar He I $\lambda 4471/\text{He II } \lambda 4686$ line ratios inconsistent with other Balmer line spectra with similar He abundances. He II lines are relatively strong for the temperature of the star. We verified that the relevant atomic data (energy levels, oscillator strengths, line widths) in our model atoms and line lists are up-to-date for these He lines. Therefore, the cause for the observed line strength inconsistencies remains to be determined. Our new analysis showed that the star is in the post-EHB evolutionary phase in the $T_{\text{eff}} - \log g$ diagram, but belongs to the possible short period sdB pulsators in the $T_{\text{eff}} - \text{He}$ diagram. The spectrum indicates a radial velocity that does not exclude binarity. To test for a subdwarf companion we repeated our fit starting with a single star model and included a companion from the spectral library compiled from all other subdwarfs modelled in this work. We found the spectrum might be dominated by an sdB star and the He II line can be the signature of a hot, but faint companion. An underestimated temperature, gravity and He abundance could have similar effects, but would affect the entire spectrum. The true nature of the He line and surface gravity inconsistency would require high resolution spectra and radial velocity measurements. To a lesser extent such inconsistencies can be observed in six other sdB stars with various atmospheric parameters. Because of a possible degeneracy in the spectral decomposition of such binaries they are listed as single stars with flag "he" in Table 2 referring to He line inconsistency.

Table 2. Atmospheric parameters of hot subdwarf stars in the *GALEX* survey.

GALEXJ	Type	N_{UV} (mag)	V (mag)	T_{eff} (K)	$\log g$ (cm s^{-2})	Abundances, $[X/H]_{\odot}$ or $[\text{Fe}/H]$				$E(B - V)$ (mag)	$V - J$ (mag)	$J - H$ (mag)	Comments	Other name
						He	C	N	O					
003531.98+245917.22	sdB	13.61	14.16	35230 ⁺⁷⁴⁰ ₋₇₀₀	5.66 ^{+0.07} _{-0.15}	-2.91 >	-4.94 >	-4.45 >	-4.19 >	0.02	-0.474	-0.152		PG 0032+247
003639.99+375553.37	sdB	12.75	14.07	38970 ⁺⁵⁰⁰ ₋₁₃₃₀	5.89 ^{+0.10} _{-0.09}	-3.20 >	-5.10 >	-4.00 >	-4.79 >	0.01	-0.709	-0.097		FBS 0033+376
004729.22+095855.69	sdB	10.44	10.24	24650 ⁺⁵⁹⁰ ₋₂₀₀	5.38 ^{+0.03} _{-0.05}	-2.42 ^{+0.20} _{-0.07}	-3.87 ^{+0.33} _{-0.44}	-3.88 ^{+0.27} _{-0.59}	-3.81 >	0.01	-0.576	-0.123	#7,t	HD 4539
004729.22+095855.69	24000 ⁺¹⁸⁰ ₋₃₈₀	5.21 ^{+0.03} _{-0.04}	-2.25 ^{+0.07} _{-0.09}	-3.89 ^{+0.13} _{-0.22}	-3.67 ^{+0.14} _{-0.26}	-3.92 >	0.00	M,t	HD 4539
004759.62+033742.88A	sdB	11.86	12.39	38620 ⁺²²⁵⁰ ₋₉₇₀	6.14 ^{+0.22} _{-0.18}	-2.63 ^{+0.44} _{-1.17}	-4.69 >	-3.61 >	-4.13 >	0.00	0.510	0.251	#7	PB 6168
004759.62+033742.88B	F6V			6140	4.14		[Fe/H] = -0.55			0.00	(0.583)	(0.244)	M	
004917.26+205640.85	sdB	13.68	14.72	27520 ⁺⁵⁰⁰ ₋₄₅₀	5.55 ^{+0.07} _{-0.06}	-2.48 ^{+0.16} _{-0.23}	-4.16 >	-4.05 ^{+0.35} _{-0.58}	-4.11 >	0.00	-0.371	-0.062	#7,s	PG 0046+207
005956.67+154413.75	sdB	11.95	12.27	33530 ⁺¹⁹⁰ ₋₃₁₀	5.83 ^{+0.04} _{-0.05}	-1.69 ^{+0.06} _{-0.04}	-4.56 >	-3.96 >	-4.73 >	0.00	-0.426	-0.122	#7,t,r	PHL 932
011103.81+194743.73	sdO	13.35	14.46	42780 ⁺⁴⁴⁰ ₋₈₂₀	5.87 ^{+0.09} _{-0.07}	-2.27 ^{+0.17} _{-0.17}	-4.77 >	-3.51 >	-4.28 >	0.00	-0.846	-0.193	#7	PG 0108+195
011525.92+192249.86A	sdB	13.10	13.09	31060 ⁺⁶⁸⁰ ₋₆₅₀	6.12 ^{+0.20} _{-0.16}	-2.57 >	-4.02 >	-3.68 >	-3.48 >	0.03	0.428	0.086	#7	CHSS 3354
011525.92+192249.86B	F2V			6710	4.38		[Fe/H] = -0.39				(0.364)	(0.000)	M	
011554.22+261401.11	He-sdO	13.84	14.51	54410 ⁺⁴⁷⁵⁰ ₋₆₄₀	5.89 ^{+0.17} _{-0.24}	0.10 ^{+0.60} _{-0.06}	-3.10 ^{+0.29} _{-0.79}	-2.44 >	-2.15 >	0.10	-0.468	-0.082		PG 0113+259
011627.22+060314.22A	sdB	13.58	13.24	35310 ⁺⁶²⁰ ₋₃₈₀	6.08 ^{+0.24} _{-0.05}	-1.70 ^{+0.13} _{-0.13}	-3.55 >	-4.80 ^{+1.18} _{-0.66}	-3.74 >	0.06	0.926	0.169	#7	PB 6355
011627.22+060314.22B	F6V			6170	4.09		[Fe/H] = -0.15				(0.735)	(0.177)	M	
011928.88+490109.39	He-sdO	12.63	13.56	43720 ⁺⁵¹⁰ ₋₅₀₀	5.86 ^{+0.07} _{-0.21}	0.16 ^{+0.44} _{-0.05}	-2.95 >	-2.76 ^{+0.92} _{-0.21}	-2.36 >	0.04	-0.244	-0.257	C&N	
014307.50-383316.30	He-sdO	11.79	13.00	45090 ⁺⁸⁰⁷⁰ ₋₁₄₀	5.64 ^{+0.06} _{-0.38}	1.00 ^{+0.33} _{-0.36}	-2.07 ^{+1.25} _{-0.11}	-2.57 ^{+1.19} _{-0.59}	-1.87 >	0.03	-0.771	-0.074	#7,C&N	SB 705
015421.98+490521.91	sdB	13.10	13.51	32100 ⁺⁴¹⁰ ₋₂₄₀	5.50 ^{+0.52} _{-0.08}	-1.98 ^{+0.15} _{-0.09}	-4.67 >	-4.20 >	-4.86 >	0.07	-0.332	0.096		LSPM J0154+4905
020447.14+272903.69A	sdB	13.41	13.84	29260 ⁺¹³²⁰ ₋₆₃₀	5.62 ^{+0.14} _{-0.16}	-2.34 ^{+0.35} _{-0.64}	-3.15 >	-3.20 >	-3.25 >	0.05	0.335	0.229	d	
020447.14+272903.69B	G0IV			5500	3.08		[Fe/H] = -1.12				(0.137)	(0.233)	M	
020656.08+143857.08	sdB	13.79	13.41	30310 ⁺⁶⁶⁰ ₋₈₀	5.77 ^{+0.05} _{-0.06}	-2.61 ^{+0.15} _{-0.24}	-4.04 >	-4.47 ^{+0.33} _{-0.61}	-4.59 >	0.04	-0.464	-0.102	#7,ca	CHSS 3497
021021.86+083058.90A	sdB	13.80	13.40	34430 ⁺¹³⁸⁰ ₋₉₉₀	5.74 ^{+0.27} _{-0.17}	-1.41 ^{+0.21} _{-0.26}	-3.74 >	-4.15 >	-3.50 >	0.03	0.566	0.150	#7,r	
021021.86+083058.90B	F2IV			6580	4.19		[Fe/H] = -0.34				(0.610)	(0.145)	M	
021618.94+275900.81	sdB	13.79	13.55	25480 ⁺⁴⁵⁰ ₋₃₄₀	5.35 ^{+0.04} _{-0.05}	-2.81 ^{+0.19} _{-0.23}	-3.88 >	-3.99 ^{+0.35} _{-0.45}	-3.33 >	0.03	-0.321	-0.127	na	
022454.87+010938.81A	sdB	12.27	12.32	28000 ⁺¹⁰²⁰ ₋₅₉₀	5.45 ^{+0.18} _{-0.10}	-2.54 >	-3.24 >	-3.74 >	-3.59 >	0.05	0.684	0.173	#7,s	
022454.87+010938.81B	F4V			6430	4.00		[Fe/H] = -0.53				(0.564)	(0.165)	M	
022512.44+234822.36	sdO	13.02	13.94	46670 ⁺¹³⁵⁰ ₋₁₇₆₀	5.83 ^{+0.10} _{-0.12}	-2.18 ^{+0.24} _{-0.24}	-4.72 >	-4.03 >	-3.42 >	0.13	-0.429	-0.092	#7,ca	HS 0222+2334
023251.96+441124.96	sdB	13.74	14.30	33260 ⁺⁴²⁰ ₋₃₈₀	5.73 ^{+0.09} _{-0.10}	-1.70 ^{+0.08} _{-0.12}	-4.94 >	-4.19 >	-4.37 >	0.06	-0.555	-0.108	na,r,rv	FBS 0229+439
025023.70-040611.00	sdB	13.43	13.02	28560 ⁺⁹³⁰ ₋₃₇₀	5.67 ^{+0.11} _{-0.09}	-2.56 ^{+0.25} _{-0.35}	-3.49 >	-3.89 ^{+0.38} _{-0.73}	-3.68 >	0.17	-0.824	0.268	#7	HE 0247-0418
031738.02+144624.00	He-sdO	12.97	12.67	47520 ⁺¹⁰³⁰ ₋₈₂₀	5.96 ^{+0.15} _{-0.19}	0.90 ^{+0.17} _{-0.21}	-2.25 ^{+1.18} _{-0.20}	-2.38 ^{+0.86} _{-0.76}	-1.54 >	0.15	-0.170	-0.074	#7,C&N	PG 0314+146
031738.02+144624.00	45310 ⁺¹⁶¹⁰ ₋₁₄₁₀	5.74 ^{+0.27} _{-0.47}	0.34 ^{+0.76} _{-0.10}	-2.50 ^{+1.19} _{-0.53}	-2.55 ^{+1.18} _{-0.68}	-1.62 >	0.20	#11,C&N	PG 0314+146
032139.63+472718.83	sdB	11.91	11.70	27990 ⁺⁴⁰⁰ ₋₄₀₀	5.34 ^{+0.07} _{-0.07}	-2.52 ^{+0.17} _{-0.22}	-3.94 >	-4.30 >	-3.88 >	0.00	-0.107	-0.052	RV ^d ,s,t	TYC 3315-1807-1
040105.31-322346.01	sdB	11.03	11.20	30490 ⁺²⁵⁰ ₋₂₂₀	5.71 ^{+0.06} _{-0.04}	-1.92 ^{+0.06} _{-0.04}	-4.17 ^{+0.27} _{-0.41}	-3.93 ^{+0.21} _{-0.27}	-4.62 >	0.05	-0.594	-0.143	#7	CD-32 1567
040105.31-322346.01	27050 ⁺¹¹⁷⁰ ₋₁₀₆₀	5.35 ^{+0.25} _{-0.17}	-1.81 ^{+0.25} _{-0.27}	-3.53 >	-3.07 >	-3.10 >	0.00	#11,rv	CD-32 1567
042034.80+012041.00	He-sdO	12.51	12.52	46050 ⁺⁹¹⁰ ₋₅₁₀	5.97 ^{+0.16} _{-0.11}	0.97 ^{+0.12} _{-0.22}	-1.59 ^{+0.93} _{-0.14}	-2.21 ^{+0.83} _{-0.76}	-1.80 >	0.09	-0.435	-0.140	#7,C&N	
050018.90+091204.60	sdB	13.67	14.63	36270 ⁺⁴⁹⁰ ₋₁₁₃₀	5.75 ^{+0.15} _{-0.13}	-1.46 ^{+0.14} _{-0.15}	-3.96 >	-3.40 >	-4.06 >	0.17	-0.083	-0.238	#7,rv	HS 0457+0907
050720.16-280224.80	sdB	11.94	12.39	29840 ⁺¹⁸⁰ ₋₂₀₀	5.61 ^{+0.03} _{-0.06}	-2.44 ^{+0.11} _{-0.14}	-4.54 >	-4.70 ^{+0.41} _{-1.04}	-4.46 >	0.09	1.304	0.214	#7,ca,t	HE 0505-2806
050720.16-280224.80	25710 ⁺³⁴⁵⁰ ₋₁₄₅₀	5.28 ^{+0.40} _{-0.26}	-1.70 >	-2.87 >	-2.43 >	-2.07 >	0.00	#11,ca,c,t	HE 0505-2806
050720.16-280224.80	26070 ⁺²⁴³⁰ ₋₁₀₄₀	5.36 ^{+0.22} _{-0.31}	-2.13 ^{+0.49} _{-0.98}	-2.97 >	-3.12 >	-2.47 >	0.15	#11,ca,c,t	HE 0505-2806

^a Kawka et al. (2010)

Table 2. Atmospheric parameters of hot subdwarf stars in the *GALEX* survey. Continued.

GALEXJ	Type	N_{UV} (mag)	V (mag)	T_{eff} (K)	$\log g$ (cm s^{-2})	Abundances, [X/H] ^a or [Fe/H]				$E(B - V)$ (mag)	$V - J$ (mag)	$J - H$ (mag)	Comments	Other name
						He	C	N	O					
050735.80+034815.00	sdB	13.82	14.42	23990 ⁺⁶³⁰ ₋₆₁₀	5.42 ^{+0.08} _{-0.11}	-3.05 ^{+0.48} _{-0.78}	-3.95 >	-3.29 >	-2.87 >	0.10	-0.205	0.005	#7,rv	
055542.07+640812.60	sdO	13.07	13.33	45600 ⁺⁷⁷⁰ ₋₃₃₈₀	5.73 ^{+0.04} _{-0.39}	-2.59 ^{+0.45} _{-0.29}	-4.49 >	-3.80 >	-4.06 >	<0.22	-0.381	-0.097	f,b,na	FBS 0550+641
061325.26+342053.09	sdB	13.60	13.63	34250 ⁺³³⁰ ₋₃₉₀	5.75 ^{+0.10} _{-0.06}	-1.28 ^{+0.04} _{-0.08}	-3.92 ^{+0.40} _{-0.63}	-3.75 >	-3.90 >	0.17	-0.408	0.027	na,r	
063952.00+515658.00	sdB	12.47	11.97	30400 ⁺²⁵⁰ ₋₃₄₀	5.58 ^{+0.13} _{-0.04}	-2.66 ^{+0.20} _{-0.28}	-4.32 >	-4.36 >	-4.68 >	0.19	-0.554	-0.142	na,b,rv,r ^b ,t	
065736.93-732449.60	sdB	10.99	11.90	29940 ⁺⁹⁰⁰ ₋₁₆₀	5.45 ^{+0.07} _{-0.15}	-3.21 >	-4.46 >	-4.14 >	-4.08 >	0.08	1.070	0.252	#7,ca,t	CPD-73 420
065736.93-732449.60	28930 ⁺⁷⁹⁰ ₋₁₁₀₀	5.10 ^{+0.13} _{-0.21}	-5.28 >	-4.30 >	-3.46 >	-2.94 >	0.25	#11,c,t,rv	CPD-73 420
065736.93-732449.60	25010 ⁺²⁴⁵⁰ ₋₁₈₈₀	4.85 ^{+0.36} _{-0.26}	-2.07 >	-2.85 >	-2.70 >	-1.72 >	0.17	#11,c,t,rv	CPD-73 420
070123.11+532938.84	He-sdO	13.57	15.31	67230 ⁺²³⁸⁰ ₋₃₈₈₀	5.60 ^{+0.08} _{-0.22}	-0.25 ^{+0.54} _{-0.04}	-3.09 ^{+0.45} _{-0.76}	-2.75 >	-2.60 >	0.09	-0.322	0.000	he,C&N	
070331.53+623626.35	sdB	12.67	13.10	28750 ⁺³⁷⁰ ₋₃₄₀	5.40 ^{+0.07} _{-0.26}	-2.76 ^{+0.22} _{-0.04}	-4.07 >	-4.46 ^{+0.34} _{-1.02}	-3.91 >	0.03	-0.675	-0.067	na,s	FBS 0658+627
071029.43+233322.24A	sdO	13.87	14.01	55420 ⁺²⁴³⁰⁰ ₋₃₈₄₀	5.21 ^{+0.43} _{-0.14}	-1.56 ^{+0.33} _{-0.32}	-3.66 >	-3.55 >	-3.16 >	0.03	-0.154	0.058	na,d	
071029.43+233322.24B	F6V	6310	4.26	[Fe/H] = -0.25					(0.075)	(0.101)	M	
071053.44+562446.77	sdB	13.50	14.98	39970 ⁺⁹⁸⁰ ₋₉₄₀	5.91 ^{+0.08} _{-0.14}	-3.16 ^{+0.48} _{-1.03}	-4.69 >	-4.00 >	-4.17 >	0.02	-0.214	-0.165		
071618.19+750241.99	He-sdO	13.74	15.04	43200 ⁺⁷¹⁰ ₋₈₈₀	5.55 ^{+0.53} _{-0.06}	0.74 ^{+0.75} _{-0.13}	-2.08 ^{+0.59} _{-0.86}	-2.09 >	-1.47 >	<0.25	-0.476	0.115	f,rv	FBS 0709+751
073527.00+613244.38	He-sdO	13.60	14.18	48400 ⁺¹⁴¹⁰ ₋₁₀₈₀	6.05 ^{+0.17} _{-0.21}	0.04 ^{+0.56} _{-0.09}	-2.73 ^{+0.85} _{-0.27}	-2.76 ^{+0.96} _{-0.33}	-2.12 >	0.06	-0.421	-0.197	C&N	FBS 0730+617
073804.54+262444.18	sdB	13.77	14.42	29740 ⁺⁴⁰⁰ ₋₂₅₀	5.48 ^{+0.06} _{-0.06}	-3.40 ^{+0.41} _{-0.87}	-3.99 >	-4.07 >	-4.05 >	0.00	-0.814	-0.054	s	
074148.99+552451.19	sdB	13.74	14.71	33470 ⁺⁴³⁰ ₋₃₉₀	5.76 ^{+0.04} _{-0.12}	-1.93 ^{+0.11} _{-0.17}	-6.01 >	-4.04 >	-3.78 >	0.19	0.071	0.407	na,r	
074435.08+302108.96	sdB	13.84	14.64	27910 ⁺⁴⁷⁰ ₋₂₈₀	5.42 ^{+0.08} _{-0.05}	-2.75 ^{+0.13} _{-0.25}	-4.04 >	-4.07 >	-4.19 >	0.01	-0.654	-0.110	s	
074617.10+061006.00	sdB	13.08	12.85	26530 ⁺⁵⁷⁰ ₋₅₄₀	5.71 ^{+0.06} _{-0.07}	-3.24 >	-4.40 >	-3.74 >	-3.58 >	0.17	0.295	0.353	#7,rv	
074722.24+622547.10	sdB	11.67	11.90	22550 ⁺⁴⁰⁰ ₋₂₂₀	4.99 ^{+0.05} _{-0.06}	-0.95 ^{+0.04} _{-0.04}	-3.12 ^{+0.15} _{-0.29}	-3.21 ^{+0.28} _{-0.47}	-2.88 >	<0.19	-0.640	-0.122		FBS 0742+625
074855.82+304249.36	sdB	13.11	14.16	30760 ⁺⁸³⁰ ₋₁₇₀	5.71 ^{+0.17} _{-0.04}	-1.85 ^{+0.05} _{-0.13}	-4.01 ^{+0.37} _{-0.51}	-4.07 ^{+0.35} _{-0.30}	-3.89 >	0.00	-0.403	-0.036		Ton 287 ?
075147.00+092526.00	sdB	???	14.12	30620 ⁺⁴⁹⁰ ₋₄₆₀	5.74 ^{+0.11} _{-0.12}	-2.49 ^{+0.27} _{-0.30}	-4.04 >	-3.74 >	-3.69 >	0.10	-0.518	-0.227	#7	
075234.20+161604.00	He-sdO	13.87	14.23	49280 ⁺⁵³²⁰ ₋₅₉₀	6.08 ^{+0.19} _{-0.36}	0.47 ^{+0.60} _{-0.13}	-2.73 ^{+1.19} _{-0.32}	-1.84 >	-2.08 >	0.08	-1.009	-0.136	#7,C&N	
075603.77+222628.82	sdO	13.12	14.50	51160 ⁺⁵⁸⁰ ₋₅₂₇₀	5.73 ^{+0.03} _{-0.26}	-2.43 ^{+0.26} _{-0.18}	-4.43 >	-4.06 >	-3.72 >	0.01	-0.335	-0.093	na	Ton 835 ?
075807.55-043203.87	He-sdO	11.81	12.20	41360 ⁺⁵³⁰ ₋₂₂₀	5.85 ^{+0.26} _{-0.06}	0.54 ^{+0.49} _{-0.04}	-2.27 >	-2.44 ^{+0.22} _{-2.02}	-2.32 >	0.01	-1.581	-0.148	#7	
080510.90-105834.00	sdB	12.35	12.21	22320 ⁺³³⁰ ₋₂₈₀	5.68 ^{+0.03} _{-0.06}	-3.44 >	-3.96 >	-3.68 >	-3.28 >	0.04	-0.437	-0.117	#7,rv	
080510.90-105834.00	22240 ⁺²⁹⁰ ₋₂₃₀	5.71 ^{+0.03} _{-0.04}	-3.21 >	-4.16 >	-3.93 >	-3.12 >	0.02	#7,rv	
080510.90-105834.00	22020 ⁺⁴⁶⁰ ₋₃₄₀	5.65 ^{+0.06} _{-0.06}	-3.25 >	-3.80 >	-3.51 >	-2.74 >	0.08	#7	
080656.70+152718.00	sdB	13.74	14.69	29410 ⁺⁵⁴⁰ ₋₆₁₀	5.44 ^{+0.11} _{-0.12}	-2.67 >	-3.70 >	-3.74 >	-3.86 >	0.05	-0.743	0.377	#7,s ^c ,t	
080929.50+054843.82	BHB	13.48	13.84	21290 ⁺²³⁰ ₋₂₂₀	4.89 ^{+0.03} _{-0.05}	-1.25 ^{+0.05} _{-0.08}	-3.15 ^{+0.18} _{-0.15}	-3.29 ^{+0.25} _{-0.37}	-3.04 >	0.01	-0.186	-0.104		
081203.80+070352.00	sdB	13.74	14.78	35590 ⁺⁵⁶⁰ ₋₆₂₀	5.75 ^{+0.09} _{-0.10}	-1.72 ^{+0.11} _{-0.16}	-4.23 >	-3.62 >	-4.12 >	0.09	-0.211	0.534	#7,r,rv	
081233.60+160121.00	sdB	12.79	13.57	31580 ⁺⁴⁴⁰ ₋₄₉₀	5.56 ^{+0.10} _{-0.13}	-2.90 >	-4.10 >	-3.78 ^{+0.46} _{-0.88}	-3.64 >	0.19	-0.731	-0.025	#7	
082556.78+130754.73	sdB	13.62	14.59	38070 ⁺⁷¹⁰ ₋₇₃₀	5.91 ^{+0.14} _{-0.10}	-1.87 ^{+0.17} _{-0.22}	-4.52 >	-3.59 >	-3.24 >	<0.26	0.545	0.424	na,b	
082734.90+175358.00	sdB	13.72	14.62	29550 ⁺⁹⁵⁰ ₋₈₀₀	5.55 ^{+0.09} _{-0.08}	-1.28 ^{+0.10} _{-0.09}	-4.43 ^{+0.62} _{-0.82}	-3.79 ^{+0.39} _{-0.61}	-3.52 ^{+0.29} _{-1.08}	0.10	-0.433	-0.112	#7,s,rv	SDSSCGB 7585.3
082832.80+145205.00	He-sdB	11.65	11.78	37060 ⁺⁶⁰⁰ ₋₆₁₀	5.92 ^{+0.09} _{-0.10}	-0.62 ^{+0.05} _{-0.08}	-4.00 >	-3.47 ^{+0.25} _{-0.38}	-3.96 >	0.14	-0.645	-0.161	#7	TD1 32707
083412.30+071211.00	sdB	13.73	14.86	29870 ⁺⁴⁸⁰ ₋₅₆₀	5.56 ^{+0.12} _{-0.10}	-2.62 >	-3.82 >	-4.13 >	-4.03 >	0.04	-0.464	-0.111	#7,rv	

^b Vučković et al. (2012)

^c Baran et al. (2011)

Table 2. Atmospheric parameters of hot subdwarf stars in the *GALEX* survey. Continued.

GALEXJ	Type	N_{UV} (mag)	V (mag)	T_{eff} (K)	$\log g$ ($cm\ s^{-2}$)	Abundances, [X/H]• or [Fe/H]				$E(B - V)$ (mag)	$V - J$ (mag)	$J - H$ (mag)	Comments	Other name
						He	C	N	O					
084024.05+113911.53	B	13.89	13.19	13270 ⁺⁴⁰ ₋₉₀	4.14 ^{+0.02} _{-0.02}	-1.27 ^{+0.04} _{-0.11}	-3.04 >	-2.81 >	-2.98 ^{+0.32} _{-1.40}	0.00	0.000	-0.041	na	NVSS J084025+113959
084143.80+130431.00	He-sdO	12.91	13.66	47660 ⁺³⁷¹⁰ ₋₇₇₀	5.68 ^{+0.29} _{-0.24}	0.73 ^{+0.34} _{-0.28}	-2.52 ^{+1.39} _{-0.45}	-1.55 >	-1.52 >	0.12	-0.643	-0.154	#7,C&N	PG 0838+133
084535.54+194150.18	BHB	13.33	13.34	21570 ⁺²¹⁰ ₋₁₇₀	4.87 ^{+0.03} _{-0.04}	-1.73 ^{+0.03} _{-0.14}	-4.01 >	-3.99 ^{+0.36} _{-0.69}	-3.56 >	0.04	-0.328	-0.085		LB 400 ?
085137.75+244151.69	sdO	12.68	14.35	70000 ⁺³¹⁹⁰ ₋₅₉₄₀	5.56 ^{+0.07} _{-0.10}	-1.79 ^{+0.17} _{-0.14}	-3.09 >	-3.61 >	-3.96 ^{+0.69} _{-0.89}	0.04	0.035	0.120	na	PG 0848+249
085649.30+170115.00	sdB	12.22	13.17	29270 ⁺³⁸⁰ ₋₄₅₀	5.39 ^{+0.20} _{-0.03}	-2.81 >	-4.44 >	-4.00 ^{+0.28} _{-1.10}	-3.74 >	0.14	-0.256	-0.079	#7,s	
090540.90+121228.00	sdB	13.73	14.67	28050 ⁺⁸⁴⁰ ₋₆₄₀	5.50 ^{+0.11} _{-0.15}	-2.79 ^{+0.37} _{-0.76}	-3.87 >	-3.52 >	-3.66 >	0.07	-0.578	0.090	#7,s	PG 0902+124
092308.30+024208.00	sdB	13.39	14.48	29100 ⁺⁴³⁰ ₋₄₄₀	5.41 ^{+0.09} _{-0.07}	-2.87 >	-4.59 >	-4.18 ^{+0.51} _{-0.90}	-3.74 >	0.21	-0.583	-0.180	#7,ca,s,rv	PG 0920+029
092440.11+305013.16	He-sdO	13.25	14.73	40830 ⁺¹⁶⁰ ₋₁₆₀	5.84 ^{+0.15} _{-0.04}	0.59 ^{+0.54} _{-0.01}	-2.89 >	-2.29 ^{+0.18} _{-0.46}	-2.43 >	0.01	-0.572	-0.328		PG 0921+311
092856.10+061634.00	sdB	13.44	14.29	26060 ⁺⁶⁸⁰ ₋₄₅₀	5.45 ^{+0.07} _{-0.08}	-2.79 ^{+0.23} _{-0.46}	-4.58 >	-3.60 ^{+0.42} _{-0.59}	-3.27 >	0.17	-0.334	-0.121	#7,ca,s	PG 0926+065
093448.20-251248.00	sdB	12.05	13.03	34440 ⁺⁹⁹⁰ ₋₂₁₆₀	5.17 ^{+0.21} _{-0.29}	-1.85 >	-3.84 >	-3.24 >	-3.23 >	0.03	-0.682	-0.051	#11,he,t	
095256.60-371940.00	He-sdO	12.00	12.69	44230 ⁺¹¹⁴⁰ ₋₁₁₂₀	5.68 ^{+0.23} _{-0.36}	0.53 ^{+1.50} _{-0.10}	-1.83 >	-1.82 >	-1.40 >	0.05	-1.168	-0.147	#11	
100752.00-292435.00	sdO	11.99	12.87	41880 ⁺⁹⁷³⁰ ₋₄₁₂₀	5.57 ^{+0.67} _{-0.71}	-3.73 >	-5.32 >	-2.65 >	-4.36 >	0.00	-0.148	0.131	#11,f	
101756.84+551632.41A	sdB	12.15	12.30	24260 ⁺¹⁴⁵⁰ ₋₁₀₄₀	5.05 ^{+0.48} _{-0.12}	-2.00 >	-3.44 >	-3.74 >	-2.43 >	0.00	1.078	0.126		
101756.84+551632.41B	F5V			6610	4.09			[Fe/H] = -0.54			(0.507)	(0.132)	M	
102358.61+691145.65	He-sdO	13.61	14.69	46750 ⁺⁹⁴⁰ ₋₁₁₁₀	5.63 ^{+0.43} _{-0.06}	0.45 ^{+0.56} _{-0.03}	-2.65 ^{+0.74} _{-0.44}	-2.39 >	-2.22 >	<0.05	-0.572	-0.005	f,rv	FBS 1020+694
102728.92+745947.26	sdB	13.89	13.87	35370 ⁺⁸⁰⁰ ₋₈₆₀	5.65 ^{+0.12} _{-0.18}	-1.73 ^{+0.16} _{-0.28}	-3.32 >	-4.31 >	-3.41 >	<0.42	-0.071	0.268	f,na	FBS 1023+753
104122.80+504420.00	He-sdO	13.69	15.31	51150 ⁺¹⁰⁸⁰ ₋₁₀₀₀	6.41 ^{+0.04} _{-0.66}	0.11 ^{+0.35} _{-0.06}	-2.77 ^{+0.86} _{-0.11}	-2.87 ^{+0.51} _{-0.65}	-2.27 >	0.00	-0.343	-0.224	C&N	PG 1038+510
104130.40+184210.00	sdB	12.27	13.24	34890 ⁺⁴⁴⁰ ₋₆₈₀	5.80 ^{+0.08} _{-0.10}	-1.68 ^{+0.09} _{-0.13}	-3.98 >	-3.37 ^{+0.24} _{-0.73}	-4.05 >	0.17	-0.430	-0.099	#7,ca,r	
104148.90-073031.00	sdB	12.49	12.14	27440 ⁺⁶²⁰ ₋₄₅₀	5.63 ^{+0.09} _{-0.06}	-2.44 ^{+0.16} _{-0.23}	-3.76 >	-3.87 ^{+0.40} _{-0.57}	-3.75 >	0.09	-0.062	-0.093	#7	
110055.90+105542.00	sdB	12.93	14.20	31970 ⁺³⁶⁰ ₋₄₁₀	5.87 ^{+0.08} _{-0.10}	-2.00 ^{+0.15} _{-0.14}	-4.40 >	-3.53 >	-3.93 >	0.15	-0.726	-0.014	#7,ca,r	
110541.40-140423.00A	sdB	11.82	11.54	30120 ⁺⁵¹⁰⁰ ₋₃₇₉₀	5.90 ^{+0.68} _{-0.82}	-1.04 ^{+0.89} _{-1.07}	-5.59 >	-1.46 >	-1.24 >	0.00	0.743	0.161	#11,f	EC 11031-1348
110541.40-140423.00B	F6V			6430	4.03			[Fe/H] = 0.00			(0.692)	(0.179)	M	
111422.00-242130.00	sdB	13.16	12.68	23430 ⁺⁴⁸⁰ ₋₄₅₀	5.29 ^{+0.08} _{-0.07}	-2.46 ^{+0.19} _{-0.31}	-4.01 ^{+0.62} _{-1.28}	-3.47 >	-3.29 >	0.14	0.452	-0.116	#7,ca	EC 11119-2405
113128.89+283739.18	B	13.70	13.71	19000 ⁺²⁵⁰ ₋₂₃₀	4.43 ^{+0.04} _{-0.05}	-2.30 ^{+0.13} _{-0.09}	-4.40 >	-3.66 >	-2.89 >	0.00	-0.320	-0.128	na	CHSS 1935
113633.58+750652.07	sdB	12.05	12.99	36030 ⁺⁵²⁰ ₋₅₉₀	5.88 ^{+0.06} _{-0.12}	-2.22 ^{+0.18} _{-0.16}	-4.91 >	-4.17 >	-4.40 >	0.00	-0.795	-0.098	he,na,ca	FBS 1133+754
120624.37+570935.70	sdB	13.71	14.87	33620 ⁺²⁸⁰ ₋₃₉₀	5.90 ^{+0.04} _{-0.13}	-1.88 ^{+0.08} _{-0.12}	-4.89 >	-4.30 >	-4.55 >	0.09	-0.706	-0.115	he,r	PG 1203+574
123716.47+383541.22	B	13.84	13.53	17570 ⁺¹¹⁰ ₋₂₅₀	3.96 ^{+0.02} _{-0.04}	-2.04 ^{+0.11} _{-0.18}	-4.79 >	-3.68 >	-3.53 >	0.02	-0.383	-0.072	rv	HZ 30, SSI1 182
125941.60+164827.00	sdB	13.85	14.37	36830 ⁺⁷⁴⁰ ₋₆₅₀	5.95 ^{+0.09} _{-0.11}	-1.66 ^{+0.10} _{-0.13}	-3.88 >	-3.75 >	-3.99 >	0.13	-0.467	-0.139	#7	PG 1257+171
131512.40+024531.00	sdO	13.61	15.10	41210 ⁺¹⁴²⁰ ₋₁₄₇₀	5.46 ^{+0.12} _{-0.13}	-2.79 ^{+0.40} _{-0.67}	-4.49 >	-6.42 >	-3.60 >	0.25	-0.055	-0.071	#7,ca	
135450.06+055937.32	B	13.87	13.54	14730 ⁺⁸⁰ ₋₂₀₀	4.18 ^{+0.03} _{-0.07}	-1.09 ^{+0.15} _{-0.06}	-2.96 >	-2.55 >	-2.60 >	0.00	-0.140	-0.059		
135629.20-493403.00	sdB	11.72	12.30	33070 ⁺²³⁰ ₋₆₆₀	5.74 ^{+0.07} _{-0.16}	-2.75 ^{+0.25} _{-0.43}	-4.17 >	-4.00 >	-4.37 >	0.10	0.317	0.278	#7,ca,r	CD-48 8608
135824.60+065137.00	sdB	13.68	14.50	27680 ⁺⁵⁷⁰ ₋₄₁₀	5.36 ^{+0.06} _{-0.09}	-2.95 ^{+0.26} _{-0.64}	-4.39 >	-4.30 ^{+0.39} _{-0.76}	-4.03 >	0.00	-0.474	-0.017	ca,s	PG 1355+071
140209.12+383713.12	BHB	12.49	12.47	19970 ⁺¹⁰⁰ ₋₃₉₀	4.81 ^{+0.03} _{-0.08}	-0.72 ^{+0.09} _{-0.04}	-2.99 ^{+0.21} _{-0.14}	-3.10 ^{+0.28} _{-0.43}	-2.49 >	0.00	-0.123	-0.163		PG 1400+389
140747.63+310318.06	B	13.81	14.20	24900 ⁺⁵⁰ ₋₃₀₅₀	4.25 ^{+0.03} _{-0.06}	-1.18 ^{+0.08} _{-0.09}	-4.21 >	-4.18 >	-3.67 >	0.12	-0.140	0.134	ca,rv	BPS BS 16082-0122
140956.88+805520.23	sdB	12.94	13.87	25380 ⁺³¹⁰⁰ ₋₁₉₀	5.39 ^{+0.10} _{-0.17}	-2.76 ^{+0.28} _{-0.58}	-3.38 >	-3.84 >	-2.58 >	<0.20	-0.401	-0.054	f	FBS 1411+812
141055.80+093256.00	sdB	12.69	14.10	36580 ⁺⁷¹⁰ ₋₆₂₀	5.77 ^{+0.11} _{-0.10}	-1.78 ^{+0.12} _{-0.18}	-4.23 >	-3.57 >	-3.90 >	0.18	-0.594	-0.125	#7	PG 1408+098

Table 2. Atmospheric parameters of hot subdwarf stars in the GALEX survey. Continued.

GALEXJ	Type	N_{UV} (mag)	V (mag)	T_{eff} (K)	$\log g$ (cm s^{-2})	Abundances, [X/H], or [Fe/H]				$E(B-V)$ (mag)	$V-J$ (mag)	$J-H$ (mag)	Comments	Other name
						He	C	N	O					
141115.90–305307.00	sdB	11.63	11.90	30150 ⁺²⁹⁰ ₋₃₁₀	5.72 ^{+0.04} _{-0.07}	-1.58 ^{+0.03} _{-0.05}	-4.18 >	-4.40 ^{+0.29} _{-0.67}	-4.52 >	0.04	-0.986	-0.046	#7,ca,rv	CD-30 11223
141115.90–305307.00	25080 ⁺¹²⁶⁰ ₋₇₃₀	5.22 ^{+0.19} _{-0.11}	-1.39 ^{+0.10} _{-0.14}	-3.59 >	-3.16 >	-2.76 >	0.02	#11,ca,rv	CD-30 11223
141133.45+703736.95A	sdB	12.71	13.17	21170 ⁺¹⁵⁰⁰ ₋₁₁₁₀	5.55 ^{+0.31} _{-0.23}	-2.36 >	-3.17 >	-3.02 >	-1.53 >	0.00	1.057	0.109		
141133.45+703736.95B	F0.5V			7160	4.15		[Fe/H] = 0.25				(0.333)	(0.069)	M	
142747.28–270108.00	sdB	11.33	11.48	31880 ⁺³⁶⁰ ₋₂₉₀	5.70 ^{+0.05} _{-0.08}	-1.71 ^{+0.05} _{-0.11}	-3.87 >	-4.16 ^{+0.33} _{-0.73}	-4.48 >	0.08	-1.049	-0.140	#7,r	EC 14248–2647
143519.80+001350.00	sdB	12.25	12.36	23090 ⁺⁷⁸⁰ ₋₂₅₀	5.28 ^{+0.08} _{-0.08}	-2.39 ^{+0.18} _{-0.20}	-4.66 ^{+0.72} _{-0.77}	-3.26 ^{+0.36} _{-1.02}	-2.84 >	0.20	-0.884	-0.072	#7,ca	PG 1432+004
145928.50+190350.00	sdB	13.33	14.17	37350 ⁺⁴⁶⁰ ₋₁₀₉₀	5.92 ^{+0.10} _{-0.15}	-1.41 ^{+0.08} _{-0.17}	-3.70 >	-3.27 ^{+0.28} _{-0.88}	-3.76 >	0.25	-0.751	-0.077	#7	PG 1457+193
150109.07+412137.20	B	13.88	13.55	15530 ⁺⁸⁰ ₋₂₁₀	4.18 ^{+0.02} _{-0.05}	-2.53 >	-4.09 >	-2.89 >	-3.34 >	0.03	-0.139	-0.109	rv	PG 1459+416
150346.81+422125.12	sdB	13.68	14.80	29170 ⁺³⁸⁰ ₋₂₅₀	5.52 ^{+0.12} _{-0.04}	-2.88 ^{+0.17} _{-0.30}	-3.94 >	-4.50 ^{+0.34} _{-0.96}	-4.52 >	0.00	-0.480	0.085	he,s	PG 1501+426
151325.75+645407.12A	sdB	13.60	13.95	34310 ⁺¹⁶⁸⁰ ₋₁₅₆₀	6.17 ^{+0.30} _{-0.36}	-1.81 ^{+0.74} _{-0.30}	-2.98 >	-3.12 >	-2.82 >	0.00	0.585	0.186		
151325.75+645407.12B	G0V			5890	4.37		[Fe/H] = -1.79				(0.681)	(0.307)	M	
152513.08+605321.53A	sdB	12.13	12.88	34380 ⁺¹⁰⁰⁰ ₋₆₉₀	5.77 ^{+0.17} _{-0.15}	-1.56 ^{+0.18} _{-0.18}	-3.55 >	-3.46 >	-3.55 >	0.00	0.597	0.192	r	PG 1524+611
152513.08+605321.53B	G0V			5820	3.92		[Fe/H] = -0.74				(0.486)	(0.195)	M	
154509.52+595505.20	sdB	13.62	14.56	29060 ⁺²⁸⁰ ₋₂₅₀	5.43 ^{+0.05} _{-0.05}	-3.44 ^{+0.26} _{-0.60}	-4.18 >	-4.49 ^{+0.35} _{-0.90}	-4.14 >	0.00	-0.521	-0.125	s	PG 1544+601
160131.30+044027.00	He-sdB	13.48	14.56	40330 ⁺⁸⁶⁰ ₋₇₇₀	6.16 ^{+0.18} _{-0.10}	-0.53 ^{+0.04} _{-0.21}	-2.75 ^{+0.15} _{-0.38}	-2.73 ^{+0.19} _{-0.41}	-2.92 >	0.24	-0.398	-0.127	#7	PG 1559+048
160209.18+072509.84A	sdO	13.63	14.63	67570 ⁺¹⁵⁵⁴⁰ ₋₃₉₅₀	5.74 ^{+0.24} _{-0.13}	-1.56 ^{+0.29} _{-0.35}	-2.95 >	-2.66 >	-3.09 >	0.04	0.492	0.296	#7,d	PG 1559+076
160209.18+072509.84B	G0V			5980	4.05		[Fe/H] = 0.07				(0.300)	(0.172)	M	
161327.66+085355.54	sdB	13.88	14.44	31840 ⁺³¹⁰ ₋₃₂₀	5.87 ^{+0.08} _{-0.09}	-2.27 ^{+0.15} _{-0.18}	-4.28 >	-3.97 >	-4.40 >	0.00	-0.857	0.003	#7,ca,r,rv	PG 1611+090
161902.78+483144.11A	sdB	13.35	13.36	34670 ⁺²³⁷⁰ ₋₁₆₁₀	5.73 ^{+0.56} _{-0.24}	-6.96 >	-5.86 >	-5.98 >	-7.13 >	0.00	0.705	0.124	r	BPS BS 16029-0090
161902.78+483144.11B	F0V			6700	4.44		[Fe/H] = -0.01				(0.494)	(0.007)	M	
162431.88+405913.03	sdB	13.64	14.32	27590 ⁺⁴³⁰ ₋₂₆₀	5.29 ^{+0.06} _{-0.05}	-2.53 ^{+0.14} _{-0.30}	-3.97 ^{+0.25} _{-0.60}	-4.47 ^{+0.37} _{-1.11}	-3.64 >	0.03	-0.323	0.052		KUV 16229+4106
162716.50+402728.48	sdB	12.29	12.60	23560 ⁺⁴¹⁰ ₋₂₅₀	5.44 ^{+0.03} _{-0.07}	-3.08 ^{+0.20} _{-0.29}	-4.35 >	-3.56 >	-3.75 >	0.00	-0.467	-0.157	rv	FBS 1625+407
162822.57+272919.71	sdB	13.11	13.72	25380 ⁺³⁵²⁰ ₋₆₀	5.31 ^{+0.05} _{-0.12}	-2.45 ^{+0.12} _{-0.30}	-3.66 >	-3.73 ^{+0.31} _{-0.45}	-2.98 >	0.00	-0.455	-0.137	rv	
163201.40+075940.00	sdB	13.41	12.97	38110 ⁺⁵⁷⁰ ₋₆₈₀	5.38 ^{+0.06} _{-0.09}	-2.71 ^{+0.27} _{-0.29}	-5.03 >	-4.43 >	-4.21 >	0.03	0.134	0.225	#7	PG 1629+081
163201.40+075940.00	35780 ⁺¹⁴²⁰ ₋₁₅₈₀	5.14 ^{+0.12} _{-0.40}	-2.15 >	-4.20 >	-3.72 >	-3.89 >	0.10	#11,he	PG 1629+081
163215.73+851359.16	sdB	12.58	12.45	33590 ⁺²¹⁰ ₋₈₁₀	5.47 ^{+0.15} _{-0.08}	-3.38 >	-4.53 >	-4.31 >	-4.52 >	0.06	-0.401	-0.143	na	FBS 1642+853
163705.28+411541.02	sdB	12.90	14.15	26850 ⁺⁴²⁰ ₋₃₁₀	5.42 ^{+0.06} _{-0.05}	-2.75 ^{+0.16} _{-0.24}	-4.30 >	-4.30 ^{+0.28} _{-0.98}	-4.01 >	0.00	-0.420	-0.124	s,rv	FBS 1635+413
164614.55+062300.71	sdB	13.72	14.84	33170 ⁺²⁴⁰ ₋₃₉₀	5.84 ^{+0.08} _{-0.07}	-2.43 ^{+0.23} _{-0.12}	-3.70 >	-4.08 >	-4.87 >	0.01	-0.617	0.100	#7,ca,r,rv	PG 1643+063
165054.44+353341.65	sdB	13.85	15.49	33020 ⁺⁶¹⁰ ₋₂₈₀	5.82 ^{+0.09} _{-0.11}	-1.32 ^{+0.03} _{-0.08}	-3.81 >	-4.17 ^{+0.31} _{-0.41}	-4.15 >	0.00	-0.241	-0.057	r	PG 1649+356
165157.16+262551.56	sdO	13.56	14.26	67700 ⁺²³⁷⁰ ₋₇₀₈₀	5.80 ^{+0.06} _{-0.30}	-1.83 ^{+0.31} _{-0.12}	-3.28 >	-3.74 >	-3.56 >	0.00	-0.608	-0.252	na	
170211.83+483024.66	sdB	13.22	14.30	26010 ⁺¹¹¹⁰ ₋₁₄₀	5.18 ^{+0.09} _{-0.03}	-2.58 ^{+0.09} _{-0.33}	-4.00 >	-3.90 >	-3.67 >	0.00	-0.530	-0.155		PG 1700+486
171708.53+675712.24	WD	13.76	13.73	14910 ⁺¹⁰⁰ ₋₁₅₀	5.67 ^{+0.04} _{-0.03}	-2.26 >	-3.18 >	-2.81 >	-2.88 >	0.00	0.121	-0.083	RV ^e ,ca	
172748.43+164456.52	sdB	12.98	13.35	28210 ⁺⁵⁵⁰ ₋₄₂₀	5.27 ^{+0.09} _{-0.08}	-2.87 ^{+0.30} _{-0.61}	-3.67 >	-4.11 >	-3.94 >	0.14	0.024	0.265	#7,ca	
172704.66+294229.22	sdB	13.78	15.03	37610 ⁺⁹⁹⁰ ₋₁₀₁₀	5.52 ^{+0.10} _{-0.13}	-2.66 >	-4.29 >	-3.75 >	-3.69 >	<0.07	-0.650	-0.028	f	LB 334 ?

^e Vennes et al. (2011b)

Table 2. Atmospheric parameters of hot subdwarf stars in the *GALEX* survey. Continued.

GALEXJ	Type	N_{UV} (mag)	V (mag)	T_{eff} (K)	$\log g$ (cm s^{-2})	Abundances, [X/H], or [Fe/H]				$E(B - V)$ (mag)	$V - J$ (mag)	$J - H$ (mag)	Comments	Other name
						He	C	N	O					
173153.70+064706.00	sdB	13.52	13.74	27780 ⁺¹⁰³⁰ ₋₄₇₀	5.35 ^{+0.18} _{-0.07}	-2.53 >	-3.84 >	-3.81 >	-3.60 >	0.16	-0.710	-0.062	#7,he,s	
173630.26+073601.04	sdB	13.68	13.91	28100 ⁺³⁹⁰ ₋₃₆₀	5.43 ^{+0.07} _{-0.06}	-3.19 ^{+0.34} _{-0.78}	-3.82 >	-4.33 ^{+0.38} _{-0.57}	-4.33 >	0.08	-0.125	-0.053	#7,ca,s	
173651.20+280635.00A	sdB	11.53	11.44	36160 ⁺⁶⁵⁰⁰ ₋₄₂₂₀	5.24 ^{+0.84} _{-0.84}	-1.09 ^{+0.69} _{-1.34}	-2.21 >	-1.65 >	-1.63 >	0.11	0.591	0.214	#11	TYC 2084-448-1
173651.20+280635.00B	F7V			6240	4.00			[Fe/H] = 0.17			(0.640)	(0.176)	M	
173812.47+263408.58	sdB	13.86	14.88	22880 ⁺⁸⁰⁰ ₋₂₃₀	5.56 ^{+0.05} _{-0.10}	-3.26 >	-4.13 >	-3.58 >	-3.20 >	0.00	-0.138	-0.237	na	
175137.44+371952.37	He-sdB	13.25	14.64	34630 ⁺⁶⁰⁰ ₋₅₈₀	5.89 ^{+0.12} _{-0.10}	-0.28 ^{+0.04} _{-0.06}	-2.92 ^{+0.14} _{-0.55}	-3.40 ^{+0.32} _{-0.44}	-3.63 >	0.00	-0.609	-0.252	r,rv	FBS 1749+373
175324.62+691058.08	He-sdO	13.84	15.46	43710 ⁺²⁸⁰ ₋₁₁₆₀	5.81 ^{+0.41} _{-0.06}	0.05 ^{+2.02} _{-0.02}	-2.33 >	-2.86 ^{+0.36} _{-0.96}	-2.67 >	0.07	-0.127	-0.513	rv	FBS 1753+692
175340.57-500741.80A	sdB	13.21	12.88	32430 ⁺⁸⁸⁰ ₋₅₇₀	5.95 ^{+0.18} _{-0.18}	-2.25 ^{+0.31} _{-1.04}	-3.58 >	-4.70 >	-3.98 >	0.08	0.766	0.253	#7	
175340.57-500741.80B	F7V			6180	4.04			[Fe/H] = -0.32			(0.722)	(0.202)	M	
175548.50+501210.77	He-sdO	13.31	12.94	40370 ⁺⁹⁴⁰ ₋₂₁₀	5.96 ^{+0.05} _{-0.15}	1.30 ^{+0.27} _{-0.10}	-2.06 >	-1.46 ^{+0.34} _{-0.19}	-2.17 ^{+0.57} _{-0.65}	0.00	-0.626	-0.161	rv	
181032.00+053909.00	sdB	13.13	13.81	31890 ⁺⁴⁶⁰ ₋₄₆₀	5.81 ^{+0.11} _{-0.10}	-2.46 >	-3.50 >	-4.16 ^{+0.52} _{-1.76}	-4.11 >	0.17	-0.412	-0.049	#7,ca,r	
182530.60+084749.34	sdO	13.46	14.28	48970 ⁺⁸⁰⁰ ₋₃₈₅₀	5.89 ^{+0.08} _{-0.11}	-2.52 ^{+0.29} _{-0.29}	-4.68 >	-3.74 >	-3.25 >	0.08	-0.329	-0.051	#7,ca,rv	
183129.61+085107.70	sdO	13.90	14.59	62840 ⁺⁴³¹⁰ ₋₃₃₁₀	6.27 ^{+0.19} _{-0.08}	-2.46 ^{+0.26} _{-0.29}	-3.97 >	-3.88 >	-3.47 >	0.12	0.435	0.330	#7,ca,t	
184559.80-413827.00	He-sdB	13.89	14.63	35930 ⁺⁸⁴⁰ ₋₄₇₇₀	5.23 ^{+0.27} _{-0.23}	2.10 ^{+1.10} _{-0.38}	-0.82 >	-0.12 >	-0.66 >	0.12	-0.422	-0.035	#11,t	
190211.74-513005.61	He-sdO	11.10	11.53	72300 ⁺⁵³⁸⁰ ₋₃₂₆₀	5.49 ^{+0.11} _{-0.11}	0.02 ^{+2.10} _{-0.03}	-2.58 >	-2.43 ^{+0.37} _{-0.25}	-2.91 >	0.07	-0.573	0.040	#7,t	CD-51 11879, LSE 263
190302.50-352829.00	sdB	13.36	14.34	32100 ⁺¹⁷⁶⁰ ₋₁₂₆₀	5.26 ^{+0.31} _{-0.30}	-1.96 >	-3.20 >	-3.49 >	-3.30 >	0.01	-0.494	-0.124	#11,rv	BPS CS 22936-0293
191109.30-140654.00	He-sdO	11.77	11.77	55970 ⁺⁴⁵⁴⁰ ₋₁₇₈₀	5.69 ^{+0.71} _{-0.09}	0.25 ^{+0.85} _{-0.11}	-3.37 ^{+0.70} _{-0.60}	-2.69 >	-1.82 >	0.15	-0.544	-0.082	#7,C&N,rv	
191109.30-140654.00	51300 ⁺⁴⁵⁷⁰ ₋₂₇₆₀	5.50 ^{+2.13} _{-0.00}	0.01 ^{+2.13} _{-0.09}	-2.32 >	-2.20 >	-1.76 >	0.15	#11,C&N,rv	
191106.82+871604.35	sdB	12.86	12.84	31610 ⁺³⁹⁰ ₋₃₅₀	5.81 ^{+0.13} _{-0.07}	-1.83 ^{+0.09} _{-0.09}	-4.06 >	-3.76 >	-4.25 >	0.00	-0.384	-0.141	r	FBS 1930+872
200631.53+014307.25	sdB	13.74	14.45	29600 ⁺⁴³⁰ ₋₁₉₀	5.62 ^{+0.06} _{-0.06}	-2.82 ^{+0.21} _{-0.33}	-3.67 ^{+0.09} _{-0.46}	-4.19 ^{+0.27} _{-0.69}	-4.55 >	0.06	-0.327	0.034	#7,ca	
200951.66+031032.81	sdB	12.63	12.63	27160 ⁺³⁵⁰ ₋₂₅₀	5.46 ^{+0.04} _{-0.05}	-2.96 ^{+0.18} _{-0.26}	-4.32 >	-4.42 ^{+0.36} _{-0.40}	-4.50 >	0.04	-0.105	0.274	#7,ca,s	
200918.25+095143.67	sdB	13.86	14.58	27000 ⁺⁵⁷⁰ ₋₃₄₀	5.60 ^{+0.06} _{-0.08}	-2.54 ^{+0.17} _{-0.20}	-3.94 ^{+0.43} _{-0.65}	-3.93 ^{+0.34} _{-0.56}	-3.95 >	0.11	-0.348	-0.195	#7,ca	
201554.27+054824.91	sdB	13.60	14.41	32510 ⁺²⁶⁰ ₋₂₃₀	5.88 ^{+0.05} _{-0.06}	-1.79 ^{+0.06} _{-0.07}	-4.15 >	-4.41 ^{+0.39} _{-0.98}	-4.71 >	0.04	-0.543	-0.206	#7,ca,r	
202027.26+070414.45A	sdO	13.85	14.02	44210 ⁺²⁶³⁰ ₋₂₂₈₀	5.98 ^{+0.25} _{-0.23}	-2.13 ^{+0.34} _{-0.79}	-4.37 >	-4.34 >	-3.57 >	0.00	0.357	0.237	#7,rv	
202027.26+070414.45B	F3V			6070	3.08			[Fe/H] = -1.11			(0.558)	(0.241)	M	
202059.85-225001.42A	sdB	11.92	11.82	34350 ⁺³³⁰ ₋₁₄₀	5.44 ^{+0.19} _{-0.02}	-1.80 ^{+0.11} _{-0.06}	-4.56 ^{+0.61} _{-0.08}	-4.61 ^{+0.57} _{-0.08}	-4.25 ^{+0.52} _{-0.08}	0.02	0.702	0.266	#7,rv	
202059.85-225001.42B	G0V			5920	4.04			[Fe/H] = 0.13			(0.495)	(0.196)	M	
202216.83+015225.18A	sdB	13.56	13.19	36700 ⁺¹¹⁶⁰ ₋₁₆₆₀	5.79 ^{+0.25} _{-0.12}	-1.52 ^{+0.22} _{-0.21}	-5.93 >	-3.77 >	-3.52 >	0.07	0.847	0.240	#7	
202216.83+015225.18B	F6V			6310	4.27			[Fe/H] = -0.25			(0.629)	(0.175)	M	
202332.75+013618.82	sdB	12.78	12.42	29450 ⁺⁴⁶⁰ ₋₁₇₀	5.60 ^{+0.06} _{-0.04}	-2.44 ^{+0.07} _{-0.20}	-4.16 ^{+0.29} _{-0.46}	-4.12 ^{+0.29} _{-0.30}	-4.35 >	0.05	-0.947	-0.095	#7,ca,rv	
203850.22-265747.16A	sdO	11.81	11.90	58450 ⁺⁴⁶⁰⁰ ₋₇₉₂₀	5.04 ^{+0.39} _{-0.17}	-1.13 ^{+0.27} _{-0.29}	-3.22 >	-2.94 >	-2.62 >	0.13	1.502	0.454	#7,rv	
203850.22-265747.16B	G3.5III			5270	3.02			[Fe/H] = -0.29			(1.289)	(0.432)	M	
203913.41+201309.38	sdB	12.69	12.64	30600 ⁺²⁷⁰ ₋₂₇₀	5.52 ^{+0.08} _{-0.06}	-3.18 >	-4.34 >	-4.18 >	-4.40 >	0.01	-0.945	-0.111	#7,rv	
204302.45+103427.08	He-sdO	11.62	12.06	45700 ⁺¹⁰⁷⁰ ₋₆₃₀	6.08 ^{+0.13} _{-0.25}	0.78 ^{+0.12} _{-0.25}	-2.37 ^{+0.85} _{-0.22}	-2.45 ^{+0.56} _{-1.02}	-1.92 >	0.03	-0.572	-0.181	#7,C&N,t	ALS 11497,LSIV+10 9
204709.60+121015.38	sdB	13.73	14.31	35510 ⁺³⁰⁰ ₋₄₈₀	5.88 ^{+0.07} _{-0.06}	-1.52 ^{+0.05} _{-0.09}	-4.74 >	-3.93 >	-4.37 >	0.07	-0.658	-0.086	#7,ca,r	
205321.05-400626.94	BHB	11.55	12.25	23050 ⁺³⁵⁰ ₋₂₆₀	4.78 ^{+0.05} _{-0.09}	-1.36 ^{+0.09} _{-0.09}	-4.50 ^{+0.62} _{-0.57}	-3.95 ^{+0.33} _{-0.52}	-3.70 >	0.06	-0.241	-0.158	#7,ca,rv	[SRA98] 6-1829
205652.32+033548.88	sdO	13.36	14.27	40350 ⁺⁶¹⁰ ₋₁₁₃₀	5.55 ^{+0.07} _{-0.09}	-2.98 ^{+0.24} _{-0.50}	-4.90 >	-4.50 >	-4.42 >	0.03	-0.830	-0.074	#7,ca	

Table 2. Atmospheric parameters of hot subdwarf stars in the *GALEX* survey. Continued.

GALEXJ	Type	N_{UV} (mag)	V (mag)	T_{eff} (K)	$\log g$ (cm s^{-2})	Abundances, [X/H] _• or [Fe/H]				$E(B - V)$ (mag)	$V - J$ (mag)	$J - H$ (mag)	Comments	Other name
						He	C	N	O					
205956.79–423203.58	BHB	11.54	11.43	20730 ⁺¹⁵⁰ ₋₃₅₀	4.52 ^{+0.09} _{-0.04}	-0.40 ^{+0.01} _{-0.13}	-2.78 ^{+0.20} _{-0.33}	-2.90 ^{+0.39} _{-0.45}	-2.55 >	0.02	-0.499	-0.145	#7,ca	CD-43 14300
210031.71+145213.83A	sdB	13.51	13.09	34170 ⁺²⁴⁷⁰ ₋₉₂₀	5.79 ^{+0.20} _{-0.24}	-1.41 ^{+0.20} _{-0.27}	-3.61 >	-3.20 >	-3.76 >	0.03	0.611	0.210	#7,r	
210031.71+145213.83B	F5.5IV-V			6550	4.06			[Fe/H] = 0.31			(0.622)	(0.173)	M	
211041.43+142559.45	He-sdO	13.16	14.03	44470 ⁺⁶⁵⁰ ₋₃₅₀	6.23 ^{+0.08} _{-0.18}	1.15 ^{+0.13} _{-0.10}	-1.49 ^{+0.19} _{-0.18}	-2.05 ^{+0.29} _{-0.76}	-2.16 ^{+0.52} _{-1.40}	0.03	-0.711	-0.164	#7,C&N	
211230.92–152410.37	He-sdO	11.46	12.56	78990 ⁺³⁷⁵⁰ ₋₆₀₄₀	5.84 ^{+0.38} _{-0.06}	-0.05 ^{+0.29} _{-0.06}	-2.46 ^{+0.83} _{-0.58}	-2.25 ^{+0.45} _{-0.22}	-2.98 >	0.23	0.349	0.220	#7,C&N	
212240.41+055808.08	sdB	13.87	14.07	23340 ⁺³¹⁰ ₋₃₁₀	5.13 ^{+0.05} _{-0.04}	-2.15 ^{+0.05} _{-0.14}	-3.84 ^{+0.28} _{-0.36}	-3.96 ^{+0.53} _{-0.63}	-3.53 >	0.06	-0.127	0.028	#7,ca	
212328.22+833351.21	sdB	13.84	13.95	27920 ⁺¹⁰⁷⁰ ₋₂₃₀	5.47 ^{+0.06} _{-0.10}	-2.76 ^{+0.18} _{-0.30}	-3.97 >	-4.19 ^{+0.35} _{-1.27}	-3.82 >	0.07	-0.511	0.002	s	HS 2126+8320
212424.35+150619.44A	sdB	12.83	13.06	36030 ⁺⁸⁶⁰ ₋₄₅₀	5.80 ^{+0.10} _{-0.12}	-1.18 ^{+0.07} _{-0.12}	-3.80 >	-3.63 >	-3.89 >	0.01	0.599	0.233	#7,r	
212424.35+150619.44B	F7V			6080	4.28			[Fe/H] = -0.48			(0.552)	(0.160)	M	
212544.48+202812.18	He-sdO	12.21	13.67	53470 ⁺¹¹²⁰ ₋₂₉₉₀	6.28 ^{+0.07} _{-0.52}	0.38 ^{+0.39} _{-0.11}	-2.60 ^{+0.35} _{-0.88}	-1.94 >	-2.02 >	0.08	-0.296	-0.161	#7,C&N	
213730.94+221908.04A	sdB	13.03	13.51	36030 ⁺⁷⁶⁰ ₋₇₆₀	5.84 ^{+0.14} _{-0.15}	-1.26 ^{+0.13} _{-0.13}	-3.79 >	-3.25 >	-3.36 >	0.01	0.557	0.255	#7,r	
213730.94+221908.04B	G1V			5640	4.50			[Fe/H] = -0.65			(0.511)	(0.244)	M	
214022.87–371414.05A	sdB	12.48	12.79	32660 ⁺²⁶¹⁰ ₋₁₈₀	5.80 ^{+0.28} _{-0.12}	-1.61 ^{+0.12} _{-0.28}	-3.61 >	-3.64 >	-3.77 >	0.01	0.677	0.212	#7,r,rv	
214022.87–371414.05B	F6V			6170	4.18			[Fe/H] = -0.55			(0.585)	(0.170)	M	
215154.37+144208.42	sdB	13.90	14.46	34290 ⁺³³⁰ ₋₆₃₀	5.46 ^{+0.21} _{-0.03}	-2.84 >	-5.07 >	-4.20 >	-4.41 >	0.11	-0.498	-0.171	#7,ca	HS 2149+1428
220102.29+083050.94	He-sdO	13.18	13.38	75050 ⁺¹⁸⁰⁰ ₋₇₅₉₀	5.99 ^{+0.07} _{-0.24}	0.21 ^{+1.07} _{-0.06}	-3.06 >	-2.37 ^{+0.46} _{-0.90}	-2.62 >	0.09	-0.027	0.100	#7	PG 2158+082
220551.86–314105.55	sdB	12.58	12.22	28650 ⁺⁹³⁰ ₋₈₀	5.68 ^{+0.01} _{-0.14}	-2.09 ^{+0.12} _{-0.03}	-4.62 ^{+0.64} _{-0.53}	-4.53 ^{+0.51} _{-0.38}	-4.55 ^{+0.55} _{-0.87}	0.02	-0.527	-0.036	#7	BPS CS 30337-0074
222554.48+172310.86	sdB	13.79	14.63	37890 ⁺⁴²⁰ ₋₁₃₀₀	5.67 ^{+0.13} _{-0.08}	-1.39 ^{+0.09} _{-0.11}	-4.65 >	-4.09 >	-3.63 >	0.07	0.277	0.319	#7	PG 2223+171
222758.59+200623.32A	sdB	11.07	10.60	30540 ⁺¹⁰⁰⁰ ₋₁₅₂₀	5.76 ^{+0.38} _{-0.19}	-1.26 ^{+0.21} _{-0.30}	-5.98 >	-3.14 >	-3.30 >	0.00	0.558	0.100	#7	TYC 1703-394-1
222758.59+200623.32B	F5V			6610	4.33			[Fe/H] = 0.08			(0.701)	(0.180)	M	
223531.53+143358.82	sdB	12.86	14.05	35020 ⁺³⁸⁰ ₋₈₂₀	5.26 ^{+0.15} _{-0.10}	-2.72 ^{+0.33} _{-0.40}	-4.68 >	-4.09 ^{+0.38} _{-0.86}	-4.09 >	0.02	-0.593	-0.109	#7	HS 2233+1418
223521.97–502119.64	He-sdO	11.90	12.61	52460 ⁺²⁷³⁰ ₋₅₀₀	6.18 ^{+0.05} _{-0.41}	0.46 ^{+0.23} _{-0.09}	-2.75 ^{+0.45} _{-0.19}	-2.45 >	-2.03 >	0.00	-0.985	-0.091	#7,C&N	
223737.00+224414.00	sdO	12.32	12.92	42860 ⁺⁸⁷⁰ ₋₁₅₉₀	5.51 ^{+0.08} _{-0.12}	-3.06 ^{+0.39} _{-0.50}	-4.90 >	-4.40 >	-4.32 >	0.00	-0.489	-0.181	#7,ca	Balloon 90900004
223913.48+181945.69	sdB	13.81	14.29	28970 ⁺³⁹⁰ ₋₂₉₀	5.44 ^{+0.08} _{-0.04}	-2.55 ^{+0.21} _{-0.19}	-4.05 >	-4.39 ^{+0.39} _{-0.61}	-4.36 >	0.04	-0.214	-0.169	#7,s	
224503.57+322150.70	sdB	13.41	13.85	29530 ⁺⁴⁷⁰ ₋₃₂₀	5.61 ^{+0.08} _{-0.09}	-3.10 ^{+0.29} _{-0.62}	-3.98 >	-3.86 >	-3.71 >	0.05	-0.609	-0.157	na,f,t	HS 2242+3206
225444.11–551505.64	sdB	11.09	12.08	31070 ⁺¹⁵⁰ ₋₁₉₀	5.80 ^{+0.04} _{-0.06}	-2.47 ^{+0.15} _{-0.13}	-4.65 >	-4.51 >	-4.54 >	0.02	-0.745	-0.151	#7,r,rv	
230314.37+392544.80	sdB	13.73	14.10	35620 ⁺³⁷⁰ ₋₆₉₀	5.64 ^{+0.27} _{-0.05}	-1.52 ^{+0.18} _{-0.08}	-4.88 >	-4.54 >	-4.33 >	0.02	-0.495	-0.178	na	
232350.79+143108.08	sdB	13.85	14.70	28220 ⁺⁴⁴⁰ ₋₂₆₀	5.38 ^{+0.15} _{-0.02}	-3.16 ^{+0.32} _{-0.77}	-4.48 >	-4.46 ^{+0.41} _{-2.69}	-3.98 >	0.03	-0.544	-0.187	#7,s,rv	PG 2321+142
232917.93+325348.37A	sdB	13.13	12.79	34870 ⁺³⁶³⁰ ₋₁₂₆₀	5.90 ^{+0.60} _{-0.36}	-1.52 ^{+0.46} _{-0.61}	-2.64 >	-2.53 >	-3.08 >	0.01	0.850	0.146	na,he,r	
232917.93+325348.37B	F4V			6300	4.04			[Fe/H] = -0.29			(0.685)	(0.180)	M	
233158.95+281522.68A	sdB	13.82	14.11	38460 ⁺²⁹⁵⁰ ₋₁₅₈₀	5.65 ^{+0.25} _{-0.33}	-2.15 >	-3.92 >	-3.43 >	-3.42 >	0.00	0.265	0.179	d	
233158.95+281522.68B	F8V			5920	4.23			[Fe/H] = -0.31			(0.232)	(0.119)	M	
234422.01–342700.39	sdB	11.39	10.95	28390 ⁺⁴¹⁰ ₋₁₂₀	5.39 ^{+0.05} _{-0.03}	-3.07 ^{+0.21} _{-0.26}	-4.83 >	-4.83 ^{+0.37} _{-0.97}	-4.23 >	0.02	-0.631	-0.103	#7,s	CD–35 15910
234947.65+384441.57	sdB	11.31	11.71	23770 ⁺³³⁰ ₋₃₅₀	5.38 ^{+0.05} _{-0.06}	-3.44 ^{+0.25} _{-0.30}	-3.97 >	-4.08 >	-3.99 >	0.09	-0.330	-0.116	RV ^f	FBS 2347+385

^f Kawka et al. (2010)

J1831+0851 is possibly an imminent WD progenitor. It lies well below the HeMS at a gravity higher than typical for He-sdO stars. Also, its He abundance is not comparable to its spectral class.

J1845-4138. We found $T_{\text{eff}} = 35\,930^{+840}_{-4770}$ K, $\log g = 5.23^{+0.27}_{-0.23}$ and $[\text{He}/\text{H}]_{\bullet} = 2.1^{+1.1}_{-0.4}$ in good agreement with our previous analysis. This star shows an extremely high He abundance compared to its location in the $T_{\text{eff}}-\log g$ diagram. It is in the region of post-EHB evolution, where He-weak sdB stars are, but shows a He abundance typical for He-sdO stars. Its surface gravity is also inconsistent with its location. A high-dispersion spectrum is needed for further analysis. No infrared excess was found.

J1902-5130 (CD-51 11879, LSE 263) was analysed by Husfeld et al. (1989). They found $T_{\text{eff}} = 70\,000 \pm 2500$ K, $\log g = 4.9 \pm 0.25$, $[\text{H}/\text{He}]_{\bullet} < -1.0$, $[\text{C}/\text{He}]_{\bullet} = -4.0 \pm 0.5$ and $[\text{N}/\text{He}]_{\bullet} = -2.4 \pm 0.3$. Our analysis confirms the temperature and the He dominated, N-rich atmosphere, but provided a 0.5 dex higher surface gravity. Missing or incomplete atomic data and broadening parameters in the earlier analysis can be accounted for such discrepancy. Due to upper limit determinations and asymmetric errors, a direct comparison with our results is not possible.

J2043+1034 (LSIV+10 9) was analysed by Dreizler (1993) who found $T_{\text{eff}} = 44\,500 \pm 1000$ K, $\log g = 5.55 \pm 0.15$ and mass fractions ($\beta_x = m_x/m_{\text{total}}$): $\log \beta_{\text{He}} = -0.001$, $\log \beta_{\text{C}} = -1.85 \pm 0.1$, $\log \beta_{\text{N}} = -2.45 \pm 0.15$ and $\log \beta_{\text{O}} = -2.40 \pm 0.15$. Our analysis resulted in $T_{\text{eff}} = 45\,700^{+1000}_{-630}$ K, $\log g = 6.08^{+0.13}_{-0.24}$, and mass fractions: $\log \beta_{\text{He}} = -0.023$, $\log \beta_{\text{C}} = -2.69$, $\log \beta_{\text{N}} = -2.71$ and $\log \beta_{\text{O}} < -2.12$. We derived a notably higher gravity and lower abundances, in particular for He and C. This can be due to the incomplete composition of our models and that we fitted the entire spectrum not just selected lines. The relatively lower quality of our fits for He-sdO stars also suggests the importance of heavier metals in their modelling.

J2245+3221 (HS 2242+3206) was fitted by Edelmann et al. (2003). Their analysis of H_{β} - H_{10} , $\text{He II } 4686$, $\text{He I } 4471$ and $\text{He I } 4026$ lines provided $T_{\text{eff}} = 29\,300 \pm 1000$ K, $\log g = 5.65 \pm 0.15$ and $[\text{He}/\text{H}]_{\bullet} = -2.8 \pm 0.2$. Our data covered the optical range from 3700 to 7150 Å and we derived $T_{\text{eff}} = 29\,530^{+470}_{-320}$ K, $\log g = 5.61^{+0.08}_{-0.09}$ and $[\text{He}/\text{H}]_{\bullet} = -3.1^{+0.29}_{-0.62}$ in good agreement.

9 CONCLUSIONS

We presented a homogeneously modelled sample of 124 sdB and 42 sdO stars and determined non-LTE atmospheric parameters by considering H, He and CNO opacities. With binary decomposition we were able to derive accurate atmospheric parameters for the members in ~ 30 composite spectra binaries. Our study shows that sdB stars concentrate in two groups in the $T_{\text{eff}} - \log g$ and $T_{\text{eff}} - \text{He}$ diagrams, suggesting two typical H envelopes with different masses and compositions. He-sdO and He-weak sdO stars also clearly separate in the $T_{\text{eff}} - \text{He}$ diagram and He-weak sdO stars can be related to sdB stars based on their He abundance and binary frequency.

The developed method for spectral decomposition can reliably determine atmospheric parameters in composite spectra binaries. The method can also be used to remove the spectral contamination caused by merging stars from subdwarf spectra. Such cleaning process and homogeneous modelling on large samples are necessary to provide accurate atmospheric parameters for evolutionary, pulsational and diffusion theories. We investigated the impact of binarity on subdwarf atmospheric parameters and showed that unresolved composite spectra binaries can cause significant shifts. Such systematic shifts can easily overwhelm non-LTE or abundance ef-

Table 3. Other targets that are not part of the GALEX UV selection.

GALEXJ	Type	N_{UV} (mag)	V (mag)	T_{eff} (K)	$\log g$ (cm s^{-2})	Abundances, $[\text{X}/\text{H}]_{\bullet}$ or $[\text{Fe}/\text{H}]$				E(B-V) (mag)	V-J (mag)	J-H (mag)	Comments	Other name
						He	C	N	O					
071646.93+231930.16A	B	13.32	11.63	11140 ± 180	4.39 ^{+0.06} _{-0.22}	-1.06 >	-2.31 >	-1.76 >	-1.75 >	0.00	0.105 (0.012)	0.016 (0.001)	na	
071646.93+231930.16B	A1V			9310	3.67			[Fe/H] = 0.11					M	
085158.89-171238.86^a	He-sdO	12.16	11.40	39060 ⁺⁵⁸⁰ ₋₁₅₀	5.79 ^{+0.10} _{-0.04}	=3.00	-1.08 >	-0.15 ^{+0.14} _{-0.23}	-0.42 >	0.04	-1.013	-0.139	#7,t	TYC 6017-419-1
160011.80-643330.35^a	He-sdB		11.86	34640 ⁺⁵⁹⁰ ₋₅₈₀	6.02 ^{+0.08} _{-0.11}	-0.30 ^{+0.05} _{-0.04}	-2.83 ^{+0.31} _{-0.15}	-2.92 ^{+0.18} _{-0.45}	-3.78 >	0.03	-0.708	-0.167	#7	TYC 9044-1653-1
215341.26-700431.55^a	sdB	12.36	11.53	23720 ⁺²⁶⁰ ₋₂₃₀	5.65 ^{+0.03} _{-0.02}	-3.22 ^{+0.13} _{-1.15}	-4.49 >	-4.11 >	-3.89 >	0.00	-0.622	-0.112	#7	TYC 9327-1311-1
234903.27+411925.62A	B?	12.92	9.93	≈11730	≈5.79	-1.00 >	-1.00 >	-1.00 >	-1.00 >	0.10	0.602 (0.284)	0.039 (0.090)	d	BD+40 5153
234903.27+411925.62B	A4V			7940	3.44		[Fe/H] = 0.13						M	

^a Target is taken from Jiménez-Esteban, Caballero, & Solano (2011).

fects and we consider binary decomposition necessary for precision spectroscopy of hot subdwarfs with a notable IR excess.

We did not find a significant sdB–A binary frequency with our current selection criteria. However, a joint analysis of ultraviolet and optical measurements would be necessary to spectroscopically distinguish the components in such binaries. Recently, Girven et al. (2012) investigated the companions of hot subdwarfs and found that F, G and K type MS companions outnumber A and M-type stars.

Our abundance analysis of He-sdO stars confirms the C&N classification scheme of Stroerer et al. (2007): cooler stars show N enriched atmospheres, hotter He-sdO stars are C-rich while we detected both C and N mostly in between these two groups. The C&N-class objects suggest a C/N ratio of ~ 3 in He-sdO stars. The spectra of cooler sdB stars show a N enrichment while hotter sdB stars do not show notable CNO abundances in general.

The observed luminosity distribution suggests a shorter EHB (~ 100 Myr) and longer post-EHB (~ 50 Myr) evolution than previous studies found. The luminosity distribution of sdB stars is sharply peaked at $\log(L/L_{\odot}) \approx 1.5$ assuming an average sdB mass of $0.48 M_{\odot}$. We found two peaks in the luminosity distribution of sdO (post-EHB) and He-sdO stars.

We reviewed our results in terms of the current evolutionary theories. Our study does not give satisfying answers for the relative contributions of the various channels, but shows evidences that He-sdO and He-rich sdB stars are related. The He-weak sdO sequence and the group of He-rich sdB stars are mixtures of different populations.

A binarity analysis of the hottest He-sdO stars ($T_{\text{eff}} > 60\,000$ K) could provide interesting results about the relation of these stars to cooler He-sdO or He-weak sdO stars. In this region the sequences of evolved He-sdO stars and He-weak sdO stars overlap. A much larger sample could help clarifying the surface gravity diversity observed at these stars, which currently suggests a connection to the He-weak sequence.

Further follow-up is necessary at higher resolution and high signal-to-noise to improve CNO determination in the optical and better understand subdwarf stars, and the contributions of various formation and evolution channels. With higher quality data it may become possible to derive reliable O abundances that could offer further clues in understanding these stars.

In addition to subdwarfs, our survey recovered six WDs that will be discussed in a forthcoming paper.

10 THE SD1000 COLLABORATION

A similar study on a larger sample could provide a more complete picture of hot subdwarfs. For this reason we would like to extend this pilot study and initiate a cooperative work under the name "SD1000 Collaboration", dedicated to process ~ 1000 hot subdwarf spectra in a homogeneous way. Such an analysis can provide important observational constraints for theoretical studies and help the advance of subdwarf research. The Subdwarf Database currently holds 2399 stars and about 1900 of these have V , J and H photometric measurements. Figure 21 shows the colour indices of these stars. About ~ 800 stars in the data base are brighter than $V = 15$ and ~ 1150 are brighter than $V = 16$ providing a rich source of bright targets for the project.

However, recording new, high-quality optical spectra ($R > 3000$ or $\delta\lambda < 3 \text{ \AA}$, $\text{SNR} > 100$) for ~ 1000 stars would require about 60–80 nights on 4-m class telescopes what is not practically feasi-

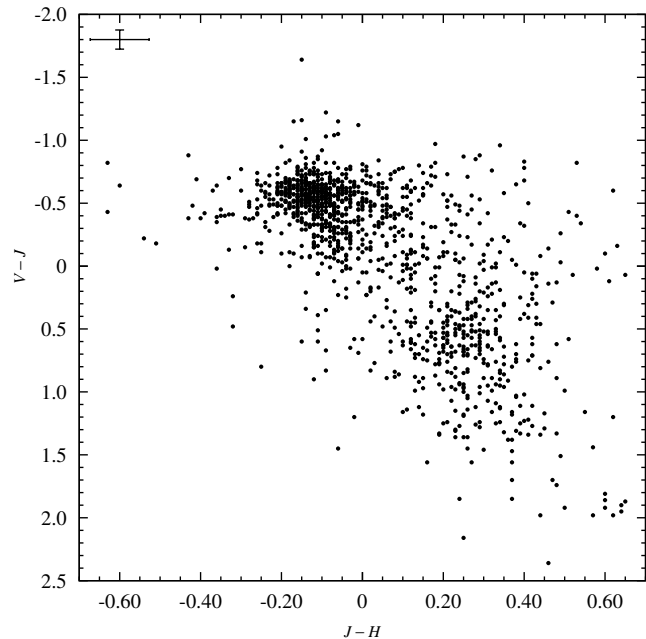


Figure 21. $V-J$ - $J-H$ diagram for ~ 1900 hot subdwarf stars in The Subdwarf Database (Østensen 2006), data were collected from various sources. Typical error bars for colour indices were calculated from average photometric errors.

ble. Acquiring data from public archives could be a way, although, data reduction of various observing runs can introduce a significant overhead and not all data are available in such archives. Moreover, it is important to maximise the number of spectra to number of instruments ratio in the sample to decrease instrumental biases. The most efficient strategy would use contributed data for the bulk and obtain new observations for a small subset to fill the sample. Therefore, the success of this project depends strongly on contributed data and we look for collaborators. We estimate that enough observations (~ 2000 stars) have been taken over the last 30 years to compile the target sample.

Model atmosphere analysis would require ~ 2000 hours with single star models and 8 processors. Using binary decomposition and estimating about 20 per cent composite spectra in the sample would extend the analysis to ~ 2400 hours, which is still manageable.

ACKNOWLEDGMENTS

We acknowledge support from the Grant Agency of the Czech Republic (GA ČR P209/10/0967) and from the Grant Agency of the Academy of Sciences of the Czech Republic (IAA 300030908, IAA 301630901). We would like to thank our referee Roy Østensen for his valuable comments and suggestions. This research has made use of the SIMBAD database and the VizieR catalogue access tool, operated at CDS, Strasbourg, France.

REFERENCES

- Ahmad A., Jeffery C. S., A&A, 2003, 402, 335
- Aznar Cuadrado R., Jeffery C. S., 2001, A&A, 368, 994
- Aznar Cuadrado R., Jeffery C. S., 2002, A&A, 385, 131

- Baran A. S., Gilker J. T., Reed M. D., Østensen R. H., Telting J. H., Smolders K., Hicks L., Oreiro R., 2011, *MNRAS*, 413, 2838
- Bessell M. S., 2005, *ARAA*, 43, 293
- Brown T. M., Ferguson H. C., Davidsen A. F., Dorman B., 1997, *ApJ*, 482, 685
- Cardelli J. A., Clayton G. C., Mathis J. S., 1989, *ApJ*, 345, 245
- Cenarro A. J. et al., 2007, *MNRAS*, 374, 664
- Charpinet S., Fontaine G., Brassard P., 2001, *PASP*, 113, 775
- Charpinet S., Fontaine G., Brassard P., 2009, *A&A*, 493, 595
- Charpinet S., Fontaine G., Brassard P., Chayer P., Green E. M., Randall S. K., 2007, *CoAst*, 150, 241
- Charpinet S. et al., 2010, *A&A*, 516, L6
- Charpinet S. et al., 2011, *A&A*, 530, A3
- D'Cruz N. L., Dorman B., Rood R. T., O'Connell R. W., 1996, *ApJ*, 466, 359
- Divine N., 1965, *ApJ*, 142, 824
- Dorman B., Rood R. T., O'Connell R. W., 1993, *ApJ*, 419, 596
- Dreizler S., 1993, *A&A*, 273, 212
- Driebe T., Schoenberner D., Bloeker T., Herwig F., 1998, *A&A*, 339, 123
- Edelmann H., Heber U., Hagen H.-J., Lemke M., Dreizler S., Napiwotzki R., Engels D., 2003, *A&A*, 400, 939
- Eisenstein D. J. et al., 2006, *APJS*, 167, 40
- Ferguson D. H., Green R. F., Liebert J., 1984, *ApJ*, 287, 320
- Frew D. J., Madsen G. J., O'Toole S. J., Parker Q. A., 2010, *PASA*, 27, 203
- Geier S., Classen L., Heber U., 2011b, *ApJ*, 733, L13
- Geier S., Heber U., Edelmann H., Kupfer T., Napiwotzki R., Podsiadlowski P., 2009, *Journal of Physics Conf. Series*, 172, 012008
- Geier S., Heber U., Edelmann H., Morales-Rueda L., Kilkeny D., O'Donoghue D., Marsh T. R., Copperwheat C., 2012, *ASPC*, 452, 57
- Geier S. et al., 2011a, *A&A*, 530, A28
- Girven, J. et al., 2012, *MNRAS*, 425, 1013
- Gray David F., *The observation and analysis of stellar spectra*, 1992, Cambridge University Press, 2nd edition
- Green E. M., Fontaine G., Hyde E. A., For B.-Q., Chayer P., 2008, *ASPC*, 392, 75
- Green E. M. et al., 2003, *ApJ*, 583, L31
- Green R. F., Schmidt M., Liebert J., 1986, *ApJS*, 61, 305
- Grevesse N., Sauval A. J., 1998, *Space Science Rev.*, 85, 161
- Groth H. G., Kudritzki R. P., Heber U., 1985, *A&A*, 152, 107
- Haas S., Dreizler S., Heber U., Jeffery S., Werner K., 1996, *A&A*, 311, 669
- Han Z., Podsiadlowski Ph., Maxted P. F. L., Marsh T. R., Ivanova N., 2003a, *MNRAS*, 336, 449
- Han Z., Podsiadlowski P., Maxted P. F. L., Marsh T. R., 2003b, *MNRAS*, 341, 669
- Heber U., 2009, *Annu. Rev. A&A*, 47, 211
- Hirsch H. A., 2009, PhD thesis, University of Erlangen-Nürnberg
- Hirsch H. A., Heber U., O'Toole S. J., 2008, *ASP Conf. Ser.*, 392, 131
- Hu, H., 2011, *ASP Conf. Ser. Vol. 462*, 54
- Hu H., Dupret M.-A., Aerts C., Nelemans G., Kawaler S. D., Miglio A., Montalbán J., Scuflaire R., 2008, *A&A*, 490, 243
- Hubeny I., Lanz T., 1995, *ApJ*, 439, 875
- Husfeld D., Butler K., Heber U., Drilling J. S., 1989, *A&A*, 222, 150
- Jeffery C. S., Saio H., 2006, *MNRAS*, 372, L48
- Jiménez-Esteban F. M., Caballero J. A., Solano E., 2011, *A&A*, 525, A29
- Kawka A., Vennes S., Németh P., Kraus M., Kubát J., 2010, *MNRAS*, 408, 992
- Kilkenny D., Heber U., Drilling J. S., 1988, *SAAO Circular*, 12, 1
- Kilkenny D., O'Donoghue D., Stobie R. S., 1988, *MNRAS*, 248, 664
- Kilkenny D., Fontaine G., Green E. M., Schuh S., 2010, *IBVS*, 5927, 1
- Kurucz R., 1993, *ATLAS9 Stellar Atmosphere Programs and 2 km/s grid*. Kurucz CD-ROM No. 13. Cambridge, Mass., 13
- Lanz T., Hubeny I., 1995, *ApJ*, 439, 905
- Lanz T., Hubeny I., 2003, *ApJS*, 146, 417
- Lanz T., Hubeny I., 2007, *ApJS*, 169, 83
- Lanz T., Brown T. M., Sweigart A. V., Hubeny I., Landsman, W. B., 2004, *APJ*, 602, 342
- Lasker B. M., et al., 2008, *AJ*, 136, 735
- Lisker T., Heber U., Napiwotzki R., Christlieb N., Han Z., Homeier D., Reimers D., 2005, *A&A*, 430, 223
- Lisker T., Heber U., Napiwotzki R., Christlieb N., Han Z., Homeier D., Reimers D., 2005, *ASP Conf. Ser.*, 334, 303
- Maxted P. f. L., Heber U., Marsh T. R., North R. C., 2001, *MNRAS*, 326, 1391
- Mengel J. G., Norris J., Gross P. G., 1976, *ApJ*, 204, 488
- Mickaelian A. M., 2008, *AJ*, 136m 946
- Miller Bertolami M. M., Althaus L. G., Unglaub K., Weiss A., 2008, *A&A*, 491, 253
- Morrissey P., et al., 2007, *ApJS*, 173, 682
- Napiwotzki R., 1999, *A&A*, 350, 101
- Napiwotzki R., 2008, *ASP Conf. Ser.*, 391, 257
- Napiwotzki R., Karl C. A., Lisker T., 2004, *Ap&SS*, 291, 321
- O'Connell R. W., 1999, *Annu. Rev. A&A*, 37, 603
- O'Donoghue D., Lynas-Gray A. E., Kilkeny D., Stobie R. S., Koen C., 1997, *MNRAS*, 285, 657
- Østensen R. H., 2004, *Ap&SS*, 291, 263
- Østensen R. H., 2006, *Baltic Astronomy*, 15, 85
- Østensen R. H., 2009, *CoAst*, 159, 75
- Østensen R. H., Van Winckel H., 2012b, *ASPC*, 452, 163
- Østensen R. H. et al., 2010, *A&A*, 513, A6
- Østensen R. H. et al., 2011, *MNRAS*, 414, 2860
- Østensen R. H. et al., 2012a, *ApJ*, 753, L17
- O'Toole S. J., 2008, *ASP Conf. Ser.*, 392, 67
- O'Toole S. J., Heber U., 2006a, *A&A*, 452, 579
- O'Toole S. J., Heber U., 2006b, *MmSAI*, 77, 164
- Paczyński B., 1971, *Acta Astron.*, 21, 1
- Pickles A. J., 1998, *PASP*, 110, 863
- Reed M. D., Stiening R., 2004, *Ap&SS*, 291, 329
- Sánchez-Blázquez P. et al., 2006, *MNRAS*, 371, 703
- Schlegel D. J., Finkbeiner D. P., Davis M., 1998, *ApJ*, 500, 525
- Silva D. R., Cornell M. E., 1992, *ApJSS*, 81, 865
- Skrutskie M. F., et al., 2006, *AJ*, 131, 1163
- Soker N., 1998, *AJ*, 116, 1308
- Stark M. A., Wade R. A., 2003, *AJ*, 126, 1455
- Ströer A., Heber U., Lisker T., Napiwotzki R., Dreizler S., 2005, *ASP Conf. Ser.*, 334, 309
- Stroerer A., Heber U., Lisker T., Napiwotzki R., Dreizler S., Christlieb N., Reimers D., 2007, *A&A*, 462, 269
- Thejll P., Ulla A., MacDonald J., 1995, *A&A*, 303, 773
- Unglaub K., 2008, *A&A*, 486, 923
- Unglaub K., Bues I., 2001, *A&A*, 374, 570
- Vazdekis A., Cenarro A. J., Gorgas J., Cardiel N., Peletier R. F., 2003, *MNRAS*, 340, 1317
- Vennes S., Kawka A., Németh P., 2011a, *MNRAS*, 410, 2095

- Vennes S. et al., 2011b, *ApJL*, 737, L16
Vennes S., Kawka A., O'Toole S. J., Németh P., Burton D., 2012, *ApJ*, 759, L25
Vučković M., Østensen R. H., Acke B., Reed M. D., Oreiro R., Bloemen S., Baran A. S., 2012, *ASPC*, 452, 257
Webbink R. F., 1984, *ApJ*, 277, 355
Werner K., Dreizler S., 1999, *Journal of Computational and Applied Mathematics*, 109, 65
Werner K., Dreizler S., Haas S., Heber U., 1998, *ESA Special Publication*, 413, 301
Wisotzki L., Reimers D., Wamsteker W., 1991, *A&A*, 247, L17
Zhang X., Jeffery S. C., 2012, *MNRAS*, 419, 452
Zhang X., Chen X., Han Z., 2010, *Astrophys Space Sci.*, 329, 11

APPENDIX A: CNO ABUNDANCE CORRELATIONS

This paper has been typeset from a $\text{\TeX}/\text{\LaTeX}$ file prepared by the author.

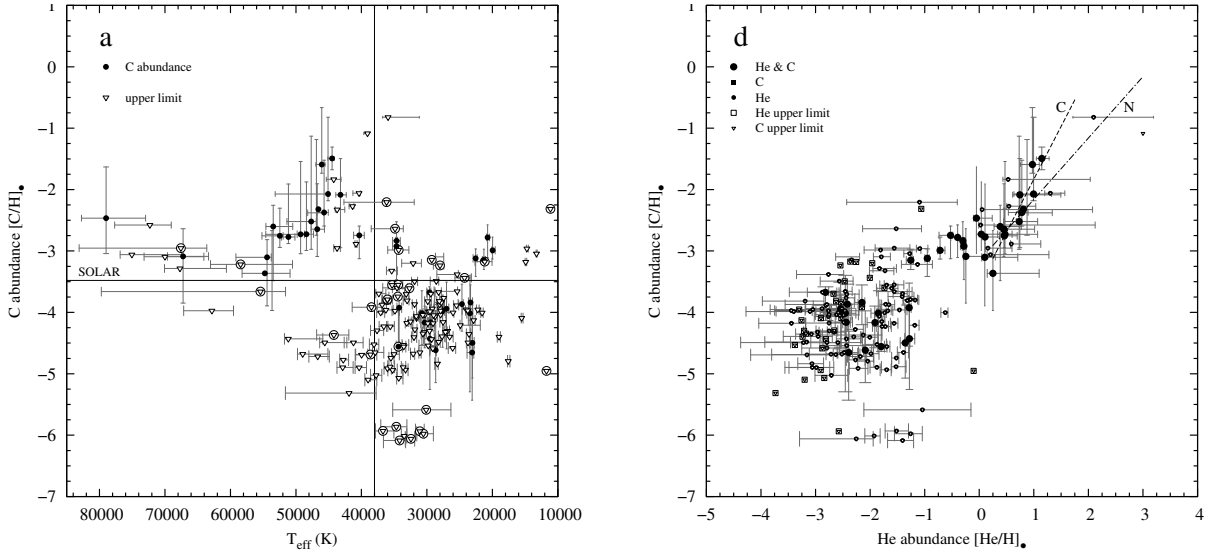


Figure A1. Panels *a* and *d* of Figure 9 complemented with error bars and upper limit measurements. *Left*: Observed C abundances with respect to effective temperature. The vertical line at 38 000 K separates sdB and sdO stars and the horizontal line shows the solar C abundance. *Right*: C and He abundance correlations.

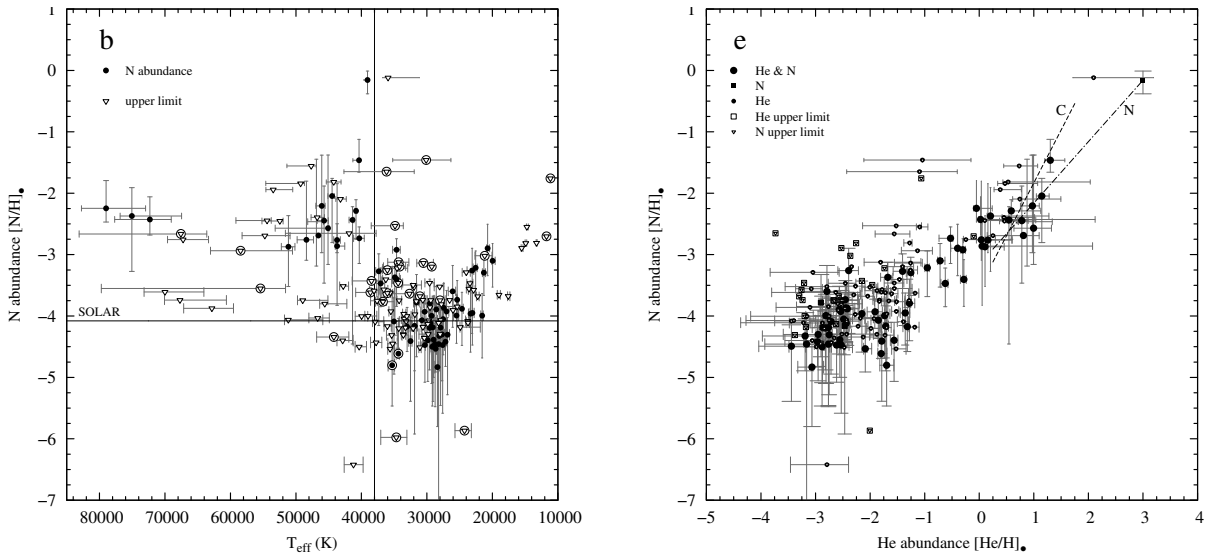


Figure A2. Panels *b* and *e* of Figure 9 complemented with error bars and upper limit measurements. *Left*: Observed N abundances with respect to effective temperature. The vertical line at 38 000 K separates sdB and sdO stars and the horizontal line shows the solar N abundance. *Right*: N and He abundance correlations.

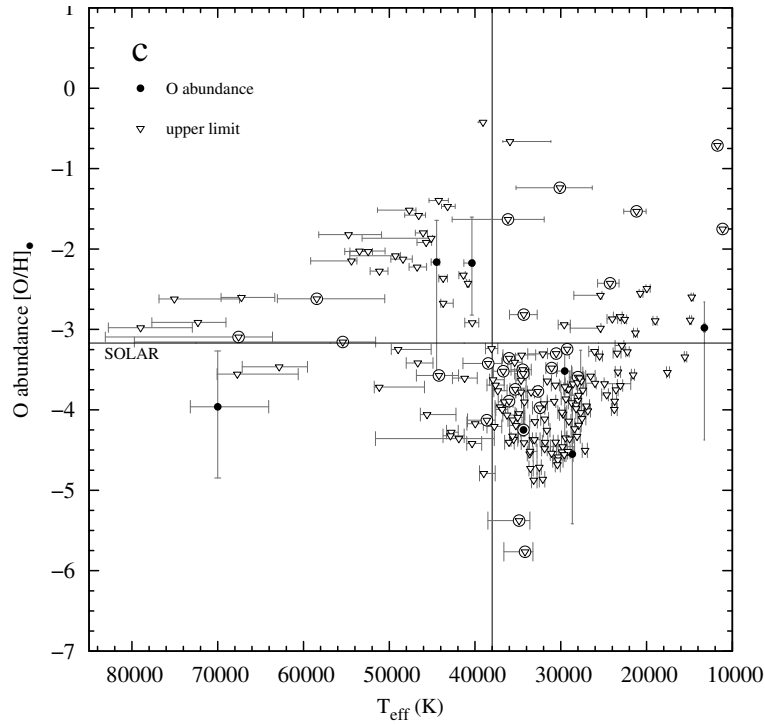


Figure A3. Panel *c* of Figure 9 complemented with error bars and upper limit measurements shows our observed O abundances with respect to effective temperature. The vertical line at 38 000 K separates sdB and sdO stars and the horizontal line shows the solar O abundance.

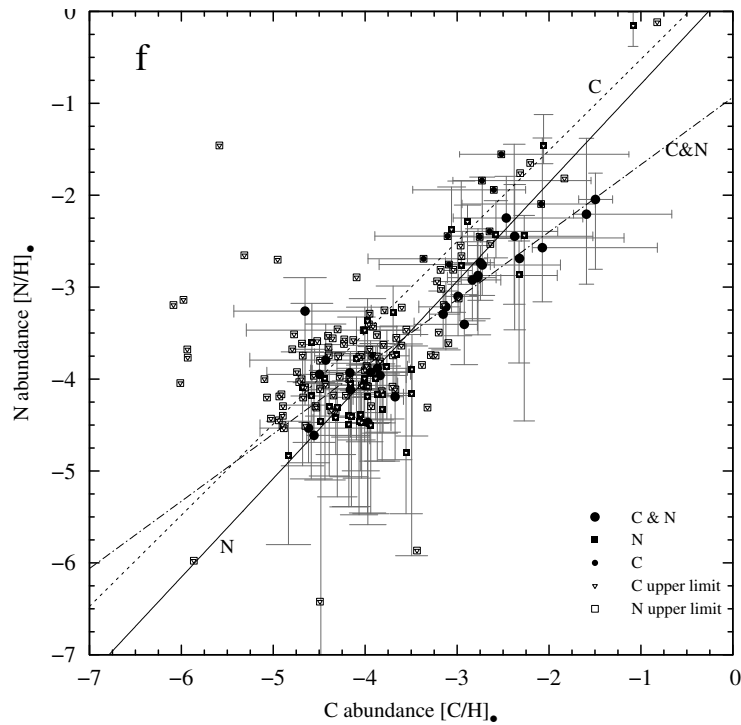


Figure A4. Panel *f* of Figure 9 complemented with error bars and upper limit measurements showing the C and N abundance correlations found in the GALEX sample.